A COARSE MESH TRANSPORT METHOD WITH NOVEL SOURCE TREATMENT

A Dissertation
Presented to
The Academic Faculty

By

Caleb I. Price

In Partial Fulfillment
Of the Requirements for the Degree
Doctor of Philosophy in Nuclear and Radiological Engineering

Georgia Institute of Technology

May 2015

A COARSE MESH TRANSPORT METHOD WITH NOVEL SOURCE TREATMENT

Approved by:

Dr. Farzad Rahnema, Advisor
George W. Woodruff School of
Mechanical Engineering
Georgia Institute of Technology

Dr. Eric Elder, Co-Advisor
Department of Radiation Oncology
Emory University School of Medicine

Dr. Chris Wang
George W. Woodruff School of
Mechanical Engineering
Georgia Institute of Technology

Dr. Timothy Fox
Imaging Informatics
Varian Medical Systems

Dr. Thomas Morley
School of Mathematics
Georgia Institute of Technology

Date Approved: April 2, 2015

For my dear friend Nasser.

ACKNOWLEDGEMENTS

I would like to extend my deepest gratitude to those without whom this work would not have been possible. First I must thank my dear friend, mentor, and advisor Dr. Nasser Maleki. Nasser's unflagging support made me a better physicist and a better person. Although he did not live to see the final product, he never doubted this day would come.

Thank you also to my advisor Dr. Farzard Rhanema and my co-advisor Dr. Eric Elder. It has been a privilege to work with both of you. Thank you to Dr. Chris Wang, Dr. Tim Fox, and Dr. Thomas Morley for serving on my committee. Also I would like to thank Dr. Sang Hyun Cho, for making his phase space files available to me even though they were no longer available for general use.

Of particular note is the assistance and guidance of Robert Hayward. Without his hard work on the COMET code and his willingness to share the subtleties of his work, I would have been lost. Thanks for sharing your brilliant mind.

I would be remiss to leave out all of the physicians and staff of the Cancer Care Institute of Carolina and the Anderson Cancer Institute. Thank you for allowing me to continue my research and putting up with me during particularly stressful days.

Lastly I wish to express my appreciation to my family and friends. My mother, father, and sisters have always been a great source of encouragement in all my endeavors. To my friend, Dr. Zachary Friis, thanks for constantly pushing me to finish so that we can finally live out our dream of shrimp farming in Florida.

Most of all I wish to thank my lovely wife Nico. You have tolerated the ups and downs of living with a graduate student for too long and for that I am truly grateful.

TABLE OF CONTENTS

LIST OF TABLES

LIST OF FIGURES

SUMMARY

A novel source model was developed to represent the radiation emanating from the head of linear particle accelerator for use in radiotherapy dosimetric calculations. Of note is the use of a hemispherical harmonic expansion with the functional expansion tally method to model the photonic fluence. The source is implemented in the COMET-PE radiation transport code for dose calculations with varying field sizes in different phantoms. The results are benchmarked against Monte Carlo reference solutions and compared with calculations performed with two popular commercially available treatment planning algorithms.

The results show that the proposed source model when implemented within the COMET-PE radiation transport code is capable of dosimetric calculations that in many cases more closely match the Monte Carlo reference solutions than the commercially available options. The approach is therefore validated with the tradeoff of increased computation time.

CHAPTER 1

INTRODUCTION

1.1 Area of Research

This PhD dissertation is in the area of dose calculation algorithms and treatment planning for radiotherapy. The focus of the dissertation is the development of a realistic source model for a dose calculation algorithm developed at the Georgia Institute of Technology and to compare sample calculations to commercially available products.

1.2 Motivation

Cancer is an increasing cause of death in modern life. In 2007 cancer caused about 13% of all human deaths [1]. One common form of treatment is the use of ionizing radiation to kill cancerous tumor cells within the body. This form of therapy is typically delivered with a linear particle accelerator. In order to safely and effectively treat patients with radiation, modern radiation oncology centers utilize three dimensional dose calculation algorithms to predict the dose distribution within a patient. Three dimensional dose calculation algorithms allow a radiation treatment plan to be developed and optimized to deliver a therapeutic dose to the tumor while minimizing the radiation dose to normal tissue. In recent years complicated techniques have been developed for delivering radiation to achieve these goals. Techniques such as Intensity Modulated Radiation Therapy (IMRT), Image Guided Radiation Therapy (IGRT), and Volume Modulated Arc Therapy (VMAT) improve the clinician's ability to deliver radiation accurately.

Intensity modulated radiation therapy (IMRT) has been called one of the most significant technical advances in radiation therapy since the advent of the medical linear accelerator [2]. IMRT seeks to shape dose distributions by modulating the intensity of each radiation field being delivered. A variety of options are available for modulating the beam including: precision machined blocks and varying the leaf position in the multileaf collimator during irradiation. Figure 1 shows an intensity pattern from a sample plan developed using a sliding window IMRT technique being delivered using a multileaf collimator. It has been demonstrated that IMRT treatments can be delivered within 0.05% of the planned dose at isocenter [3].

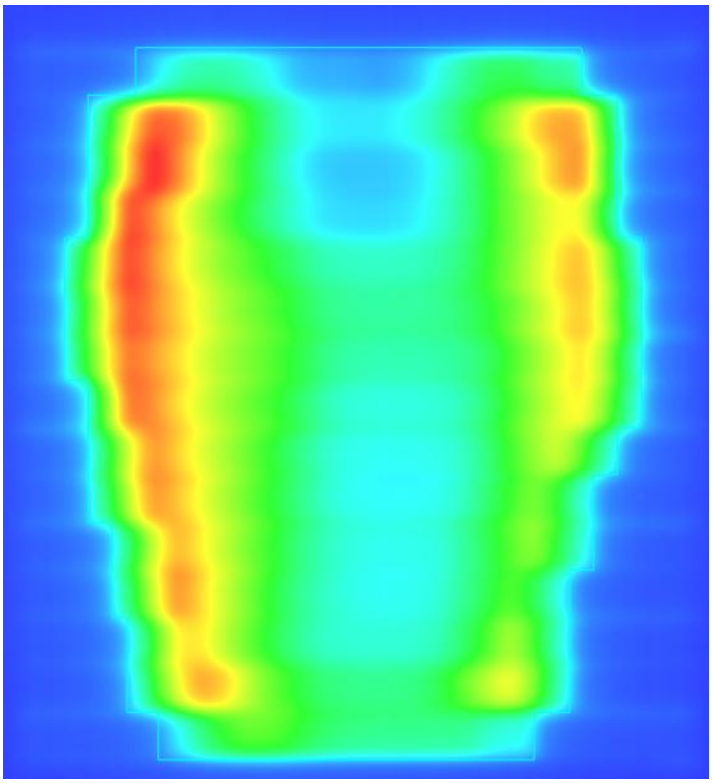

Figure 1: Intensity pattern from an IMRT plan

Another advancement that has impacted the accuracy of linear accelerator based radiotherapy is image guided radiation therapy (IGRT). IGRT refers to the host of recent technologies that integrate image based techniques in tumor identification and delineation with patient positioning and delivery devices and/or radiation delivery guiding tools [4]. IGRT addresses uncertainties associated with tumor target definition, patient immobilization, and patient breathing motion, which complicate delivery of high radiation doses to a planned location. The International Commission on Radiological Protection recommends that an accuracy of 2% and precision of 1% should be the target requirement for IMRT delivery using IGRT [5].

Volume modulated arc therapy has become a popular treatment option because it can be used to create treatment plans that are comparable to IMRT plans but can be delivered in a fraction of the time. This is achieved by not only moving the leaves in the multileaf collimator during radiation delivery, but also rotating the gantry around the patient. Figure 2 is an image of a sample VMAT patient plan. The patient received 50 Gy in 10 fractions using non-coplanar arcs to minimize low dose to normal lung. Treatment times in stereotactic lung cases have been shown to be shorter in VMAT treatments to an average of 6.6 minutes compared with 23.7 min with non-coplanar IMRT [6]. The reduced treatment time is an obvious benefit for the patients, many of whom have difficulty breathing and are in pain. It is also of benefit in delivering radiation accurately. It is intuitive that the longer a patient remains on the treatment table the more likely they are to move out of the treatment position.

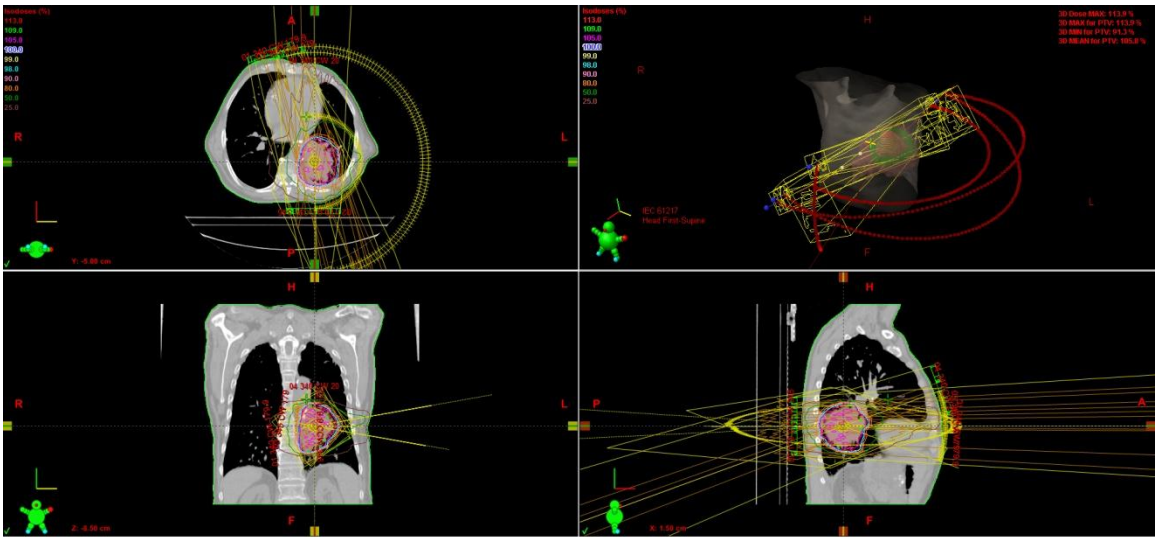

Figure 2: VMAT plan for inoperable left lung tumor

It is logical to conclude that if we can deliver the therapeutic dose accurately, there is a need for treatment planning algorithms that are sufficiently capable of producing accurate calculations to match. The effectiveness of radiation therapy depends on the ability to maximize the Tumor Control Probability (TCP) while minimizing Normal Tissue Complication Probability (NTCP). TCP and NTCP are very sensitive to absorbed dose. A 5% change in dose corresponds to a 20% change in NTCP as seen in Figure 3 [7]. Dose calculation algorithms that are currently in popular use have been shown commonly to have calculation discrepancies of up to 7% [8]. The gold standard for dose calculation has long been Monte Carlo methods. The drawback of Monte Carlo methods is the extended calculation times. In this research project reference calculations were generated that took as long as two weeks to calculate on a Dell Precision 490 Workstation with a quad-core Intel Xeon 5300 series processor. In a busy clinical environment, calculation times should be on the order of a few minutes.

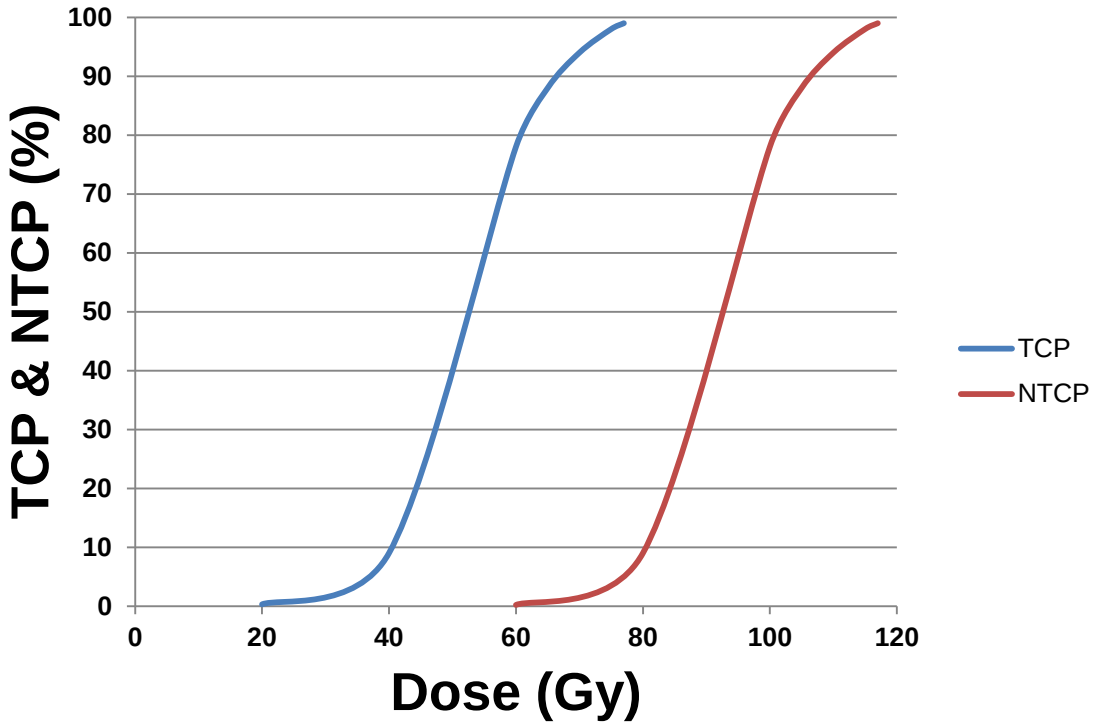

Figure 3: TCP & NTCP vs. Dose

The heterogeneous coarse-mesh transport code COMET has been demonstrated by Satterfield to produce highly accurate dose models within the context of radiation therapy problems [9]. The code was further developed by Hayward et al. into the COMET-PE method to include a new angular basis and analytical source treatment making it more suitable for use in radiotherapy calculations [10]. It is a promising new approach to producing highly accurate dose distributions with calculation times that are much smaller than Monte Carlo methods. The COMET-PE code was used for this work and will now simply be referred to as COMET. The COMET code however needs a clinically realistic source model. The source model should be representative of a clinical radiation beam emanating from the head of linear particle accelerator. With the realistic source in place, the COMET code can then be

benchmarked against a Monte Carlo calculation. It is also reasonable to compare the performance of COMET to existing commercially available software packages.

1.3 Objectives

The primary objective of this work is to construct a practical source model that can be incorporated into COMET. It is important that the source mimic the physical characteristics of a typical beam from a clinical linear particle accelerator. The source treatment should also not be so complex as to add an unacceptably long source integration time into the final dose calculation.

A secondary goal of this research is to validate the COMET code against a known benchmark. In this case Monte Carlo dose calculation has been chosen for the reference. The Monte Carlo technique is the most accurate method for radiotherapy treatment planning dose calculation to date [11]. It is therefore an excellent choice for generating reference dose distributions.

Finally, it is desirable to compare COMET calculations with commercially available calculation algorithms. Two algorithms have been chosen for comparison: the Analytical Anisotropic Algorithm (AAA) and Acuros XB (AXB). Comparisons will be made using phantoms of known composition and density and an actual computed tomography (CT) scan from a patient.

CHAPTER 2

REVIEW OF DOSE CALCULATION

The attributes of a good dose calculation algorithm include a basis in first principles, accuracy as measured against a measured standard, speed, and expandability [7]. There have been a variety of methods used in treatment planning software since the mid 1950's. Early attempts at automated dose calculations were made with analog computers developed to reduce calculation times in calculating 2-D dose distributions. In 1967 the International Atomic Energy Agency (IAEA), used a manual procedure to digitize single beam isodose charts and a computer was used to combine multiple single beams to generate an atlas of isodose distributions for arc and rotational therapy [12]. The advent of computed tomography in the 1970s made patient specific anatomical information available. It became possible, for the first time, to actually derive electron density information *in vivo*, which could then be incorporated into the dose calculation process [13].

Modern treatment planning derives precise three-dimensional information from various imaging modalities including CT, magnetic resonance (MRI), positron emission tomography (PET), single photon emission computed tomography (SPECT), digital angiography, and ultrasound. Imaging data can be processed for improved tumor definition and identification of normal tissues. The patient can be virtually simulated on a computer workstation and a variety of treatment options can be contemplated during the treatment planning process. The culmination of all this technology is a sophisticated treatment simulation and planning process. The manner in which dose is calculated has also made impressive advances.

This review will briefly describe the various methods that have been and are being used. For reference, dose calculation algorithms can be categorized as either measurement based or model based [7].

2.1 A Note on Phantoms and Patients

In this work the terms phantom and patient are often used to describe a medium being irradiated by a photon beam. The ultimate goal of any dose calculation algorithm is the accurate calculation of dose within the patient. To that end, extensive measurements are clinically taken to characterize the radiation beam being produced by linear particle accelerators used in radiotherapy. Radiation beam measurements are often taken in various phantoms with some form of radiation detector.

Phantoms can be as simple as an acrylic tank filled with water or as complicated as an anthropomorphic phantom with simulated respiratory motion. Water phantoms as a substitute for human tissue have been used from as early as 1918 [14]. In 1924, Quimby confirmed that water was a reasonable substitute for measurements in tissue by comparing measurements in a cadaver with measurements made in water, beeswax, paraffin, wood, and rice [15].

It is routine practice to confirm dose calculations using measurements taken in phantoms. In this research the terms patient and phantom can often be used interchangeably.

2.2 Measurement Based Algorithms

Measurement based algorithms are sometimes called correction based because they rely on measured data in water along with empirically derived correction factors. These correction factors account for patient contour, internal anatomy, and beam

modifiers [7]. While measurement based algorithms dominated radiation treatment planning for many years, they are not the norm in the modern radiation oncology department.

2.2.1 Correction Based Algorithms

Correction based algorithms begin with a calculation made under somewhat idealized conditions. Corrections based on measurements are applied to adjust the calculation to more realistic conditions. Stated another way correction methods aim to convert phantom dose to patient dose. Figure 4 demonstrates this concept in an illustrative way.

In general, a calculation is started with the assumption of a cube shaped patient at a reference source to surface distance (SSD) with uniform tissue density. The calculation is then adjusted for the patient contours, thickness, and composition. Any beam modifiers, such as wedges, blocks, or compensators, also are taken into account in the calculation. A host of correction factors and alternative ways of calculating such factors have been proposed, formulated, and clinically tested. These algorithms quickly become quite complex. A few of the more common correction methods are described here.

2.2.2 Patient Contour Corrections

Contour corrections address the fact that a patient is not a cube of water like the phantoms that are frequently used to acquire characteristic beam data in radiotherapy. Often the approach taken is to account for the so called “missing” tissue, that is, the tissue that must be removed from a cuboidal phantom to match the shape of the patient.

The effective source-to-surface distance method uses percentage depth dose (PDD) and the assumption that PDD is independent of SSD to scale the depth of maximum dose with an inverse square factor. Figure 4 illustrates the concept [16]. The dose desired is at point A expressed as a percentage of the maximum dose at point Q shown below the $S' - S'$ line. The dose can be calculated using the following equation:

$$D_A = D'_{max} \cdot P' \tag{1}$$

where D_A is the dose at point A, P' is the percentage depth dose at A relative to D'_{max}. D'_{max} is the maximum dose relative to the $S' - S'$ line, taken as if the SSD at central axis is at the level of the line $S' - S'$. The desired dose is calculated relative to D_{max}, which is the true maximum dose along the central axis. This is calculated by scaling according the inverse square law incorporated into equation 2.

$$D_A = D_{max} \cdot P' \cdot \left(\frac{SSD + d_m}{SSD + h + d_m}\right)^2 \tag{2}$$

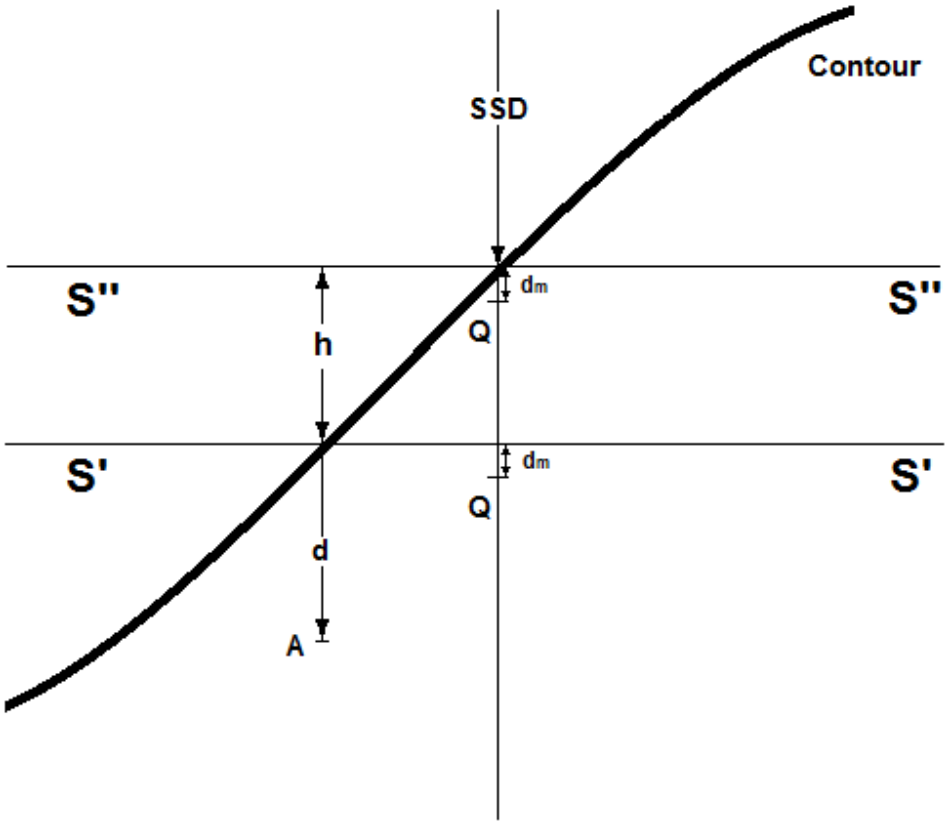

Figure 4: Effective SSD method

Another method commonly used to account for contour irregularities is the tissue-air ratio (TAR) method. The TAR method is useful for clinical applications because it does not depend on the surface distance from the source but only depends on the field size at the depth. This is especially useful in calculations for rotational therapy, where the linear accelerator rotates around the patient while delivering the therapeutic radiation dose. The TAR method is formulated in equation 3:

$$TAR(d, r_d) = \frac{D_d}{D_{fs}} \tag{3}$$

where d is the depth within the phantom at which the measurement is taken, r_d is the size of the radiation field at the depth d, D_d is the dose at a given depth d within the phantom, and D_{fs} is the dose in free space at the same point. To use the TAR method to account for the contour of the patient a correction factor is calculated according to equation 4:

$$CF = \frac{TAR(d, r_d)}{TAR(d + h, r_d)} \tag{4}$$

where CF is the correction factor, $TAR(d, r_d)$ is the TAR at depth d where the tissue deficiency exists, $TAR(d + h, r_d)$ is the TAR at a depth of $d + h$, and h is the distance between the surface used to define the SSD and the surface at the location of the tissue deficiency. In this context the word deficiency is used to denote that the distance from the source to the surface is not at the reference SSD. In some locations the surface of the patient is higher than the reference SSD and in other locations it is lower.

Many other methods have been used to correct for contour irregularities that are not mentioned here.

2.2.3 Heterogeneity Corrections

Another meaningful correction included in many algorithms accounts for the fact that patients are not homogeneous in composition. The TAR method has also been used to calculate correction factors to account for the inhomogeneous nature of patients. In equation 5 a ratio of TAR's is taken to account for a tissue inhomogeneity:

$$CF = \frac{T(d', r_d)}{T(d, r_d)} \tag{5}$$

where d' is the equivalent water depth $d' = d_1 + \rho_e d_2 + d_3$ and d is the depth of dose calculation, d_1 is the distance from the surface to the heterogeneity, d_2 is the distance from the top of the heterogeneity to the bottom, ρ_e is the electron density of the heterogeneity relative to water, d_3 is the distance from the bottom of the heterogeneity to the point of calculation, and r_d is field size projected at the point of calculation. Using a ratio of TAR to correct for inhomogeneity in the patient does not account for the position of the inhomogeneity. A method that does consider the position of the inhomogeneity in the tissue is the Batho power law method.

The Batho power law was originally proposed by H.F. Batho in 1964. The method was originally formulated as an empirical correction for a calculation point located in tissue-equivalent material below a lung-type heterogeneity in Co-60 irradiation [17]. Using the same notation in Equation 5, Equation 6 shows the correction factor calculated with tissue air ratios:

$$CF = \left[\frac{TAR(d_2 + d_3, r_d)}{TAR(d_3, r_d)}\right]^{\rho_e^{-1}} \tag{6}$$

The power law was later reformulated by Sontag and Cunningham for the more general situation where the dose calculation point can be below the heterogeneity or within it [18]. This formulation is shown in equation 7:

$$CF = \frac{TAR(d_3, r_d)^{\rho_3 - \rho_2}}{TAR(d_2 + d_3, r_d)^{1-\rho_2}} \quad (7)$$

where ρ_3 is the density of the material in which the calculation point lies, d_3 is its depth within this material, ρ_2 is the density of the overlying material, and $(d_2 + d_3)$ is the depth below the upper surface of it. The generalized Batho power law is based on the following assumptions [18]:

1. Only the material above the calculation point is considered in the calculation of the correction factor. It is assumed that the material below the calculation point is the same at the material of the calculation point.
2. The effect of heterogeneity on the dose is assumed to be independent of the thickness of the tissue-equivalent material located above the heterogeneity.
3. Charged particle equilibrium exists at the point of interest.
4. The lateral dimensions of all the regions are assumed to be at least as large as the beam dimensions.

Not all of these assumptions hold in non-idealized calculations. For example in high-energy radiation beams, charged particle equilibrium does not always exist. Also not all regions irradiated in the patient have lateral dimensions as large as the beam dimensions.

Other methods that have been used to correct for inhomogeneities include: the Equivalent Tissue-air Ratio Method and the Isodose Shift Method.

2.2.4 Problems with Correction-Based Algorithms

There are several problems with correction-based algorithms that have contributed to their decline in popularity. First they usually assume that a state of electronic equilibrium exists. Electronic equilibrium is a state where as many electrons

are set in motion in a given volume by photon interactions as stop in the same volume. This state exists when the ionization lost in a given volume is compensated by the ionization gained. It is well established that particularly in areas of the body with low electron densities, electronic equilibrium does not exist.

Correction-based algorithms are also inaccurate near heterogeneities. Calculation inaccuracies as high as 20% have been reported in the literature [19]. As has been already established, modern radiotherapy strives to attain a much higher level of accuracy in both calculation and delivery.

Another drawback of calculation based measurements is that they require copious measurements. Huge lookup tables must be compiled for off-axis factors, beam output, wedge factors, etc.

2.3 Model Based Algorithms

Unlike measurement based algorithms, model based algorithms simulate radiation transport using physical laws to calculate the dose distribution within a medium. These models use measured data to derive the parameters of the model. They rely on fewer measurements than correction type dose calculation algorithms. Measured data is used to modify parameters in order to better match the physical characteristics of the radiation beam. Energy deposition at and around photon interaction sites is then computed with the model based algorithm. The two most common model based algorithms are convolution superposition and Monte Carlo.

2.3.1 Convolution-Superposition

Measurement based algorithms make the assumption that all charged-particle energy is deposited locally. This is an acceptable assumption for cobalt-60 radiation but

is not valid for megavoltage beams, which are the norm in modern radiation therapy. Figure 5 demonstrates the radiation transport problem [17]. The interaction of a primary photon occurs at some point within the patient. The scatter from that interaction contributes to the dose deposited at point P(x,y,z).

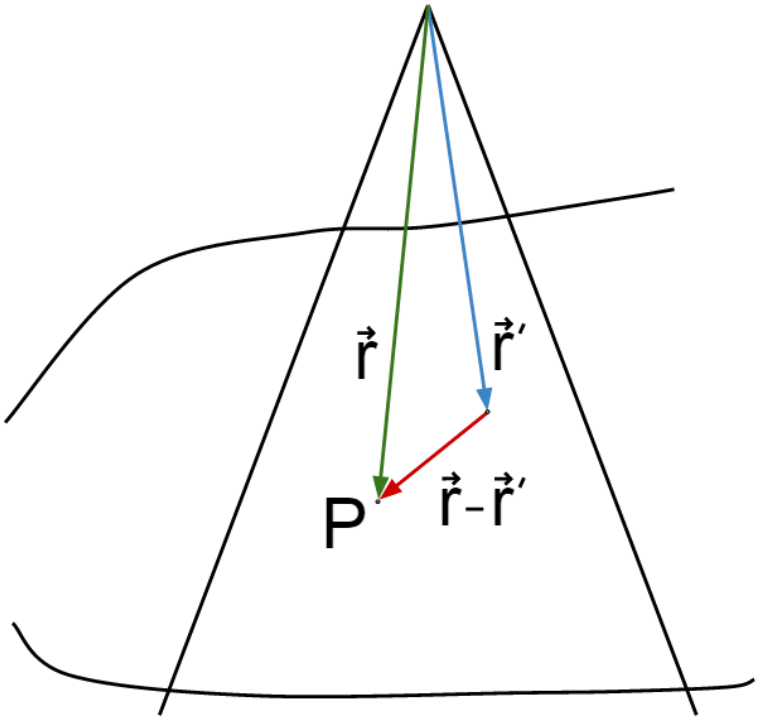

Figure 5: Photon interaction and scatter

Primary photons are those photons that are incident upon the surface of the phantom or patient in this context. Some primary photons have traveled directly from the radiation source to the position of their first interaction, while others are the product of an interaction in the head of the linear accelerator. Most of these interactions are Compton scattering events, which also produce secondary electrons that can reach the phantom and contribute to dose deposition. Primary photons contribute to the dose at a

point in the phantom when they have their first interaction within the medium and produce recoil electrons.

Scattered dose within the patient is the result of photon interactions from photons that have already interacted at least once within the phantom. The proportion of scattered and primary contributions to the dose at a particular point depends on many factors including position of the point, the energy of the beam, the field size of the beam, and the patient thickness.

Scatter can be evaluated as originating from various depths, slabs, pencil beams, or from singular points within the phantom. The dose is often therefore decomposed into primary and scatter components within the patient.

The convolution-superposition algorithm was proposed by Mackie et. al in 1985 [20]. It is currently the most popular dose calculation algorithm used in the clinic [7]. The convolution superposition algorithm accounts for nonlocal energy deposition by rigorously tracking the lateral spread of scattered photons and charged particles liberated by primary photons. The pattern of energy from a primary interaction is called a scatter kernel. Various methods have been employed to calculate scatter kernels including derivation from measurement and pre-calculation using Monte Carlo methods (see section 2.3.6) [21, 22].

The convolution equation for calculating dose is given below:

$$D(\vec{r}) = \int \frac{\mu}{\rho} \Psi_p(\vec{r}\,') A(\vec{r} - \vec{r}\,') d^3\vec{r}\,' = \int T_p(\vec{r}\,') A(\vec{r} - \vec{r}\,') d^3\vec{r}\,' \quad (8)$$

where μ/ρ is the mass attenuation coefficient, $\Psi_p(\vec{r}\,')$ is the primary photon energy fluence, and $A(\vec{r} - \vec{r}\,')$ is the convolution kernel. The kernel is obtained by Monte Carlo

simulation of photons of a given energy interacting at a point and spatially mapping the absorption of the resulting release of energy or it is derived from measurements. $T_p(\vec{r}')$ is the TERMA, which is an acronym for **T**otal **E**nergy **R**eleased per unit **MA**ss. The terma is the product of the mass attenuation coefficient and the primary photon energy fluence. It represents the total amount of radiation energy available at r' available for deposition. The product of terma and the dose kernel integrated over volume is the dose $D(\vec{r})$.

The convolution-superposition algorithm is obtained by correcting equation 8 for radiologic path length.

$$D(\vec{r}) = \int T_p(\rho_{\vec{r}'} \cdot \vec{r}')A(\rho_{\vec{r}-\vec{r}'} \cdot (\vec{r} - \vec{r}'))d^3\vec{r}' \tag{9}$$

Radiologic path length is the distance corrected for electron density relative to water. Radiologic path length from the source to the primary photon interaction site is given by $\rho_{\vec{r}'} \cdot \vec{r}'$ and the radiologic path length from the site of primary photon interaction to the site of dose deposition is given by $\rho_{\vec{r}-\vec{r}'} \cdot (\vec{r} - \vec{r}')$.

2.3.2 Pencil Beam Convolution (PBC)

The pencil beam convolution (PBC) calculates dose according to the method described above with the addition of polyenergetic pencil beam kernels [23]. These polyenergetic kernels are pre-calculated for a megavoltage narrow ("pencil") beam in water and can be described analytically by the sum of the two exponentials shown below.

$$\frac{p}{\rho}(r,z) = \frac{A_z e^{-a_z r}}{r} + \frac{B_z e^{-b_z r}}{r} \quad (10)$$

where r is the cylindrical radius from the pencil beam axis and A_z, a_z, B_z, b_z and are fitting parameters dependent on the depth z and $\frac{p}{\rho}$ is used to represent the energy fraction deposited per unit mass. The first term in equation 10 represents primary dose and the second term results from scatter dose. Other kernels are calculated for specific clinical conditions such as calculating dose in the penumbra region, accounting for charged particle contamination, and photon contamination. Each pencil beam contributes dose to a point based on the point's position relative to the pencil beam, making the convolution calculation relatively fast.

The pencil beam convolution does have several disadvantages. It is not scaled laterally to account for changes in radiation transport due to inhomogeneities. It also breaks down at interfaces and for structures smaller than the pencil beam.

In 2006, Rassiah-Szegedi compared finite-size pencil beam/equivalent path-length (FSPB/EPL) and Monte Carlo computations for use in stereotactic body radiation therapy [24]. They reported that FSPB/EPL consistently overestimated minimum doses to the clinical target volume and planning target volumes by an average of 18.1±7.15% and 21.9±10.4% respectively. Mean target dose differences were 15.5±7.4% and 19.2±7.6%. The differences were shown to be dependent on lesion size and location. Smaller lesions completely surrounded by lung tissue were found have the greatest differences while larger lesions in contact with the chest wall or mediastinum were found to have the least.

2.3.3 Analytical Anisotropic Algorithm (AAA)

The analytical anisotropic algorithm (AAA) is a convolution-superposition algorithm implemented in the Eclipse treatment planning system produced by Varian Medical Systems, Palo Alto, CA. It was proposed by Waldemar Ulmer and Wolfgang Kaissl in 1995 [25]. AAA uses a multiple-source model to represent the clinical beam. Patient scatter is represented with density scalable poly-energetic kernels.

In the clinical implementation of AAA, the broad clinical beam is divided into finite-sized beamlets. Each beamlet is modeled using several monoenergetic scatter kernels to produce poly-energetic scatter kernels. The cross-sectional dimensions of the beamlet correspond to the resolution of the calculation being performed. Calculation grid size can be varied from 2-5 mm.

The beamlet energy fluence is separated into contributions from primary photons, extrafocal photons, and contaminant electrons [26]. Dose contribution from a beamlet β is modeled through the convolution of its fluence Φ and energy deposition density function $I(z,\rho)$ with scatter kernel (x,y,z,ρ) , that defines the lateral dose scattering in the medium.

$$D_\beta(x,y,z) = \Phi_\beta \times I_\beta(z,\rho) \times \iint_\beta K_\beta(x'-x, y'-y, z, \rho)dx'dy' \tag{11}$$

Depth-dependent functions used in the beamlet convolutions are computed along the central fanline of the beamlet. Scatter dose is defined on the spherical shell perpendicular to the central fanline of the beamlet. Total dose $D(x,y,z)$deposited at a point (x,y,z) by a therapeutic beam is calculated as a superposition of beamlet contributions, $D_\beta(x,y,z)$.

The main feature of AAA that distinguishes it from PBC is the treatment of scatter kernels. AAA scatter kernels are density dependent and are evaluated in multiple lateral directions from the beamlet.

The photon scatter is also convolved with a density-scaled kernel along the beamlet direction. This method more accurately reproduces the dose at the border of heterogeneities.

In 2006 Gagne and Zavgorodni, evaluated the differences between AAA and PBC calculations versus Monte Carlo in water-lung interface phantoms. The results showed that AAA is significantly more accurate than PBC in this situation. Confidence limits on AAA calculations were calculated at 4% while PBC confidence limits ranged from 3.5% to 11.2% [27].

2.3.4 Collapsed Cone Convolution

The collapsed cone convolution is a convolution dose calculation algorithm that discretizes point kernels with respect to angle. All energy released into coaxial cones of equal solid angle, from volume elements on the cone axis, is rectilinearly transported, attenuated, and deposited in elements on along each angle [28]. In other words, the cones are collapsed onto their central axes. The number of angles used to discretize the kernel is typically on the order of 100 to 128. Density scaling is applied along each discretized angle.

The kernel is also parameterized in a manner similar to pencil beam convolution. Equation 12 demonstrates this parameterization.

$$h(r) = \frac{A_\theta e^{-a_\theta} + B_\theta e^{-b_\theta}}{r^2} \tag{12}$$

where A_θ, a_θ, B_θ, and b_θ are fitting parameters depending on the scaterring angle θ. As with pencil beam convolution the first term describes the primary dose fraction and the second term describes the scatter dose fraction [29].

Combining the angular discretization along with the above parameterizations yields the following equation describing the collapsed cone convolution point kernels. Each discrete angular sector (cone) is represented by Ω_i.

$$\iint_{\Omega_i} \frac{h_{\rho_0}}{\rho}(r,\Omega) r^2 d^2\Omega = A_{\Omega_i} e^{-a_{\Omega_i} r} + B_{\Omega_i} e^{-b_{\Omega_i} r} \tag{13}$$

The collapsed cone convolution method does suffer from displacement errors. The displacement increases with distance from the point of primary interaction but is somewhat compensated by the fact that the first scatter fraction decreases with increasing distance. This makes the approach acceptable because the total energy deposited is conserved. Displacement errors are less important in the calculation because most energy is deposited close to where it is released.

In 2007 Hasenbalg, et al. compared dose calculations from collapsed cone convolution and analytical anisotropic algorithms to Monte Carlo calculations in clinical cases [30]. Hasenbalg reported that in the five clinical cases studied the CCC performed better than AAA when compared to Monte Carlo. Dose differences between the algorithms for the median value of the planning target volume (PTV) were reported to be typically 0.4% in the lung and -1.3% in the breast.

2.3.5 Acuros XB

An alternative to correction based methods and convolution methods for dose calculation, is to numerically solve the Linear Boltzmann Transport Equation (LBTE). The LBTE is the governing equation that describes the macroscopic behavior of ionizing particles as they travel through and interact with matter. Within a given volumetric domain of matter subject to a radiation source, the solution to the LBTE would give an exact description of the dose [31]. Analytical solutions to the LBTE can only be obtained for a few simplified problems. Therefore practical implementation of the LBTE involves solving the equation in a non-analytical manner.

Numerical methods explicitly solve the LBTE by discretizing the equation in space, angle, and energy. The system is then solved in an iterative manner. Methods which deterministically solve the LBTE are referred to as grid-based Boltzmann solvers (GBBS) [32]. Because of the discretization, methods for solving the LBTE inherently introduce errors. Larger steps in the discretization produce a faster calculation but less accuracy.

Acuros XB is a grid-based Boltzmann solver developed by Varian Medical Systems, Inc. for use in external beam radiotherapy calculations. It is based on a solver called Attila, which was co-authored by the founders of Transpire, Inc. while at Los Alamos National Laboratory [33].

Attila employs linear discontinuous finite-element spatial differencing on a computational mesh consisting of tetrahedral elements. The primary photon fluence is analytically transported through ray tracing, and the discrete ordinates method is used for angular differencing of the scattered fluence.

Acuros XB transports fluence through a patient by the following four steps:

1. Transport of source model fluence into the patient.
2. Calculation of scattered photon fluence into the patient.
3. Calculation of scattered electron fluence in the patient.
4. Dose calculation.

Unlike convolution superposition algorithms, Acuros XB requires a material map of the imaged patient. Algorithms like AAA account for heterogeneities using density-based corrections, but Acuros XB explicitly models the physical interactions of radiation with matter. Thus not only is material density required but also the chemical composition of each material. In the Varian implementation of Acuros XB, a material library of 5 biological materials and 16 non-biological materials are provided to generate the material map. Table 1 lists materials stored in the material library. The material map is generated by matching the mass density in each voxel of the image grid with the associated material type.

Table 1: Material specification Acuros

Material	Density		
	Minimum (g/cm^3)	Default (g/cm^3)	Maximum (g/cm^3)
Biological Materials			
Lung (ICRP 1975)	0.011	0.26	0.6242
Adipose Tissue (ICRP 1975)	0.5539	0.92	1.001
Muscle, Skeletal (ICRP 1975)	0.9693	1.05	1.0931
Cartilage (ICRP 1975)	1.0556	1.1	1.6
Bone (ICRP 1975)	1.1	1.85	3
Non-Biological			
Air	0.0012	0.0012	0.0204
Aluminum	2.275	2.7	3.56
Titanium Alloy	3.56	4.42	6.21
Stainless Steel	6.21	8	8
Water	0.0012	1	3
Wood	0.3	0.7	1
Cork	0.1	0.19	0.4
Polystyrene	0.59	1.05	1.075
Epoxy		1.04	
PMMA		1.19	
Radel		1.3	
PEEK		1.31	
PVC		1.38	
Acetal		1.42	
PVDF		1.77	
PTFE		2.2	

Acuros XB solves a system of coupled time-independent three-dimensional linear Boltzmann transport equations. For a problem spatial domain with volume, V, and surface, δV, the equations take the following form.

$$\widehat{\Omega} \cdot \vec{\nabla}\Phi^{\gamma} + \sigma_t^{\gamma}\Phi^{\gamma} = q^{\gamma\gamma} + q^{\gamma} \tag{14a}$$

$$\widehat{\Omega} \cdot \vec{\nabla}\Phi^{e} + \sigma_t^{e}\Phi^{e} - \frac{\partial}{\partial E}(S_R\Phi^{e}) = q^{ee} + q^{\gamma e} + q^{e} \tag{14b}$$

Equation 14a solves for photon transport and 14b solves for electron transport. Photons are denoted by γ and electrons are denoted by e. Note that the dependent variables have been suppressed in equations 14a and 14b for brevity. The variables used in each equation are defined in Table 2.

Table 2: LBTE variable definitions

$\Phi^{\gamma}(\vec{r}, E, \widehat{\Omega})$ is the photon angular fluence
$\Phi^{e}(\vec{r}, E, \widehat{\Omega})$ is the electron angular fluence
$\vec{r} = (x, y, z)$ is the spatial position vector
E is energy
$\widehat{\Omega} = (\mu, \eta, \xi)$ is the unit direction vector
$\vec{n}$ is the outward directed unit normal to surface δV

Equations 14a and 14b are subject to the conditions $\vec{r} \in V$, $\widehat{\Omega} \in 4\pi$, and $E > 0$.

The terms from the left side of equations 14a and 14b are summarized in Table 3.

Table 3: Left side terms of LBTE

$\hat{\Omega} \cdot \vec{\nabla}\Phi^{\gamma}$, $\hat{\Omega} \cdot \vec{\nabla}\Phi^{e}$ are the streaming operators
$\sigma_t^{\gamma}\Phi^{\gamma}$, $\sigma_t^{e}\Phi^{e}$ are the collision operators
$\sigma_t^{\gamma}(\vec{r}, E)$, $\sigma_t^{e}(\vec{r}, E)$ are the macroscopic photon and electron total cross sections respectively
$\frac{\partial}{\partial E}(S_R\Phi^{e})$ is the continuous slowing down operator, where $S_R(\vec{r}, E)$ is the restricted collisional plus radiative stopping power

The terms on the right side of equations 14a and 14b include scattering, production, and extraneous source terms. Table 4 summarizes these terms.

Table 4: Scattering and production sources LBTE

$q^{\gamma\gamma}(\vec{r}, E, \hat{\Omega}) = \int_0^{\infty} dE' \int_{4\pi} d\hat{\Omega}'\, \sigma_s^{\gamma\gamma}(\vec{r}, E' \to E, \hat{\Omega} \cdot \hat{\Omega}')\Phi^{\gamma}(\vec{r}, E', \hat{\Omega}')$
$q^{\gamma e}(\vec{r}, E, \hat{\Omega}) = \int_0^{\infty} dE' \int_{4\pi} d\hat{\Omega}'\, \sigma_s^{\gamma e}(\vec{r}, E' \to E, \hat{\Omega} \cdot \hat{\Omega}')\Phi^{\gamma}(\vec{r}, E', \hat{\Omega}')$
$q^{ee}(\vec{r}, E, \hat{\Omega}) = \int_0^{\infty} dE' \int_{4\pi} d\hat{\Omega}'\, \sigma_s^{ee}(\vec{r}, E' \to E, \hat{\Omega} \cdot \hat{\Omega}')\Phi^{e}(\vec{r}, E', \hat{\Omega}')$

In Table 4, $q^{\gamma\gamma}$ is the photon source resulting from photon interactions, $q^{\gamma e}$ is the electron source resulting from photon interactions, and q^{ee} is the electron source resulting from electron interactions. The macroscopic photon-to-photon differential scattering cross section is represented by $\sigma_s^{\gamma\gamma}$. $\sigma_s^{\gamma e}$ is the macroscopic photon-to-

electron differential production cross section and σ_s^{ee} is the macroscopic electron-to-electron differential scattering cross section [31].

Equation 14a and 14b include several assumptions. First both charge pair production secondary particles are assumed to be electrons instead of an electron and a positron. The partial coupling technique is assumed, whereby photons can produce electrons, but electrons do not produce photons. The energy from Bremsstrahlung photons is assumed negligible.

Acuros XB models the anisotropic behavior of the differential scattering and production sources by expanding the macroscopic differential scattering cross sections into Legendre polynomials. Angular fluence appearing in the scattering source is expanded into spherical harmonic moments. The reader is referred to the published literature for the details of this expansion [31].

Acuros XB uses several discretization methods to iteratively solve the LBTE. The calculation grid is determined using a spatially variable Cartesian grid, where the local element size is adapted to produce a finer mesh inside the beam and a coarser mesh in the penumbra region, umbra region, and outside the field. Spatial discretization is accomplished using a linear discontinuous Galerkin finite-element method, providing a linear solution variation throughout each element, with discontinuities permitted across element faces [34].

Energy treatment is handled by discretizing through standard multigroup methods [32]. The photon cross section library for Acuros XB includes 25 photon groups and 49 electron energy groups, although not all groups are used for energies lower than 20 MV.

The discrete ordinates method is used for angular discretization. The discrete ordinates method requires that the scattered photon fluence and scattered electron

fluence holds for a fixed number of directions, $\widehat{\Omega}_n$. The discrete directions are chosen from an angular quadrature set that also serves to compute the angular integrals for the generation of the scattering source. Square-Tchebyshev Legendre quadrature sets are used. The quadrature order ranges from N=4 to N=16 corresponding to 32 and 512 discrete angles respectively. The angular quadrature order varies by particle type and energy. Higher energy particles have longer mean free paths, or ranges for electrons. For each particle type, the angular quadrature order is increased with the particle energy.

When the energy of a particle falls below the cutoff energy, Acuros XB assumes that all remaining energy is deposited locally in that voxel. The cutoff energy for photons is 1 keV and for electrons is 500 keV.

The numerical methods used by Acuros XB require that a convergence tolerance be selected. Errors that result from convergence tolerance are reported to be on the order of 0.1% of the local dose in any given voxel [32].

The dose calculation in Acuros XB, for any output grid voxel i, of the problem is calculated according to equation 15.

$$D_i = \int_0^\infty dE \int_{4\pi} d\widehat{\Omega} \frac{\sigma_{ED}^e(\vec{r}, E)}{\rho(\vec{r})} \Phi^e(\vec{r}, E, \widehat{\Omega}) \tag{15}$$

where σ_{ED}^e is the macroscopic electron energy deposition cross sections in units of MeV/cm and ρ is the material density in g/cm^3.

The dosimetric accuracy of Acuros XB was explored by Han et al. in comparison to AAA and CCC using a Monte Carlo generated dose distribution as the reference calculation. Calculations were performed using a 30x30x30 cm^3 water phantom and 30x30x30cm^3 layered slab phantom. The slab phantom consists of a soft tissue layer 3 cm thick with a density of 1.0 g/cm^3, a bone layer 2 cm thick with a density of 1.85 g/cm^3, a lung layer 7 cm thick with a density of 0.26 g/cm^3, and a soft tissue layer 18 cm thick with a density of 1.0 g/cm^3.

Acuros XB was found to be closer to the Monte Carlo calculation than both AAA and CCC for all investigated plans. The average differences of depth dose profiles between Monte Carlo and Acuros XB, AAA, or CCC was within 1.1, 4.4, and 2.2%, respectively. The authors concluded that Acuros XB dose prediction ability is comparable to Monte Carlo and superior to current clinical convolution methods.

2.3.6 Monte Carlo

Complex systems are often difficult or impossible to solve analytically. Monte Carlo methods are a class of numerical computer simulation techniques that utilize statistical resampling to solve such systems. The Monte Carlo method was originally developed by a group of radiation physicists during the Manhattan nuclear project [35]. This class of numerical solvers has been applied to fields such as quantum physics, electrical and telecommunication engineering, computational biology, and weather forecasting.

When used in radiation transport, Monte Carlo techniques simulate the random trajectories of the individual particles by using machine generated random numbers to sample the probability distributions governing the physical processes involved [36]. A number of particles is simulated and followed through their interactions and energy loss.

Probability distributions dictate the fate of a particle as it interacts in the medium. By simulating large numbers of histories, information can be obtained about the average values of macroscopic quantities such as energy deposition. The accuracy of this method increases with the number of particle histories generated.

Monte Carlo methods are considered the gold standard for calculating dose distributions. They are the often used to extract dosimetric information when physical measurements are difficult or impossible to perform. These algorithms are not the most popular clinically because they consume great amounts of computing resources and therefore are not as fast as the methods previously described. To produce faster calculations electron and photon Monte Carlo rely on condensed history algorithms that employ some assumptions, yielding systematic errors.

2.3.7 EGSnrc

The Monte Carlo software that is used in this research utilizes EGSnrc. EGSnrc is a Monte Carlo simulator code package distributed by the National Research Council of Canada for applications in coupled electron-photon transport. It is a code that is based on the EGS4 software package originally developed at Stanford Linear Accelerator Center (SLAC). EGS is an acronym for **E**lectron **G**amma **S**hower.

EGSnrc has been widely used in medical physics applications. A search of the PUBMED US National Library of Medicine database at the time of this work for the search term ‘EGSnrc’ resulted in 348 unique publications that referred to EGSnrc.

The EGSnrc code has also been extensively benchmarked for applications in radiotherapy. One significant paper compared the results of three Monte Carlo systems (EGSNRC, GEANT4, PENELOPE) to published measurements of bremsstrahlung yield from thick targets for 10-30 MV beams [37]. Monte Carlo simulation was shown to be

capable of producing calculations of photon yield in the experimental geometry used to 5% out to 30°, 10% at wider angles, and photon spectra to 10% at intermediate photon energies, 15% at lower energies. EGSNRC and PENELOPE calculations were the most accurate codes showing results within 2 standard deviations of the measured photon yield at all beam energies and angles. GEANT4 was shown to be within 3 standard deviations.

2.3.8 BEAMnrc

BEAMnrc is a Monte Carlo simulation system for modeling radiotherapy sources. It is based on the EGSnrc code system for modeling coupled photon and electron transport [38]. The motivation behind developing BEAMnrc was to develop a user code for the EGSnrc system that addresses the challenges associated with modeling a radiotherapy source, such as a linear particle accelerator, while being accurate and straightforward for routine use. To that end, extensive work was done to document all aspects of the BEAMnrc user code. For example, all variables and input requirements are defined within the source code and scripts are available to extract stand-alone files containing these descriptions.

Figure 6 presents a schematic of the steps necessary for performing an accelerator simulation in BEAMnrc [39].

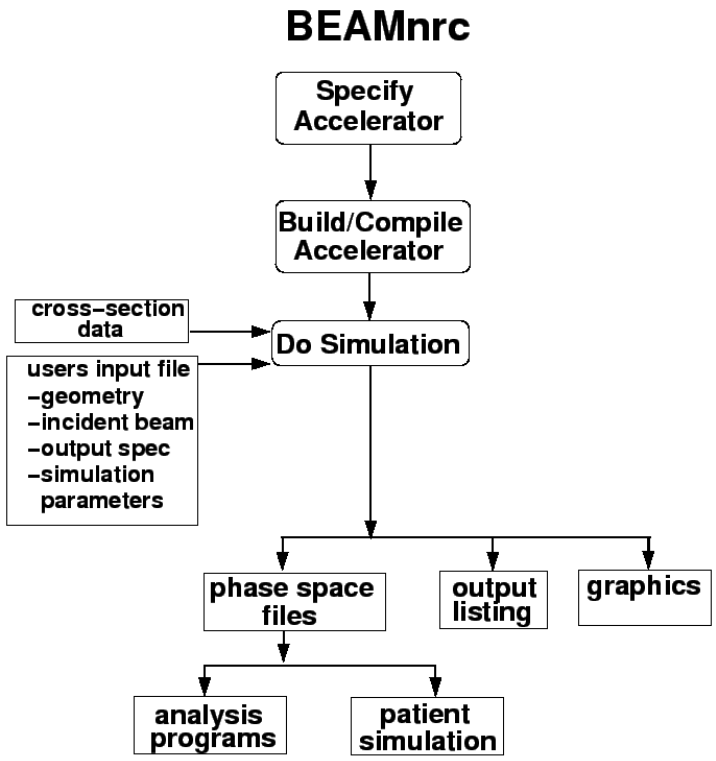

Figure 6: Steps required to simulate an accelerator in BEAMnrc

One of the outputs from such a simulation is a phase space file (i.e., the position, energy, direction, charge, and history tag for each particle) with size typically on the order of hundreds of megabytes. This type of output is generally the most important. The files contain the variables LATCH, E, X, Y, U, V, SIGN(W), WT, IQ and NPASS. The definitions of these variables are summarized in Table 5. The phase space data can be used as an input to an EGSnrc calculation to obtain dose to the patient. Various scripts are available to facilitate the conversion of computed tomography data into a format can be used directly in such an EGSnrc simulation. Phase space data generated with BEAMnrc was used to generate reference solutions for this work and in deriving primary and secondary photon fluence as will be discussed.

Table 5: Phase space file variables

Variable	Definition
LATCH	The history variable
E	Energy
X,Y	Position coordinates in the scoring plane
U,V	Direction cosines with respect to the X and Y axes
SIGN(W)	Sign of W, the direction cosine with respect to the Z axis
WT	Weight of the particle
IQ	Particle charge (-1, 0, +1)
NPASS	Specifies whether this is the first or later time that the particle has crossed this coring plane

2.3.9 DOSXYZnrc

DOSXYZnrc is a Monte Carlo simulation code based on EGSnrc. It is used for calculating dose distributions in a rectilinear voxel phantom. This is relevant in radiotherapy calculations as most if not all commercially available treatment planning systems calculate and report dose using a rectilinear voxel phantom decomposition.

DOSXYZnrc can be utilized with a variety of sources including full phase-space files from BEAMnrc and beams characterized using beam characterization models [40]. A companion program is available that is capable of reading in a CT data set of Hounsfield numbers and converting it into the information needed by DOSXYZnrc to simulate transport in a phantom.

2.3.10 Coarse Mesh Transport Method (COMET)

COMET is a **co**arse-**me**sh **t**ransport method that was developed by the Computational Reactor and Medical Physics Group at the Georgia Institute of Technology. COMET is based on incident flux response expansion theory in general geometry developed by Mosher and Rahnema [41]. In the cited work, the methods'

implementation was limited to 2-dimensional Cartesian geometry in which the energy variable was treated using multigroup theory. The original application was to solve the neutron transport equation using the deterministic discrete ordinates method in large heterogeneous problems with high fidelity and efficiency. Zhang and Rahnema extended this method to coupled photon-electron transport with the same fidelity and high efficiency [42]. This method, which is known as COMET-PE, is a hybrid stochastic/deterministic continuous energy transport method in which incident flux response expansion coefficients for each unique coarse mesh are generated *a priori*. The theory was developed in general geometry but implemented in 2-dimensional Cartesian geometry with a monoenergetic and monodirectional incident source. Using this implementation, Satterfield demonstrated the viability of COMET-PE in calculating dose distributions for radiation therapy problems [9]. Hayward and Rahnema subsequently extended the implementation of the COMET-PE method to a more general incident source distribution in angle and energy [43]. Using a heterogeneous interface phantom composed of water, aluminum, and lung it was demonstrated that the enhanced implementation of COMET-PE is capable of producing calculations that agree with a reference DOSXYZnrc calculation within 1.5% maximum and 1.5% root-mean-square error. COMET-PE was the basis for all COMET method calculations performed in this work.

As previously mentioned, COMET-PE is a hybrid stochastic and deterministic code/method that combines the accuracy of Monte Carlo with the precision of deterministic transport theory. In broad terms, the method solves the transport equation by coupling the stochastically generated response functions using a deterministic solver [44]. The response functions need only be generated once because they are a function

of material density and independent of the patient. Thus the computational time necessary for computing response functions is not included in a clinical calculation.

COMET utilizes the particle transport equation shown below in its' typical form.

$$\hat{\Omega} \cdot \vec{\nabla}\psi + \sigma_t(\vec{r}, E)\psi - \int_0^\infty dE' \int_{4\pi} d\hat{\Omega}' \, \sigma_s(\vec{r}, \hat{\Omega}, E; \hat{\Omega}', E')\psi = q(\vec{r}, \hat{\Omega}, E)$$

$$\vec{r} \epsilon V \tag{16}$$

The boundary condition is given in equation 17.

$$\psi(\vec{r}, \hat{\Omega}, E) = \gamma(\vec{r}, \hat{\Omega}, E)$$

$$\vec{r} \epsilon \partial V \tag{17}$$

$$\hat{n} \cdot \hat{\Omega} < 0$$

The variable $\psi(\vec{r}, \hat{\Omega}, E)$ represents the differential energy fluence (cm^{-2}). The differential energy fluence is a function of the phase space variables $\vec{r}$, $\hat{\Omega}$, and E. $\vec{r}$ represents the spatial variable, $\hat{\Omega}$ is the angle, and E is the energy (MeV). The spatial domain of the problem is given by a volume V. The external boundary of the system is ∂V, and the outward normal vector $\hat{n}$ is given with respect to this external boundary. The differential energy fluence can originate from a source that is either internal to the spatial domain or external to it. A description of the terms in equations 16 and 17 is provided in Table 6.

Table 6: Terms in the Boltzmann transport equation

$\hat{\Omega} \cdot \vec{\nabla}\psi$	Net energy of particles streaming out of the differential phase space $d\vec{r}d\hat{\Omega}dE$
$\sigma_t(\vec{r}, E)\psi$	Describes the removal of particles from the phase space due to collision interactions, σ_t is the total cross section
$\int_0^\infty dE' \int_{4\pi} d\hat{\Omega}' \, \sigma_s(\vec{r}, \hat{\Omega}, E; \hat{\Omega}', E')\psi$	Describes the distribution of particles emerging from scattering interactions, σ_s is the double differential cross section
$q(\vec{r}, \hat{\Omega}, E)$	Source internal to the problem spatial domain V
$\gamma(\vec{r}, \hat{\Omega}, E)$	Source external to the problem spatial domain V

As mentioned, the larger problem is decomposed into a set of smaller non-overlapping regions V_i. Each region composes a single coarse-mesh. Let ∂V_i denote the boundary of mesh V_i, let ∂V_{is} denote surface s of mesh i, and let $\hat{n}_{is}$ denote the outward unit normal on this surface. The transport equation is now represented by equation 18.

$$\hat{\Omega} \cdot \nabla\psi_i + \sigma_t(\vec{r}, E)\psi_i - \int_0^\infty dE' \int_{4\pi} d\hat{\Omega}' \, \sigma_s(\vec{r}, \hat{\Omega}, E; \hat{\Omega}', E')\psi_i = q_i(\vec{r}, \hat{\Omega}, E) \tag{18}$$

In this equation ψ_i is the fluence within the volume V_i. If s is an external surface ($\partial V_{is}, \subset \partial V$), the external boundary condition γ in equation 17 defines the incoming fluence. If s is not an external surface then it must be an internal surface ($\partial V_{is}, \subsetneq \partial V$), and the continuity condition in equation 19 determines the incoming fluence.

$$\psi_{is}^{-}(\vec{r},\hat{\Omega},E)=\psi_{\tilde{i}\tilde{s}}^{+}(\vec{r},\hat{\Omega},E)$$

$$\vec{r}\epsilon\partial V_{is} \tag{19}$$

$$\hat{n}_{is}\cdot\hat{\Omega}<0$$

In equation 19 + and – superscripts denote incoming and outgoing fluence respectively. The mesh index $\tilde{\imath}$ and the surface index $\tilde{s}$ define neighbors to surface s of mesh i such that $\partial V_{is}=\partial V_{\tilde{i}\tilde{s}}=(\partial V\cap\partial V_{\tilde{i}})$. The problem has now been decomposed into N local fixed source problems, which can be solved using Monte Carlo methods thereby generating a set of response functions.

The response function describes how a single mesh responds to internal and external source distributions. The response function for a particular mesh is a combination of solutions to many simpler problems. Such problems are defined as either surface-to-volume or volume-to-volume [42, 45]. A surface-to-volume response is generated by imposing a unit incoming fluence on a single surface of a mesh. The unit incoming fluence can also be considered as a surface source. The incoming fluence distributions are chosen from a set of basis functions and the process is repeated for each member of the set of basis functions. A similar process is performed to compute volume-to-volume responses that correspond to the result of imposing a unit volumetric source distribution on a single mesh.

Both types of sources correspond to a fixed basis set. They are therefore known and can be pre-computed and stored. An arbitrary source can be constructed by superposition of the pre-computed responses. Outgoing and incoming fluences on the

mesh surfaces are found by expanding the same basis functions. Because of this, the response functions can be connected to solve the global problem.

In order to solve the global problem, the response to a fixed source must be calculated. An external source can be treated as either an incoming fluence or alternatively it can be considered as the source resulting from the distribution of first-collisions. The global solution can then be found using an iterative scheme that refines the fluence distributions that couple the meshes. The iteration converges the initially discontinuous fluence distributions at the mesh interfaces to a continuous distribution. After a solution has converged, the energy distribution can be rapidly computed. See references [10, 42] for a more detailed description of the COMET-PE method.

CHAPTER 3

SOURCE TREATMENT IN TREATMENT PLANNING

A clinical radiation beam generated in a linear particle accelerator is composed of more than the photons created in the target of the machine. A typical methodology for handling the various components of a clinical radiation beam is to divide the source into three components: primary photons, extra-focal photons, and contamination electrons [46].

Primary photons are generated by electron bremsstrahlung interactions in the target and do not interact further in the linac head, although they may have further interactions in the target. Extra-focal photons may be generated or scattered in the various components of the head of the linac other than the target, such as the primary collimator, the secondary collimator, or the flattening filter. Electron contamination describes the dose deposition in the build-up region of the phantom or patient that has not been accounted for by the primary and extra-focal photon source components. The electron contamination includes any contribution from positrons as well.

It is common when modeling a clinical photon beam to treat each of these components separately. This approach is used by the Eclipse treatment planning system in the implementation of both the Analytic Anisotropic Algorithm (AAA) and the Acuros XB (AXB) dose calculation algorithm.

A review of the Eclipse triple source implementation is included in section 3.1. This is instructive both to introduce key concepts and as a basis of comparison for the current work.

3.1 AAA/AXB Source

Eclipse uses a parameterized model of the radiative output from a medical linear accelerator that is based on Monte Carlo simulations of the treatment unit head for both the AAA and AXB algorithms. One advantage to this approach is that the parameters of the model can be adjusted so that the phase-space source can be constructed to match the radiation produced by a specific accelerator. The adjustments are made based on comparisons of calculated dose distributions to measurements made on-site in a large water phantom. All model parameters for AAA and AXB are computed in a water-equivalent medium.

One important parameter is the photon energy spectrum. As indicated the spectrum is initially determined through Monte Carlo simulation of the Bremsstrahlung interactions of electrons in the target. A sample photon spectrum for a 6 MV beam is shown in Figure 7.

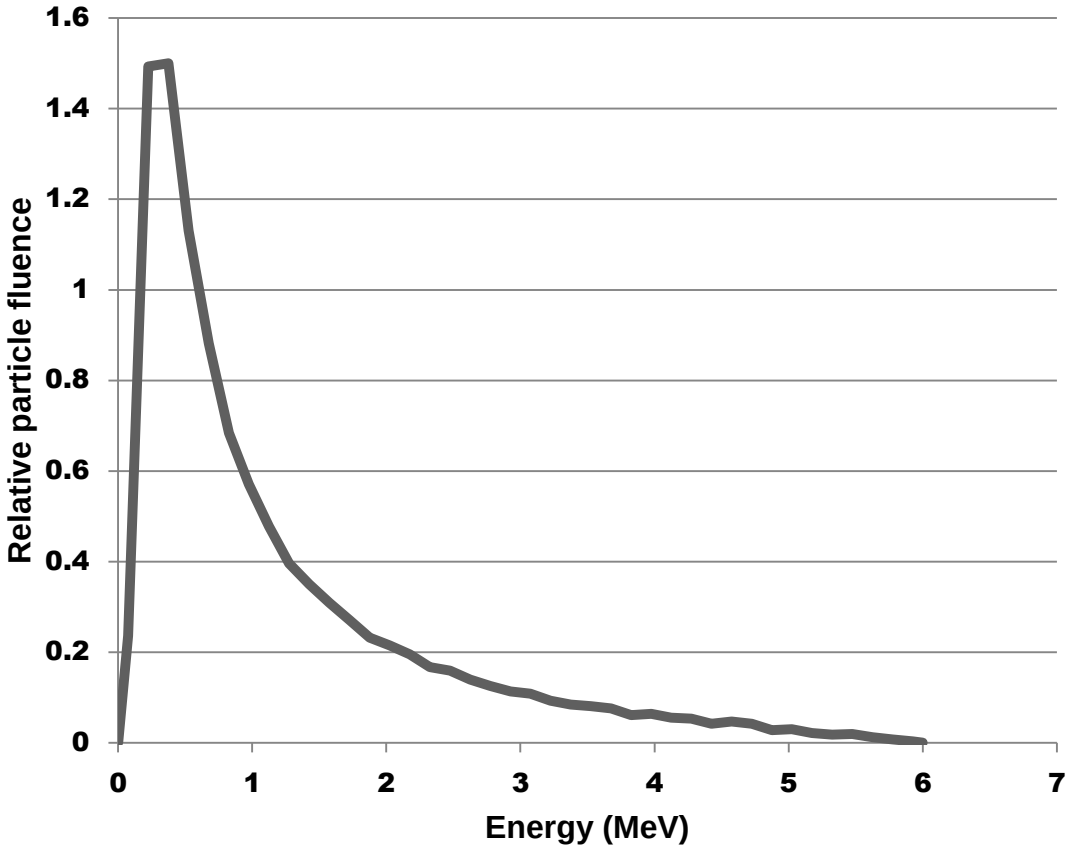

Figure 7: Example photon spectrum for 6 MV photons

Another important source parameter that must be modified is the mean radial energy with distance from the central axis of the beam. The spectral shift that occurs off central axis is due primarily to the influence of the flattening filter. Figure 8 shows the rapid falloff of mean energy that occurs with radial distance.

Figure 9 illustrates the varying intensity of the photon beam with distance from the central axis. This parameter is also the result of the flattening filter in the head of the machine. The flattening filter in this example is considered to be made of copper. The intensity is computed as the photon energy fluence (number · energy of photons) as a function of the radial distance from the beam central axis.

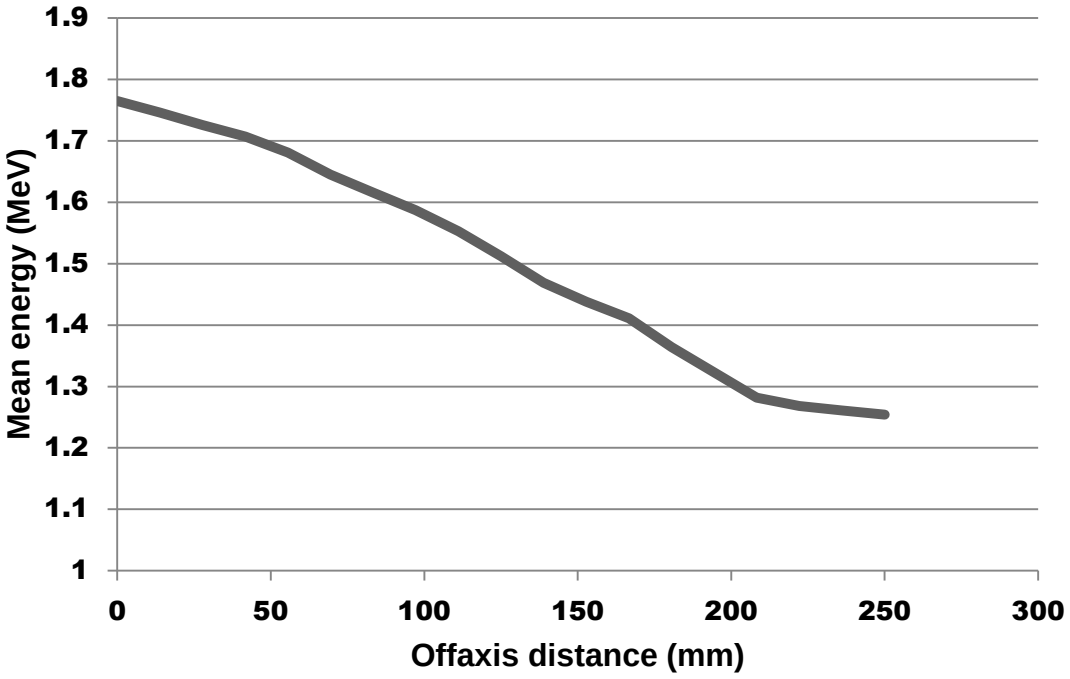

Figure 8: Mean radial energy as a function of radial distance from central axis of a 6 MV photon beam

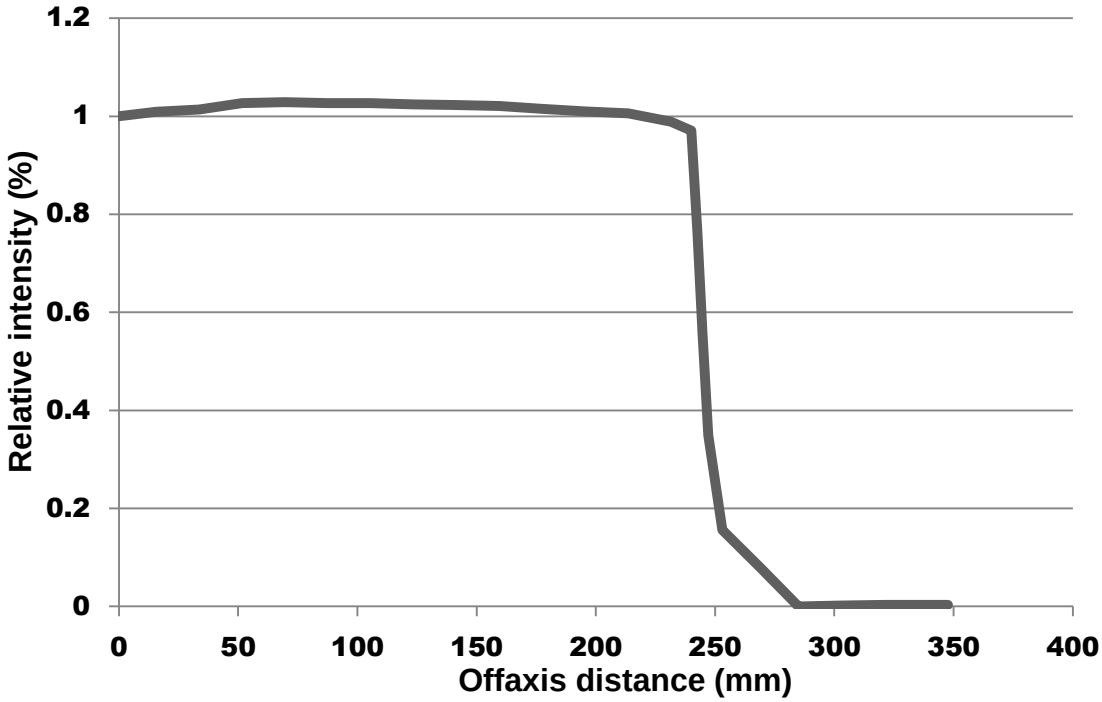

Figure 9: Intensity profile from a 6 MV photon beam

The AAA and AXB algorithms use a source model that is divided in the usual way into the following main components: primary photon energy fluence (primary source), extra-focal photon energy fluence (extra-focal source), and contaminating electron fluence (electron contamination source) [47]. A diagram of the head of the accelerator is shown in Figure 10.

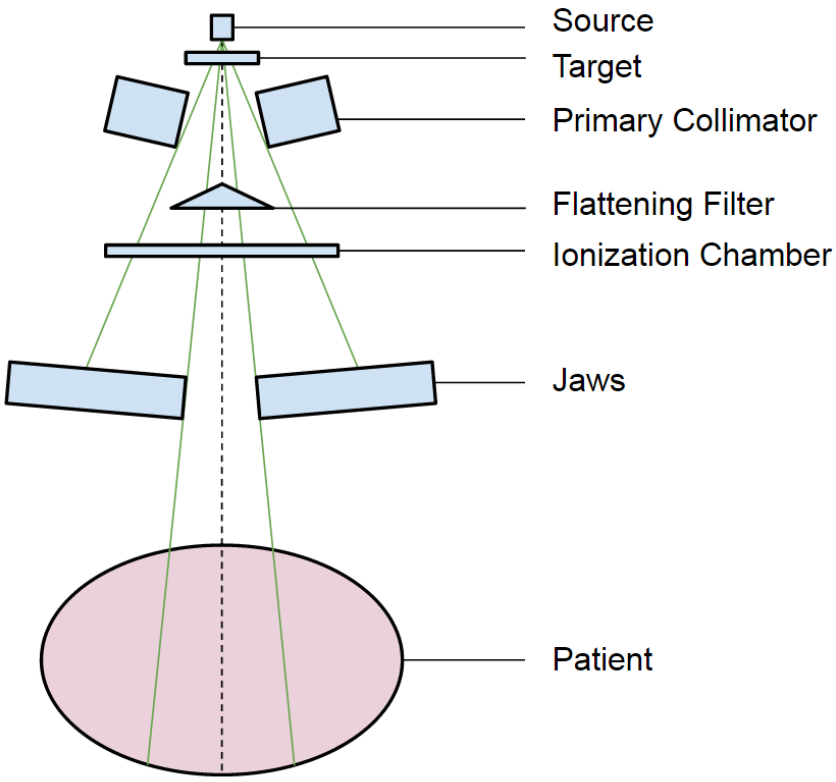

Figure 10: Components of a linear accelerator head

The primary source is a point source located at the target plane. It models bremsstrahlung photons that do not interact in the treatment unit head. Separate energy spectra for every fanline of the broad beam are derived from the mean energy curve.

The extra-focal source is a Gaussian plane source located at the bottom plane of the flattening filter. It models the photons that are created as a result of interactions in the accelerator head outside the target. The extra-focal photons are assumed to be uniformly distributed across the broad beam, and they are modeled with a secondary source having a configurable intensity.

Electron contamination models electrons produced from photon interactions in the head of the accelerator. The electron contamination strongly depends on the field size and beam energy. In AAA and AXB electron contamination is modeled with a depth dependent curve that describes the total electron contamination dose at a certain depth.

CHAPTER 4

COMET SOURCE

In order for COMET to be useful in clinical application the radiation source should have characteristics that closely model the radiation produced by a linear particle accelerator. The model used by AAA/AXB has proven to produce excellent results when implemented in the Eclipse treatment planning system [8, 48, 49]. It would therefore be desirable to implement the same source model into COMET. This implementation would have the added advantage of facilitating a more direct comparison of the performance of COMET versus AAA and AXB. It was the original intent of this work to implement such a source model. During the course of the project, it was realized that not all of the information regarding how the AAA/AXB source is implemented in Eclipse is readily available. Additionally a number of assumptions were necessary to adapt the model for use in COMET. As the assumptions grew in number, it became clear that the aforementioned benefits of using the AAA/AXB source were increasingly less applicable. The performance of such an implementation could not be assumed to produce comparable results to those previously studied. Also with such assumptions a direct comparison of the performance of COMET with AAA/AXB was not truly direct as the input radiation from the source was not necessarily identical.

The focus was therefore shifted to finding an efficient and accurate method of modeling the radiation from a clinical accelerator that works within the COMET framework. The idea of separating the source into three components is conceptually sound and has been demonstrated to be effective [46]. It was retained in this work, with the definitions of each component remaining the same, namely: primary photons are

those which are directly from the target and reach the patient without any interactions elsewhere, extra-focal photons are those which are generated or scattered in the component modules other than the target, and contamination electrons (including positrons) are those created anywhere in the accelerator head.

4.1 Primary Source

As implied by the name, the majority of photons that reach the patient originate in the primary source. The contribution of direct photons to the photon energy fluence in a 10x10 cm^2 field with a 6 MV beam energy varies between 92% and 97% [50]. An accurate representation of the primary source is therefore critical in any attempt to model the energy fluence from a linear accelerator.

Some important characteristics of the primary source that must be accounted for include the energy spectrum, angular distribution, and change in energy with radial distance from central axis. These characteristics were modeled in this research by first dividing the photon distribution into energy bins and expanding the angular distribution of photons in each bin using an orthonormal basis. The background and justification of this technique is discussed further in the following sections.

4.1.1 Harmonic Expansion Background

Harmonic functions are the solutions to Laplace's equation. They are widely used by many sciences [51]. A useful subset of harmonic functions is spherical harmonics, which is the angular portion of harmonic functions. In other words, spherical harmonics are the solutions to Laplace's equation when restricted to the sphere. They have been used in physics to solve potential problems associated with the heat equation, gravitation, and electromagnetics [52, 53]. In quantum physics and chemistry, they have

been used to model the electron configuration of atoms and quantum angular momentum [54, 55]. In three dimensional computer graphics, spherical harmonics have been extensively applied to a variety of topics but especially to those involving lighting [56-59].

Spherical harmonics are an analog to the Fourier series but defined for the sphere. Just as the Fourier series is used to expand periodic signals into a sum of sines and cosines, spherical harmonics can be used to expand a spherical function into a set of coefficients and basis functions. This means that a set of coefficients can be calculated and then later used to analytically reconstruct an approximation of the original function. The power of this method is illustrated in Figure 11. As is evident in the figure, the reconstruction is increasingly accurate as the expansion order increases. The details of spherical harmonic expansions are well document and the reader is referred to the literature for an in depth analysis.

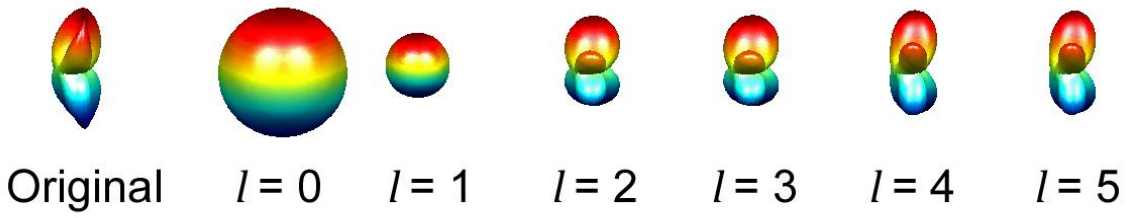

Figure 11: Spherical harmonic expansion with increasing orders of approximation

However, the primary source from a linear accelerator is not well modeled with a spherical function but rather hemispherical. In his paper on hemispherical harmonics, Gautron points out that hemispherical functions introduce discontinuities in the spherical domain at the boundary of the hemisphere [60]. Therefore their accurate representation

using a spherical basis requires a large number of coefficients. It is therefore logical to utilize hemispherical harmonics in the expansion of the primary source.

4.1.2 Hemispherical Harmonics

A detailed explanation of hemispherical harmonics as they are defined for this work can be found in the paper by Hayward and Rahnema [10]. Their work demonstrates that the hemispherical harmonic basis used represents a complete and orthonormal basis. Amongst other things, orthogonal and orthonormal basis functions allow the expression of any piecewise continuous function over their domain as a linear combination of an infinite series of linearly independent basis functions.

In general, to approximate a given function f to an arbitrary accuracy, coefficients k_n are calculated that describe how much each basis function p_n is like f. This is done by integrating the product shown in equation 20 over the domain of f.

$$\int f(x)p_n(x)dx = k_n \tag{20}$$

This process is referred to as a projection or expansion of the original function. The inverse process is called reconstruction and is performed by linear combination of all of the basis functions scaled by their associated coefficients as shown in equations 21 and 22.

$$f(x) = \sum_{n=0}^{\infty} k_n p_n \tag{21}$$

$$\tilde{f}(x) = \sum_{n=0}^{N} k_n p_n \tag{22}$$

Equation 21 shows an exact reconstruction and equation 22 is an approximate reconstruction truncated at an arbitrary expansion order N.

The hemispherical harmonics basis functions used in this work are defined in spherical polar coordinates as

$$\widehat{H}_{lm}(\theta,\phi) = \begin{cases} \frac{2}{\sqrt{\pi}} \hat{J}_l^{(-m)}(2\cos\theta - 1)\sin(-m\phi), & m < 0 \\ \frac{2}{\sqrt{\pi}} \hat{J}_l^{(0)}(2\cos\theta - 1), & m = 0 \\ \frac{2}{\sqrt{\pi}} \hat{J}_l^{(m)}(2\cos\theta - 1)\cos(m\phi), & m > 0 \end{cases} \tag{23}$$

for $l \geq 0$ and $|m| \leq l$ where $\hat{J}_l^{(m)}(x)$ is a normalized adjoint Jacobi function. The adjoint Jacobi functions are defined as

$$\hat{J}_l^{(m)}(x) = c_{lm}(1-x^2)^{\frac{m}{2}} \frac{d^m}{dx^m} P_l^{(0,1)}(x) \tag{24}$$

where c_{lm} is a constant factor chosen such that

$$\int_{-1}^{1} dx(1+x)\left(\hat{J}_l^{(m)}(x)\right)^2 = 1. \tag{25}$$

The $P_l^{(0,1)}(x)$ term in equation 24 is a Jacobi polynomial. Jacobi polynomials are orthogonal on the interval [-1,1] with respect to the weighting function $w_{(\alpha,\beta)} = (1-x)^{\alpha}(1+x)^{\beta}$. They can be defined as

$$P_n^{(\alpha,\beta)}(x) = \frac{(-1)^n}{2^n n!\, w_{(\alpha,\beta)}(x)} \frac{d^n}{dx^n}\left[w_{(\alpha,\beta)}(x)(1-x^2)^n\right]. \tag{26}$$

The index l represents the band. An order n hemispherical harmonic expansion uses all of the basis functions through degree $n-1$.

The hemispherical harmonics presented are orthonormal by the condition given in equation 27.

$$\int_{\boldsymbol{H}} d\widehat{\Omega}\left(\hat{n}\cdot\widehat{\Omega}\right)\widehat{H}_{lm}\left(\widehat{\Omega}\right)\widehat{H}_{l'm'}\left(\widehat{\Omega}\right) = \delta_{ll'}\delta_{mm'} \tag{27}$$

$\boldsymbol{H}$ denotes the hemisphere such that $\left(\hat{n}\cdot\widehat{\Omega}\right) > 0$ for some unit normal $\hat{n}$, and δ is the Kronecker delta. The coordinate system is chosen such that

$$\begin{gathered}\int_{\boldsymbol{H}} d\widehat{\Omega} = \int_0^{2\pi} d\phi \int_0^{\pi/2} d\theta \sin\theta \\ \hat{n}\cdot\widehat{\Omega} = \cos\theta.\end{gathered} \tag{28}$$

There are several methods for visualizing harmonic basis functions. One standard way is to distort a unit sphere/hemisphere, by scaling each point radially by the absolute value of the function and coloring it based on the sign. Figure 12 uses this method to visualize the first few hemispherical harmonics based on the formulation by Gautron, et al. [60]. These are the more commonly used hemispherical harmonic basis functions. Figure 13 uses the same method to visualize the first few hemispherical harmonics based on the formulation by Hayward and Rahnema [10]. The plots are colored based on the sign. Red represents positive values and green represents

negative. The plots were generated using a purpose built Matlab R2009b (The MathWorks, Inc. Natick, MA) function. The main difference between these two approaches is that Gautron uses Legendre Polynomials as the orthogonal basis functions on which the hemispherical harmonics are built and Hayward, et al. uses adjoint Jacobi basis functions. The orthogonality condition also differs between the two sets of basis functions. This will become important later but it is worth noting now because although the basis derived by Gautron is more commonly used there are sound reasons for choosing the basis formulated by Hayward and Rahnema for this work.

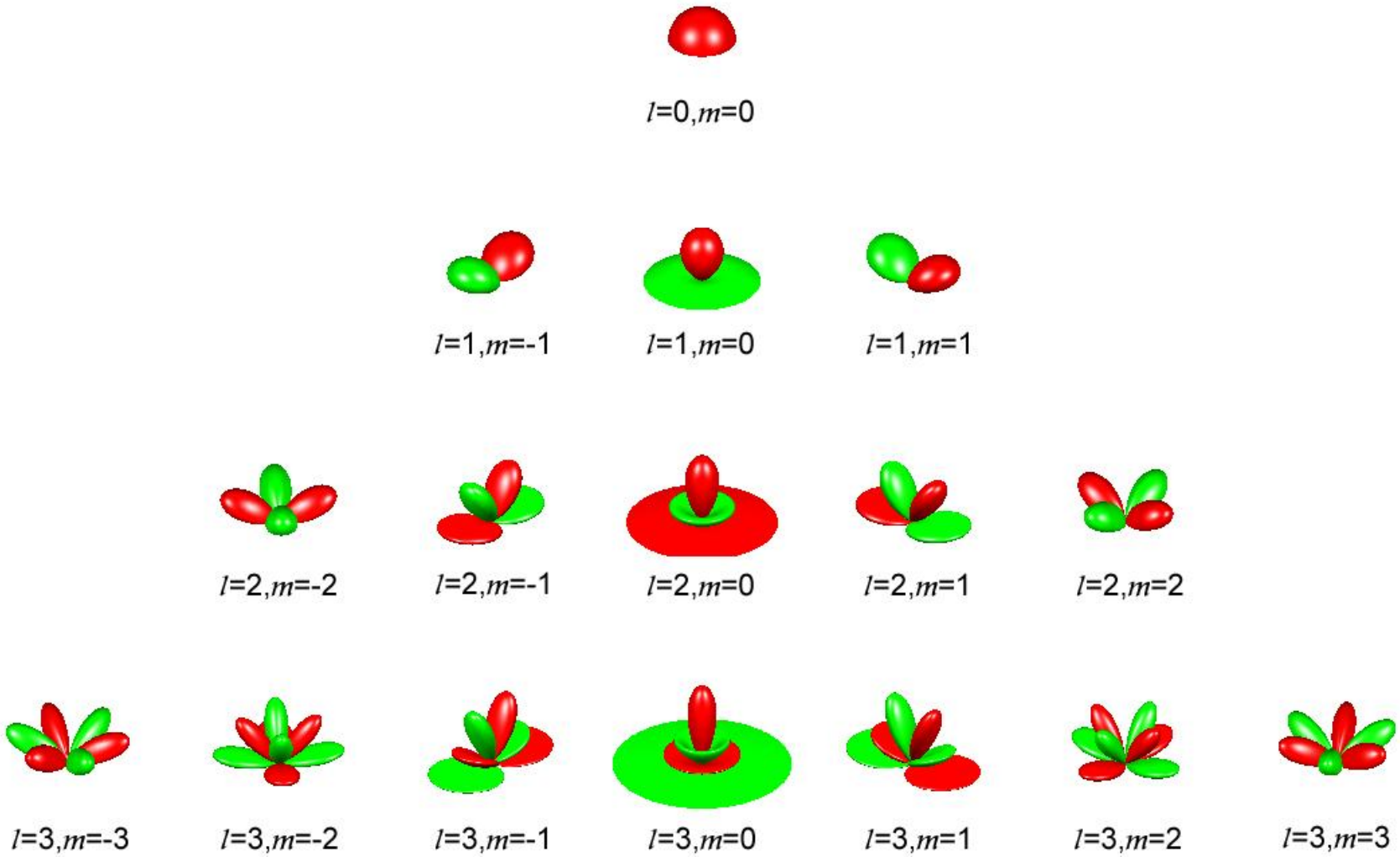

Figure 12: The first four hemispherical harmonics from the basis proposed by Gautron et al.

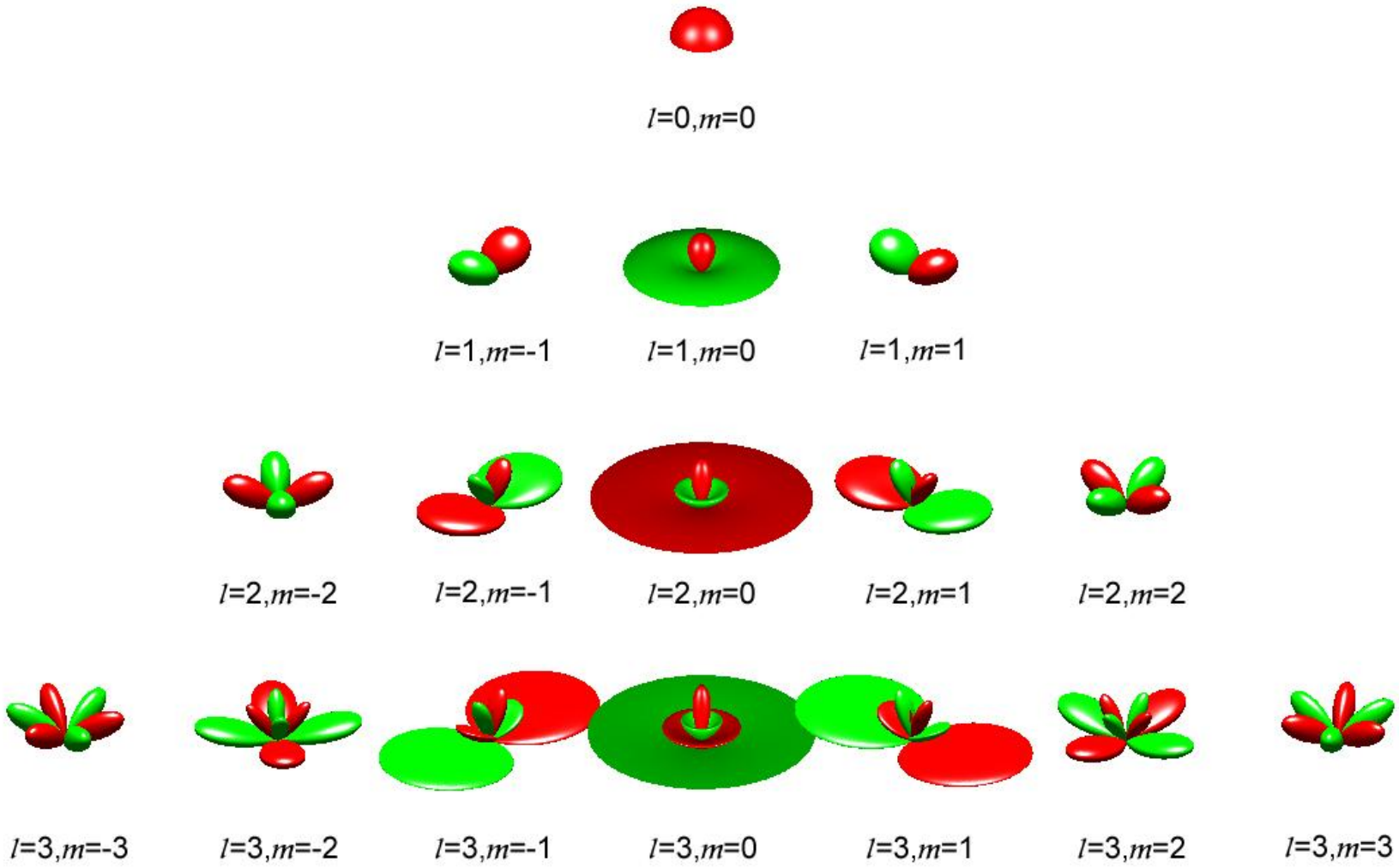

Figure 13: The first four hemispherical harmonics from the basis proposed by Hayward et al.

The functions in the central columns of Figures 12 and Figure 13 are called zonal harmonics (ZH). They have the property of rotational symmetry in the azimuthal direction. This is of note because accelerator fluence (ignoring jaws and multileaf collimators) has only very weak azimuthal dependence. This conclusion is supported by the absence of any correction for azimuthal dependence in the treatment planning algorithms in common use [23, 25, 26, 28]. Dropping all expansion coefficients with $m \neq 0$ and assuming azimuthal symmetry is an appealing option for expansion techniques because far fewer expansion coefficients will be necessary. Both methods were explored in this work.

Using the process of expansion and reconstruction previously described, hemispherical harmonics can be used to approximate functions on the hemisphere. Figure 14 shows the expansion of the clamped cosine function shown in equation 29, with increasing orders of approximation.

$$f(\theta, \phi) = \max(0{,}5\cos(\theta) - 4) \tag{29}$$

Note that the same coloring was used as in Figures 12 and 13, so that red represents positive values and green represents negative. The clamped cosine function presented is a smooth function and is well approximated with a small number of expansion coefficients. The number of coefficients necessary to approximate a function in this manner is governed by $(l+1)^2$. For an expansion order of $l = 8$ the number of coefficients required is 81. It is clear that the number of expansion coefficients can grow rapidly and must be taken into consideration when performing an expansion as the size can quickly become unmanageable. If only the zonal harmonics are considered, the

number of expansion coefficients is governed by the equation $l + 1$. So for an expansion order of $l = 8$, only 9 coefficients are necessary. This clearly demonstrates the advantage of being able to assume azimuthal symmetry.

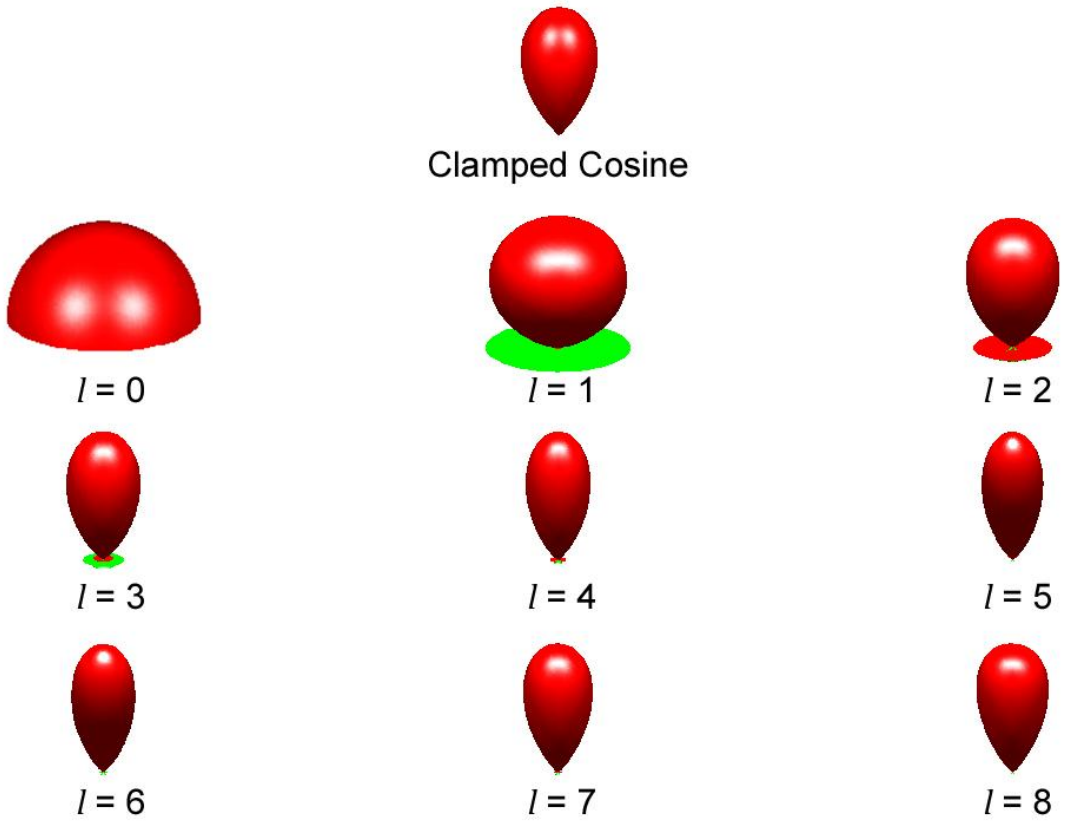

Figure 14: Hemispherical harmonic expansion of clamped cosine function with increasing orders of approximation

4.1.3 Monte Carlo Functional Expansion Tallies

It has now been demonstrated that a hemispherical function can be expanded and reconstructed to an arbitrary order of approximation using hemispherical harmonics. To use this method to model the energy fluence from a linear accelerator, the functional expansion tally approach can be used.

The functional expansion tally (FET) method has been shown to be an effective approach for constructing functional estimates of unknown tally distributions produced by Monte Carlo simulation [61]. As previously discussed Monte Carlo methods are widely used in particle transport and radiative transport calculations to model processes within complex systems. In this approach, particles are sampled from a source distribution. The trajectories of the individual particles are tracked using machine generated random numbers to sample the probability distributions that govern the physical processes involved. Each particle is typically tracked until it leaks from the system or is absorbed.

Monte Carlo techniques in particle transport are commonly used to estimate particle flux or reaction rates. Such values can be calculated by keeping track of a tally during the simulation. A common value that is tracked by use of a tally is the number of particles that cross a surface for use in the statistical estimation of planar fluence. Such methods are well suited to estimating integral values, such as total reactions, particle current, etc.

To gain information about the higher order shape of simulations from Monte Carlo simulations, the traditional approach has been to divide the phase space into bins and calculate an average over each bin, resulting in a histogram approximations of the true tally distribution [61]. It is instructive at this point to reintroduce a common result of the Monte Carlo simulation of the head of a linear accelerator known as the phase space

file. A phase space file contains data relating to particle position, direction, charge, energy and weighting for every particle crossing a user defined scoring plane [39].

To obtain a finer resolution for values such as angular distribution of the photons emerging from a radiation source a larger number of bins must be used. If one is using the data from a Monte Carlo generated phase space file to fill the bins in the histogram, then there are a finite number of particles available. Meaning when there are a larger number of bins then there are fewer particles per bin which can lead to large statistical uncertainties.

The functional expansion tally approach is an alternative method for obtaining high order shape information from Monte Carlo simulations. Chadsey introduced the FET method in 1975 and initially used it to estimate spherical harmonic expansion coefficients of the angular distribution of X-ray photoemission [62]. The data from a Monte Carlo run can be used to estimate functional expansion coefficients of the true distribution with respect to a set of orthogonal basis functions. There are several advantages of this method over the traditional histogram approach. First, every tally in the region contributes to every expansion coefficient, yielding information regarding the shape of the phase space distribution as well as its average value. Second, it is possible to choose a set of basis functions such that the lowest order term preserves the integral quantity over the region of interest. So the average value estimated by the conventional tallies is preserved. Third, the estimated solution is a continuous function, which in many cases is more useful than a histogram for extensive calculation and analysis. Griesheimer, et al. demonstrated that for a sufficiently smooth distribution the functional expansion tally approach converged faster, and achieved a lower residual error, than a histogram approach [61].

4.1.4 Derivation of the FET Method

The following is a summary of the derivation presented by Griesheimer et al, in their paper on the convergence properties of Monte Carlo functional expansion tallies [61]. Consider a particle transport problem that is simulated using the Monte Carlo method, in which a random variable x is distributed according to a particular probability density function $P(x)$. The probability density function (PDF) tells us the relative probability that a variable will take on a specific value. Traditionally to obtain shape information about the PDF, the domain of the random variable would be divided into bins $b = [1,2,\dots,M]$ and then the number of events that occur in each bin N_b are counted during the simulation. The total score in each bin divided by the number of independent trials, N, is an unbiased estimator for the probability that a given sample will fall within the bin, as seen in equation 30:

$$E\left[\frac{N_b}{N}\right] = P(x_{b-1} \leq x < x_b) \tag{30}$$

where x_{b-1} and x_b denote the bounds of bin b. The process can be repeated for all bins and the result is a histogram that approximates the actual PDF shown in equation 31 and 32,

$$P(x) = \sum_{b=1}^{M} \left(\overline{P_{M,b}^{hist}}(x) + O[\Delta x_b] \right) \tag{31}$$

$$\overline{P_{M,b}^{hist}}(x) = \frac{P(x_{b-1} \leq x < x_b)}{\Delta x_b} \tag{32}$$

where Δx_b is the width of bin b, and $\overline{P_{M,b}^{hist}}(x)$ is the true value of the histogram in bin b. As the number of bins M increases, the error associated with truncating the distribution decreases and the histogram approximation converges to the continuous distribution.

The FET uses a complete set of basis function to expand an unknown PDF $P(x)$. Using a set of independent samples from $P(x)$, an estimate of the coefficients of the expansion can be made. This is shown by letting $\{\psi_n\}_0^\infty$ be a complete orthogonal set with respect to a weighting function ρ in $L_\rho^2(\Gamma)$, the space of all square integrable functions over some bounded domain Γ. Any $P(x)\epsilon L_\rho^2(\Gamma)$ can be written as

$$P(x) = \sum_{n=0}^{\infty} \bar{a}_n \, k_n \psi_n(x), \tag{33}$$

where $\bar{a}_n$ is the true nth expansion coefficient defined by the inner-product,

$$\bar{a}_n = \int_\Gamma \psi_n(x)\rho(x)P(x)dx, \tag{34}$$

and k_n is the normalization constant for the nth basis function,

$$k_n = \frac{1}{\|\psi_n\|^2}. \tag{35}$$

To create a functional approximation to $P(x)$, the expansion coefficients $\bar{a}_n$ must first be determined. The integral shown in equation 34 can be estimated by Monte Carlo integration methods in order to determine the coefficients. It can be shown that the statistic in equation 36 is an unbiased analog estimator for the true expansion coefficient $\bar{a}_n$, where N is the number of histories tallied [63, 64].

$$\hat{a}_n = \frac{1}{N}\sum_{i=1}^{N} \psi_n(x_i)\rho(x_i) \tag{36}$$

4.1.5 Phase Space Files for 6 MV

It has been demonstrated that the functional expansion tally method can be used effectively to extract source shape information from a Monte Carlo simulation. In this research, phase space files generated by Cho et al. were used to provide the particle simulations necessary to calculate primary photon expansion coefficients with the hemispherical harmonic basis proposed by Hayward and Rahnema [10, 65].

The 6 MV photon energy is a logical starting place for this work because it is a common and well researched energy in radiotherapy. Although a search revealed no hard statistics, it is likely that 6 MV is the most selected energy currently used for external beam therapy treatments.

In their research Cho et al., produced reference phase space data (RPSD) for the 6 MV photon beam from Varian 2100 series linear accelerators [65]. This data was acquired using the BEAMnrc/DOSXYZnrc code system with 6.2 MeV electrons striking a target to produce the typical 6 MV clinical photon beam. A spread of 3% full width at half maximum energy and 1.0 mm full width at half maximum radial spread of the Gaussian

electron pencil beam incident on the target were implemented. Detailed specifications provided by the manufacturer were used to model the head of the linear accelerator for simulation. The target, primary collimator, flattening filter, monitor chamber, upper (Y) and lower (X) jaws were modeled. The phase space data were collected at a plane located right below the lower jaws.

The phase space data generated was matched to measured reference photon dosimetry data constructed by compiling average data based on the analysis of more than 50 sets of measured data from the Radiological Physics Center (RPC) at MD Anderson, and 10 sets of clinical dosimetry data obtained from 10 different institutions participating in the RPC's quality assurance monitoring program. The matching was performed by varying the energy (E_e) and the radial spread (R_e) of a Gaussian electron beam incident on the target. All other parameters that might be included in the simulation were kept constant including the densities of the target and flattening filter. It was assumed that the material specifications provided by the manufacturer were accurate.

Upon completion of the matching process the reference phase space data has been demonstrated to be capable of producing dosimetric results that agreed with reference photon dosimetry data within 1% or 1 mm for depth dose. Such a high level of accuracy is obviously desirable in a project such as this and so the RPSD was chosen for use in this work.

4.1.6 Reading Phase Space Data and Primary Fluence Expansion

The reference phase space file set produced by Cho et al. consists of 7 files produced for the following field sizes: 4x4, 6x6, 10x10, 15x15, 20x20, 30x30, and 40x40 cm^2. All of the files sizes are on the order of 1-2 GB. The phase space files are in

binary format and so a custom Fortran90 code called *phase_source* was developed to read the files, one particle at a time, and perform the functional expansion tally to generate expansion coefficients. The LATCH parameter was used to sort the particles into primary, extra-focal, and electron.

The distance from the target to the scoring plane of the phase space files is given as the bottom surface of the lower collimator jaw. A numerical value is not explicit in the file set. The AAA and AXB algorithms assign a value of 44.5 cm to the bottom of the lower collimator jaw. The schematics of the 2100C linear accelerator report a distance of 44.43 cm from the target to the bottom of the lower collimator jaw [66]. An experiment was performed to discover the target to scoring plane distance of the reference phase space data.

The distance of the scoring plane to the source along the z axis (the axis from source to the isocenter of the machine), was determined by backprojecting the primary photons from their position in the scoring plane to their z-intercept point and averaging those values. Table 7 summarizes the results for the 4x4, 10x10, 20x20, and 40x40 cm^3 field sizes.

Table 7: Source to phase space scoring plane distances

Field Size (cm^2)	Average Source to Scoring Plane Distance (cm)	Standard Deviation
4x4	44.48	0.56
10x10	44.47	0.54
20x20	44.39	0.47
40x40	44.26	0.40

The average distance of the values reported in Table 7 is 44.4 cm which is remarkably close to the reported value of 44.43 cm and 1 mm from the value used by AAA and AXB of 44.5 cm. For the sake of consistency between the calculation methods used in this work, a value of 44.5 cm was adopted as the source scoring plane distance. The source to isocenter distance was therefore maintained at 100 cm.

The *phase_source* Fortran code performed in-group expansions using the same energy groups that are used in the spectrum when generating necessary material cross section data in the COMET code. The energy groups are summarized in Table 8. The primary source is then defined as 14 sources of different energies.

Table 8: Energy groups used for in-group expansion

$6.0 \leq E < 6.5$
$5.5 \leq E < 6.0$
$5.0 \leq E < 5.5$
$4.5 \leq E < 5.0$
$3.5 \leq E < 4.5$
$3.0 \leq E < 3.5$
$2.5 \leq E < 3.0$
$2.0 \leq E < 2.5$
$1.5 \leq E < 2.0$
$1.0 \leq E < 1.5$
$0.5 \leq E < 1.0$
$0.25 \leq E < 0.5$
$0.05 \leq E < 0.25$
$E < 0.05$

The angular component of the fluence of each of the in-group sources that comprise the primary source is accounted for by the hemispherical harmonic expansion. The relative fluence of each in-group expansion is determined by normalizing the expansion coefficients by the total statistical weight within the energy group. This approach means the relative fluence is being approximated by the FET method instead of the expected value of the fluence. This formulation is used so that the photonic spectrum can be applied separately. In the AAA and AXB source model the spectrum is optimized so that the calculated results match a measured data set. Separating the spectral component leaves this option open for future work.

The equation for approximating an in-group expansion coefficient can be seen in equation 37. Note that a single index n is used for projection coefficients l and m.

$$\hat{a}_n = \frac{1}{w_{tot}} \sum_{i=1}^{N} w_i H_n(\hat{\Omega}_i) \tag{37}$$

In equation 37 N is the number of particle histories, H_n represents the hemispherical harmonic basis functions, w_i is the statistical weight, w_{tot} is the total in-group statistical weight, and $\hat{\Omega}$ is the angle. All primary particles in the phase space file were used to generate the expansion coefficients. Such calculations are performed when establishing the source model but are not repeated. They do not therefore contribute to the clinical calculation time for patient related dosimetry. The total time to calculate the expansion coefficient from a reference phase space file depends greatly on the expansion order and is typically 0.5 to 4 hours.

For dosimetric calculations in COMET, a reconstruction must be performed. This was accomplished for each energy group in the usual way through linear combination of

all basis functions scaled by their associated coefficients. The equation governing the primary fluence reconstruction is shown in equation 38,

$$\phi(\hat{\Omega}) = \sum_{n=0}^{\infty} \bar{a}_n H_n(\hat{\Omega}) \tag{38}$$

where ϕ represents the primary fluence, $\bar{a}_n$ represents the true expansion coefficient, and $\{H_n\}_0^\infty$ are the hemispherical harmonic basis functions that form a complete set over $\hat{\Omega}$. The expansion coefficients are defined exactly in equation 38, but for calculation purposes are approximated using equation 37 and the expansion order is necessarily truncated.

The value of using the hemispherical harmonic basis formulated by Hayward and Rahnema is now evident. Consider a tally on a surface with normal $\hat{n}$ where every particle that crosses in the positive direction is counted. For every particle, score the statistical weight by the m^{th} hemispherical harmonic h_m. In this case the tally mean is

$$\int_{\boldsymbol{H}} J(\hat{\Omega}) h_m(\hat{\Omega}) d\hat{\Omega} \tag{39}$$

where J is the planar fluence.

By applying the tally to the fluence equation and using the orthogonality relationship from equation 27, we can see that the tally gives us the m^{th} fluence expansion coefficient:

$$\begin{aligned}\int_{\boldsymbol{H}} J(\hat{\Omega}) h_m(\hat{\Omega}) d\hat{\Omega} &= \int_{\boldsymbol{H}} (\hat{n}\cdot\hat{\Omega})\phi(\hat{\Omega}) h_m(\hat{\Omega}) d\hat{\Omega} \\ &= \int_{\boldsymbol{H}} (\hat{n}\cdot\hat{\Omega}) \sum_n \hat{a}_n h_n(\hat{\Omega}) h_m(\hat{\Omega}) d\hat{\Omega} \\ &= \sum_n \hat{a}_n \int_{\boldsymbol{H}} (\hat{n}\cdot\hat{\Omega}) h_m(\hat{\Omega}) h_n(\hat{\Omega}) d\hat{\Omega} \\ &= \sum_n \hat{a}_n \delta_{mn} \\ &= \hat{a}_m.\end{aligned} \tag{40}$$

The fluence can then be converted to planar fluence by multiplying by $(\hat{n}\cdot\hat{\Omega})$. If a basis that utilizes Legendre polynomials was used then the tally would calculate planar fluence and would have to be converted to fluence by multiplying by $(\hat{n}\cdot\hat{\Omega})^{-1}$, but this introduces a singularity for grazing angles.

4.1.7 Sources of Error in the Expansion

There are two sources of error associated with the functional expansion tally method: statistical and truncation. Statistical errors occur because equation 37 is an estimate of the true expansion coefficient and therefore has some associated statistical uncertainty. The sample variance for an expansion coefficient $\hat{a}_n$ can be estimated by utilizing the customary method. This involves using equation 41 as an unbiased estimator for the true variance.

$$\hat{\sigma}^2_{\hat{a}_n} = \frac{\sum_{i=1}^{N}(w_i H_n(\hat{\Omega}))^2 - \frac{1}{N}\left(\sum_{i=1}^{N} w_i H_n(\hat{\Omega})\right)^2}{N(N-1)} \tag{41}$$

In equation 41, $H_n(\hat{\Omega})$ is a basis function, i is a single particle history, w_i is the statistical weight and N is the total number of particle histories. Equation 41 can be used to estimate the statistical uncertainty of an individual expansion coefficient. It is also possible to derive a result that gives the pointwise variance of the reconstructed functional estimate rather than individual coefficients but as Griesheimer et al. demonstrate, such an estimate is computationally intensive and can present an undue burden on the code [61].

A two-norm estimate of the variance has been previously derived and can be used to estimate the variance of the reconstructed functional estimate. Using the two-norm estimate of the variance provides a way to evaluate the overall statistical uncertainty rather than the individual expansion coefficients. Applying the orthogonality of the basis functions, it can be shown that

$$\int \hat{\sigma}^2_{\hat{\phi}(\hat{\Omega})}\, d\Omega = \sum_{n=0}^{M} \hat{\sigma}^2_{\hat{a}_n}, \tag{42}$$

where $\hat{\phi}$ represents the reconstructed functional approximation of the fluence, $\hat{\Omega}$ represents the angle, and $\hat{a}_n$ is the estimate of an individual expansion coefficient for the n^{th} basis function [61]. Equation 42 is used in this project to provide an estimate of the statistical error for each expansion performed.

The second source of error associated with the FET is truncation, which arises from the approximation of the true distribution with a truncated series expansion. Truncation error is not given by the magnitude of individual expansion coefficients, but rather is associated with the rate at which the sequence of coefficients converges toward zero. The 2-norm measure of the truncation error in a finite series expansion is given by equation 43 [67].

$$\|E_M\|^2 = \int \phi\left(\hat{\Omega}\right)^2 d\hat{\Omega} - \sum_{n=0}^{M} \bar{a}_n^2 \tag{43}$$

The Mth partial sum of the squared expansion coefficients will approach a constant value as the truncation error goes to zero. As is evident in equation 43, an approximation for the error requires knowledge of the true expansion coefficient, which is not available. The influence of truncation error will therefore be assessed when comparing the final results from COMET to the reference benchmark results produced in DOSXYZnrc. This approach is similar to that taken by other projects that implement the FET method [68].

Truncation error and statistical error are inversely related. If the expansion order is large the statistical uncertainty increases because the basis functions become more difficult to integrate. If the expansion order is small, the statistical uncertainty is lower but the truncation error increases. Large truncation error results in lower resolution. Care must be taken to achieve a balance when performing the FET method that produces results with acceptable truncation error and statistical uncertainty. Methods have been investigated to derive a cost-to-benefit metric that can be used to optimize the FET [61]. While interesting, this work does not focus entirely on the FET. Therefore

it was decided the best measure of results is in the final comparison with the Monte Carlo reference calculation. A more thorough investigation of the properties of the use of the FET in conjunction with linear accelerator phase space files is left for future work.

4.1.8 Source Spectrum

Accurate radiotherapy calculations depend greatly on implementing a method that includes a well modeled energy spectrum. Research into the energy spectrum produced from linear accelerators can be found as far back as 1955 [69]. This continues to be an active area of research, with investigational methods ranging from measurement to functional approximation [70-72].

The energy spectrum used in this work was taken from the BEAM user code for a 6 MV beam produced on a 2100C Varian clinic. It is shown in Figure 17. The shape of the 6 MV spectrum used is similar to that used in the source model for both the AAA and AXB algorithms. This is not unexpected as they were generated to match Varian C-series linear accelerators. The same spectrum is used for both the primary source and the secondary source. This approach has been adopted by other researchers with good results and for simplicity is also adopted in this work [73].

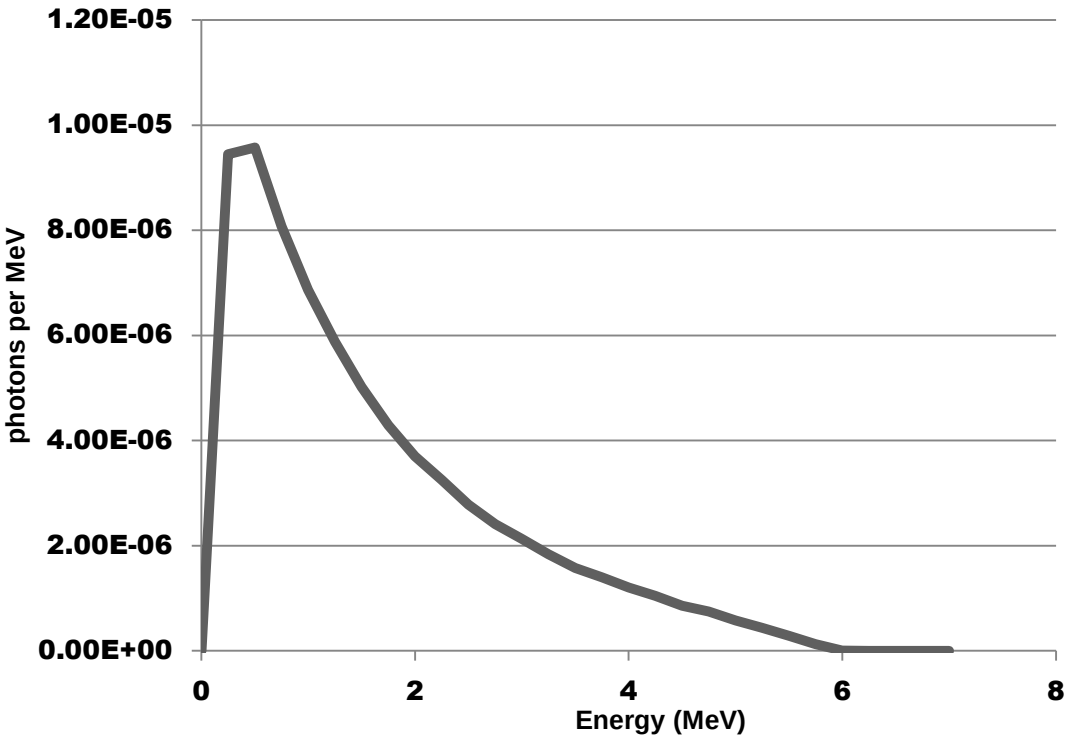

Figure 15: Photon spectrum for 6 MV photon beam from a 2100C linear particle accelerator

4.2 Extra-focal Photons

As previously mentioned, extra-focal photons are those generated or scattered in components other than the target. Liu et al., found that the extra-focal photon contribution to the photon fluence at isocenter was between 11% and 16 % [46].

The AAA and AXB algorithms model extra-focal fluence using a plane source located at the bottom of the flattening filter. The intensity distribution of the finite-size extra-focal source is Gaussian. The energy spectrum is scaled to obtain a given mean energy. The off-axis energy variation is not modeled. The weight of the extra-focal source compared to the primary source and the mean energy are free parameters that are adjusted to match calculated dose to measurement.

This project used the FET method and the reference phase space data to calculate the fluence generated by extra-focal photons in the same manner outlined in section 4.1. Adopting this approach allows the variation in intensity as a function of angle from the source to be well modeled.

Because the extra-focal photons are scattered or generated in components other than the target, the field size of extra-focal photons is larger than that projected by the collimator jaws at isocenter. The optimal field size for the secondary source in the work was determined empirically by comparing COMET calculated results with reference results.

4.3 Contamination Electrons

Sheikh-Bagheri and Rogers report that for a 6 MV Varian linear accelerator with a 10x10 cm^2 field at an SSD of 100 cm impinging on water, the dose from electron contamination accounts for 7.7% of the dose at the surface and 0.16% of the dose at the depth of maximum dose [50].

Although many approaches to modeling the electron contamination in a photon beam have been proposed, a relatively simple approach was chosen for this work [74, 75]. The broad beam depth dose behavior of the contaminant electrons has been shown to be almost exponential [76]. Therefore, the contaminant electrons were modeled with the exponential equation 44.

$$\frac{p_c}{\rho}(z) = \alpha e^{-\beta z} \tag{44}$$

In equation 43, p_c is the energy deposition due to contaminant electrons, ρ is the unit incident primary photon energy, z is the depth in centimeters, and α and β are free parameters [77]. The parameters α and β were found by manually fitting the percentage depth dose curve along the central axis calculated by COMET to the reference result calculated with the RPSD and the DOSXYZnrc user code. The parameters were set using calculations made in a water phantom.

This approach of using a fitted parameter to match the source model with a calculation or measurement is commonly used in source modeling. For example the AAA and AXB model, runs an extensive optimization to fit source model parameters such as mean radial energy of primary photons, intensity profile of primary photons, the weight of the extra-focal photon source with respect to the primary photon source, etc. to that measured clinically [78].

CHAPTER 6

TESTING THE FUNCTIONAL EXPANSION TALLY

5.1 FET and Phase Space Data

The approach of using the FET with phase space data to produce functional approximations of the photon fluence is a new concept in the source modeling of linear accelerators. To test the efficacy and to better quantify the behavior of this approach functional approximations of the planar fluence were generated with increasing expansion orders and compared with binned tally results generated from the same phase space file. The planar fluence was chosen to facilitate the comparison between the functional expansion and the binned tally. Expansions were also performed using increasing numbers of particle histories to investigate the impact of statistical error on the FET. The results were again compared to binned tally results computed from the same phase space file namely the 40x40 cm^2.

The functional value was calculated for a plane placed at 44.43 cm from a point source of radiation. This corresponds to the position of the plane on which the reference phase space data was tallied. The 40x40 cm^2 phase space file was read and the particles sorted into meshed bins to serve as the reference solution of the planar fluence. The square mesh size was set to 0.25 cm resolution. Particles histories were sorted using the LATCH parameter into primary, extra-focal, and electron. The functional value over the same mesh was obtained so that the relative difference between the FET and the Monte Carlo phase space fluence could be calculated. Both sets of data were normalized so that the central pixel has unit value so that results can

be compared when generated from differing numbers of particle histories. Comparisons were made with expansions performed using all basis functions and using only zonal harmonics.

The root-mean-square (RMS) difference was calculated for increasing expansion orders to investigate the effect of truncation error on the expansion and calculated with increasing particle histories to investigate the effect of statistical error. A similar approach has been used in other work with nuclear engineering applications [68]. The resulting comparisons were also separated according to typical field sizes used in radiotherapy applications. The field sizes are listed as nominal field size at isocenter. This approach serves to quantify the effect of truncation and statistical error for various field sizes and excludes error introduced at the square collimated field edges of the 40x40 cm^2 beam when using zonal harmonics.

5.2 FET and Binned Tally Comparison

The results of the comparisons of the planar fluence and the functional approximations of the planar fluence are shown in Tables 9 and 10.

The minimum RMS error for primary photon planar fluence was found with an expansion order of $l = 75$, 75,000 histories, and a zonal harmonic basis for all three field sizes. The lowest RMS error overall for primary photons was with the 10x10 cm^2 field size. The largest reductions in RMS error occurred as the expansion order increased. Increasing the number of particle histories used to generate the expansion coefficients had a much smaller, though apparent, impact on the RMS error. Increasing the number of histories did not necessarily reduce the RMS error with a fixed expansion order but

rather a minimum was reached and then the error began increasing with particles histories. The RMS error was systematically lower using the zonal harmonic basis.

The total number of extra-focal photons in the phase space file for the 40x40 cm^2 field size was 179,868. Consequently that is the highest number of particle histories used in the functional approximations. The minimum RMS error for the 5x5 cm^2 and the 10x10 cm^2 field sizes had an expansion order of $l = 50$. The minimum RMS error for the 20x20 cm^2 field size was found to be $l = 75$. For the 5x5 cm^2 field size the minimum RMS error was found at 25,000, 75,000, and 179,868 particle histories. For the 10x10 cm^2 field size the minimum RMS error was found at 75,000 particle histories and for the 20x20 cm^2 field size the minimum RMS error was found at 100,000 particle histories. The RMS error with the extra-focal photons was in general higher than the RMS error with primary photons with the minimum RMS error being 0.2302 in contrast to the primary photon minimum RMS error of 0.0158. The increase in expansion order did not have the same impact on the RMS error in extra-focal photons as it did with the primary photons. Again the RMS error was systematically lower using a zonal harmonic basis.

This brief investigation demonstrates that implementing the FET method with phase space data is capable of producing functional approximations that well represent the photon distributions from a linear accelerator. There is also strong evidence that indicates that using a zonal harmonic basis will produce a functional approximation that better agrees with measured data.

Table 9: Root-mean-square error of primary planar fluence for various field sizes, expansion orders, and number of particle histories. Results are presented for functional approximations with a full basis and zonal harmonic basis.

	Primary Photons Full Basis					Primary Photons Zonal Harmonic Basis				
5x5 cm^2										
# histories	***l*=15**	***l*=25**	***l*=35**	***l*=50**	***l*=75**	***l*=15**	***l*=25**	***l*=35**	***l*=50**	***l*=75**
25000	0.040	0.039	0.074	0.072	0.076	0.038	0.029	0.067	0.066	0.026
50000	0.038	0.034	0.074	0.057	0.042	0.038	0.032	0.069	0.055	0.037
75000	0.038	0.031	0.074	0.054	0.033	0.038	0.031	0.071	0.053	0.021
100000	0.038	0.030	0.076	0.061	0.054	0.038	0.029	0.075	0.059	0.040
200000	0.038	0.033	0.079	0.065	0.066	0.038	0.032	0.077	0.065	0.051
10x10 cm^2										
# histories	***l*=15**	***l*=25**	***l*=35**	***l*=50**	***l*=75**	***l*=15**	***l*=25**	***l*=35**	***l*=50**	***l*=75**
25000	0.077	0.116	0.154	0.113	0.105	0.076	0.104	0.139	0.098	0.047
50000	0.075	0.121	0.153	0.082	0.088	0.074	0.115	0.141	0.075	0.061
75000	0.075	0.115	0.157	0.075	0.049	0.075	0.110	0.147	0.070	0.016
100000	0.076	0.111	0.165	0.086	0.063	0.076	0.106	0.156	0.085	0.039
200000	0.075	0.118	0.170	0.096	0.071	0.077	0.113	0.162	0.097	0.055
20x20 cm^2										
# histories	***l*=15**	***l*=25**	***l*=35**	***l*=50**	***l*=75**	***l*=15**	***l*=25**	***l*=35**	***l*=50**	***l*=75**
25000	0.187	0.352	0.212	0.126	0.129	0.187	0.316	0.183	0.082	0.053
50000	0.180	0.385	0.203	0.090	0.118	0.182	0.346	0.183	0.055	0.075
75000	0.182	0.368	0.218	0.074	0.066	0.184	0.333	0.196	0.054	0.020
100000	0.185	0.356	0.232	0.089	0.069	0.187	0.321	0.213	0.077	0.044
200000	0.184	0.373	0.237	0.095	0.076	0.187	0.339	0.220	0.090	0.063

Table 10: Root-mean-square error of extra-focal planar fluence for various field sizes, expansion orders, and number of particle histories. Results are presented for functional approximations with a full basis and zonal harmonic basis.

	Extra-Focal Photons Full Basis					Extra-Focal Photons Zonal Harmonic Basis				
5x5 cm^2										
# histories	***l*=15**	***l*=25**	***l*=35**	***l*=50**	***l*=75**	***l*=15**	***l*=25**	***l*=35**	***l*=50**	***l*=75**
25000	0.238	0.241	0.260	0.242	0.275	0.237	0.236	0.241	0.231	0.252
50000	0.238	0.237	0.247	0.243	0.312	0.238	0.237	0.241	0.232	0.262
75000	0.238	0.236	0.242	0.238	0.272	0.238	0.236	0.238	0.231	0.249
100000	0.238	0.236	0.238	0.236	0.253	0.238	0.237	0.236	0.232	0.236
179868	0.238	0.236	0.238	0.233	0.246	0.238	0.236	0.236	0.231	0.233
10x10 cm^2										
# histories	***l*=15**	***l*=25**	***l*=35**	***l*=50**	***l*=75**	***l*=15**	***l*=25**	***l*=35**	***l*=50**	***l*=75**
25000	0.242	0.243	0.284	0.256	0.319	0.243	0.240	0.253	0.231	0.278
50000	0.246	0.243	0.264	0.253	0.303	0.246	0.244	0.254	0.232	0.271
75000	0.245	0.241	0.252	0.249	0.275	0.245	0.242	0.244	0.230	0.255
100000	0.247	0.244	0.248	0.251	0.255	0.246	0.242	0.240	0.233	0.239
179868	0.247	0.241	0.246	0.243	0.262	0.246	0.241	0.240	0.230	0.234
20x20 cm^2										
# histories	***l*=15**	***l*=25**	***l*=35**	***l*=50**	***l*=75**	***l*=15**	***l*=25**	***l*=35**	***l*=50**	***l*=75**
25000	0.272	0.295	0.322	0.315	0.340	0.267	0.280	0.291	0.254	0.266
50000	0.282	0.305	0.301	0.301	0.293	0.279	0.305	0.280	0.280	0.259
75000	0.280	0.296	0.279	0.279	0.284	0.276	0.296	0.279	0.258	0.255
100000	0.286	0.302	0.270	0.272	0.277	0.281	0.300	0.270	0.252	0.251
179868	0.288	0.293	0.262	0.264	0.284	0.281	0.295	0.268	0.256	0.265

CHAPTER 6

SOURCE EVALUATION

6.1 Water Phantom

The true test of the proposed source model is in the final dose calculation performed when coupled with the COMET code. A logical starting point for such calculations is with a water phantom.

A water phantom of 30x30x30 cm^3 was developed in COMET, the Eclipse treatment planning system, and in the DOSXYZnrc user code. The water phantom was placed at a nominal source-to-surface distance of 100 cm and calculations were performed with a 4x4, 10x10, and 20x20 cm^2 field sizes.

The Eclipse calculations were performed with a 0.25 cm grid spacing for both AAA and AXB calculations. Beam data used in source modeling was from the Varian gold beam data set for 6 MV photons. Eclipse version 11.0 was used along with AAA version 11.0 and AXB version 11.0. All Eclipse calculations were performed on a Dell Optiplex 755 computer (Dell Inc., Round Rock, TX) with an Intel Core 2 Duo CPU at 2.33GHz and 8.00 GB of RAM.

COMET calculations were also performed with 0.25 cm grid spacing. Response functions were pre-calculated according to the method outlined in Hayward's doctoral dissertation and the parameters reported in Appendix A [45]. The notation for expressing the expansion orders of the response functions used in each calculation was adopted from Hayward's work and is as follows:

$$(o_1 o_2 o_3 o_4 o_5 o_6)$$

where

o_1= angular expansion order for uncollided fluence

o_2= spatial expansion order for uncollided fluence

o_3= angular expansion order for photon fluence

o_4= spatial expansion order for photon fluence

o_5= angular expansion order for electron fluence

o_6= spatial expansion order for electron fluence

The example presented by Hayward is for order=(917062). This denotes and expansion of 9th order in uncollided angle, 1st order in uncollided space, 7th order in photon angle, 0th order in photon space, 6th order in electron angle, and 2nd order in electron space.

All response functions were calculated with the hemispherical harmonic orders set to 7 and the Legendre orders set to 2. That limits the maximum order that can be chosen in further COMET calculations with this set of response functions. The maximum angular expansion that can be chosen is 7 and the maximum spatial expansion that can be chosen is 2. COMET calculations were performed in the water phantom for comparison to the DOSXYZnrc calculated reference data and the AAA and AXB results.

The DOSXYZnrc user code was used to generate reference results to test the accuracy of the proposed source model when coupled with the COMET code. The research in this work, such as the fluence shape, was performed using the phase space files provided by Cho et al. [65]. All DOSXYZnrc calculations were run on a cluster with

4 compute nodes, each with 31 GB of memory and 12 six-core AMD Opteron 2427s clocked at 2.2 GHz.

The 4x4 cm^2 reference solution followed 1 x 10^{10} source particle histories and took 21.347 hours to calculate on a 10 processors. The average percentage error of the 20 highest doses was 0.091% and the quadrature average percentage of the doses greater than half of the maximum dose was 0.010%.

The 10x10 cm^2 reference solution followed 1 x 10^{11} source particle histories and took 101.283 hours to calculate on a 30 processors. The average percentage error of the 20 highest doses was 0.105% and the quadrature average percentage of the doses greater than half of the maximum dose was 0.125%.

The 20x20 cm^2 reference solution followed 1 x 10^{11} source particle histories and took 101.330 hours to calculate on 30 processors. The average percentage error of the 20 highest doses was 0.208% and the quadrature average percentage of the doses greater than half of the maximum dose was 0.244%.

6.2 Slab Phantom

Rogers and Mohan developed a benchmark for testing Monte Carlo methods with strong heterogeneities [79]. The phantom consists of 4 layers of water, aluminum, lung and water respectively. To adapt the benchmark to better match the characteristics of a typical patient, the aluminum layer was replaced with a slab of bone and water was replaced with soft tissue. This is the approach taken by Han et al. when evaluating AXB calculations in heterogeneous media described in section 2.3.5 [49].

Matlab was used to create a series of axial DICOM-CT images that were used by DOSXYZnrc, Eclipse, and COMET when performing calculations. The phantom was created to have dimensions of 30x30x30 cm^2 and is composed of 4 layers of varying

thicknesses. The layers, listed in order from proximal to the source to the most distal are: 3 cm of soft tissue (1.0 g/cm^3), 2 cm of bone (1.85 g/cm^3), 7 cm of lung tissue (0.26 g/cm^3), and 18 cm of soft tissue (1.0 g/cm^3). Figure 16 shows the phantom imported in the Eclipse treatment planning system.

DOSXYZnrc, COMET, and Eclipse have differing methods of using DICOM-CT images to create data sets containing the density and material composition necessary for dose calculation. DOSXYZnrc uses a program called CTCREATE to import the necessary data [40]. CTCREATE uses a set of conversion ramps to convert CT numbers stored in the DICOM-CT images to map each voxel to density and material composition. A total of 4 materials are specified for import in CTCREATE. The ramp used for importing the slab phantom DICOM-CT images is shown in Figure 17 [80]. The process is described in more detail in the DOSXYZnrc User's Manual [40].

COMET performs a conversion in a similar way to CTCREATE. The density is mapped to a set of discrete values and the CT to material conversion is accomplished using the values in Table 11. The process is described in detail by Hayward in his dissertation [45].

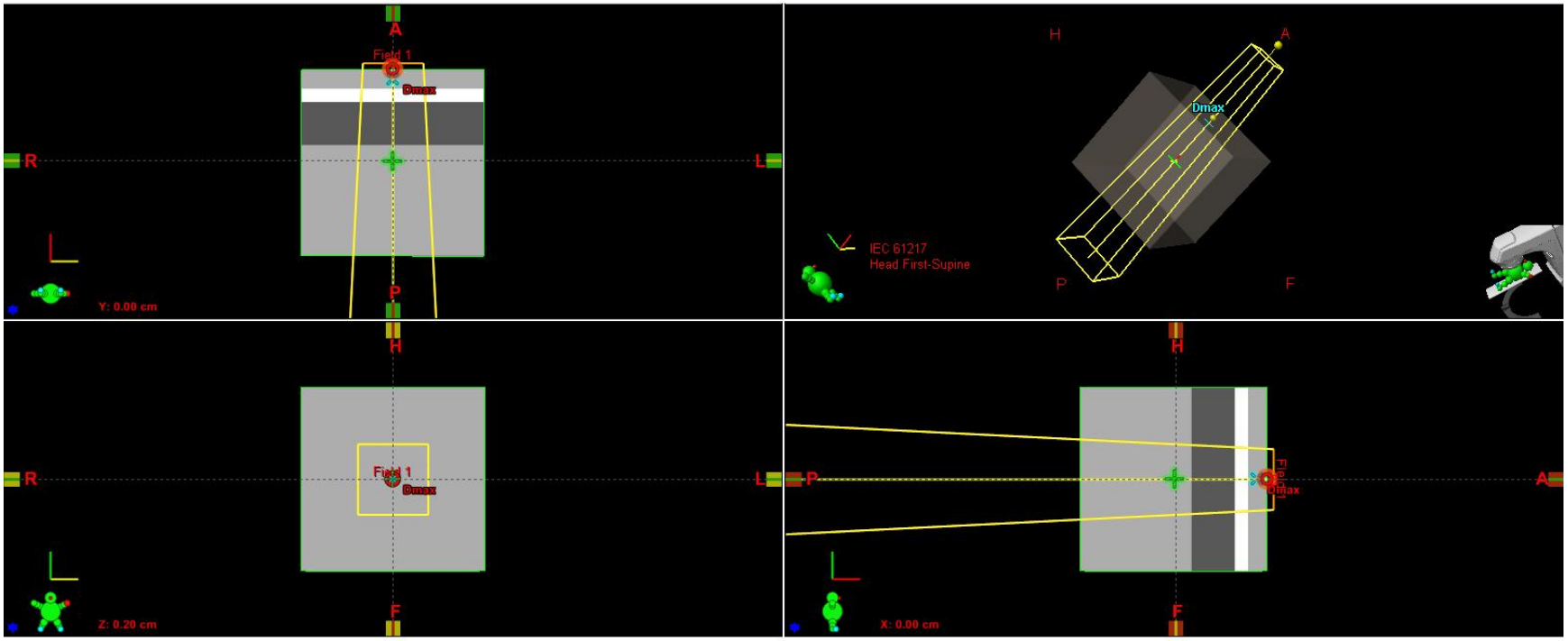

Figure 16: Slab phantom in Eclipse. Dicom-CT images were generated with Matlab and imported.

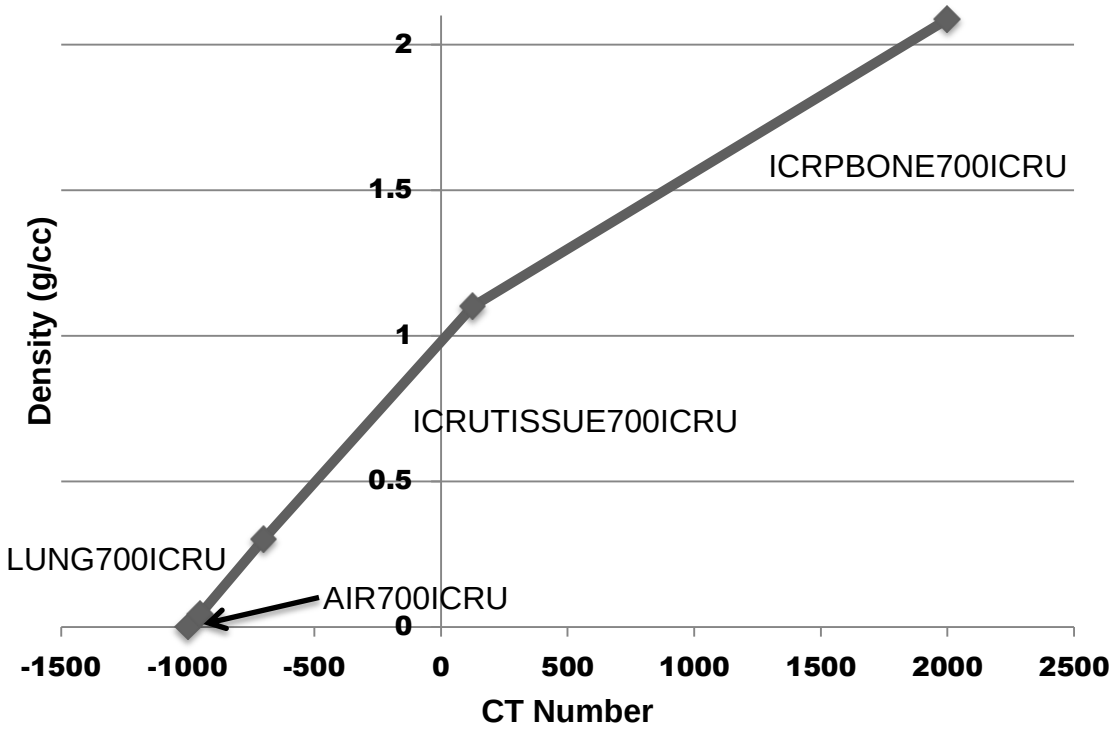

Figure 17: The ramp for converting CT values to material and density used with CTCREATE

Table 11: CT to material conversion

Range of Hounsfield Units	Material	Density (g/cm^3)
-1000 ≤ HU ≤ -950	Air	1.2048 x 10^{-3}
-950 ≤ HU ≤ -700	Lung	0.26
-700 ≤ HU ≤ 125	Soft Tissue	1.0
125 ≤ HU ≤ 2000	Bone	1.85

Like DOSXYZnrc, Eclipse uses a series of conversion ramps to convert CT number to material assignment and density. The conversion ramps used in this research project are shown in Figure 18, which is taken directly from the Eclipse treatment planning system. The HU values in each slab were checked in Eclipse to ensure that the phantom was imported and reconstructed with the correct material specification and density.

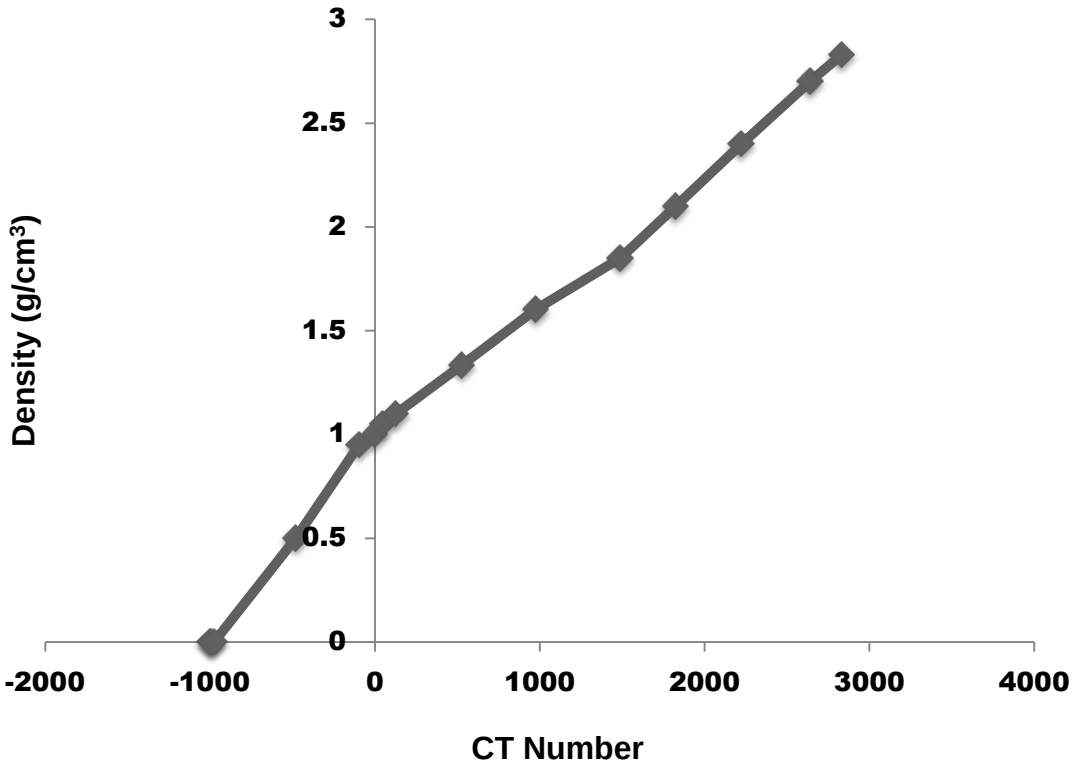

Figure 18: Graph of CT number and material assignment versus density used by Eclipse for the AXB algorithm

The choice to use a phantom that was digitally produced and imported rather than creating the phantom within each software package was made in an attempt to ensure consistency between dose calculation methodologies being tested.

DOSXYZnrc calculations were performed to generate a set of reference solutions for use in comparing the performance of all calculation methods being tests. Efforts were made to keep the relative uncertainty low by following a large number of source particle histories.

The 4x4 cm^2 reference solution followed 1 x 10^{10} source particle histories and took 21.078 hours to calculate on 10 processors. The average percentage error of the 20 highest doses was 0.135% and the quadrature average percentage of the doses greater than half of the maximum dose was 0.185%.

The 10x10 cm^2 reference solution followed 1 x 10^{11} source particle histories and took 105.557 hours to calculate on a 30 processors. The average percentage error of the 20 highest doses was 0.470% and the quadrature average percentage of the doses greater than half of the maximum dose was 0.626%.

The 20x20 cm^2 reference solution followed 5 x 10^{11} source particle histories and took 101.522 hours to calculate on 30 processors. The average percentage error of the 20 highest doses was 0.202% and the quadrature average percentage of the doses greater than half of the maximum dose was 0.272%.

COMET calculations were performed with the slab phantom for the purpose of testing the influence of the expansion order. To that end, sample runs were made with orders (727272), (717171), (525252), (515151), (323232), and (313131) and the results were compared to the Monte Carlo generated reference solutions. The calculations were performed with a 10x10 cm^2 field size and the phantom size was reduced to 15x15x30 cm^2 to reduce the computation time. All COMET calculations were done on a cluster with 4 compute nodes, each with 31 GB of memory and 12 six-core AMD Opteron 2427s clocked at 2.2 GHz.

6.3 Sample Lung Patient CT Phantom

Figure 19 shows the axial, sagittal, and coronal views of a lung patient used to create the lung phantom for dose calculation comparisons. A lung patient was chosen with a mediastinal tumor because the highly inhomogeneous nature of the lung region will best reveal the capabilities of each calculation method. The tumor is clearly visible on the axial slice close to the mediastinum and the isocenter is placed inside the tumor.

The DICOM image data was first truncated to a smaller size to facilitate faster calculation times for COMET. This was necessary because the current version of COMET calculates dose for the entire image set being used even in areas far outside of the field. The voxel size was set to 0.25x0.25x0.25 cm^3 and each voxel was mapped to four materials and densities according to the methods outlined in section 6.2. The phantom was slightly modified for the use of each calculation method to ensure that the correct material and density was assigned during import. Figure 20 shows the truncated DICOM patient images with the resampled voxels size and density.

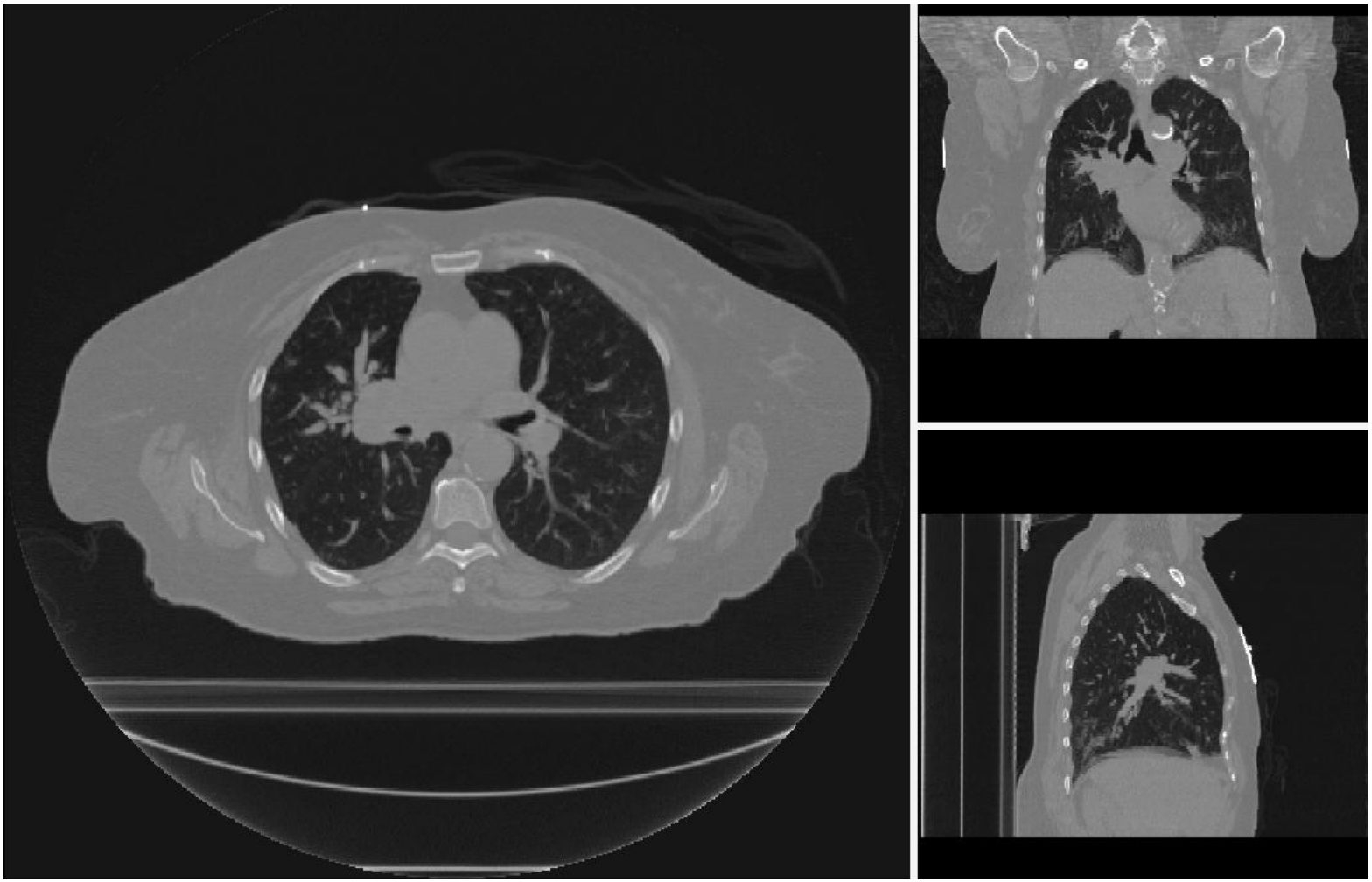

Figure 19: Patient DICOM images used to create the lung phantom. Note the mediastinal tumor in the right lung.

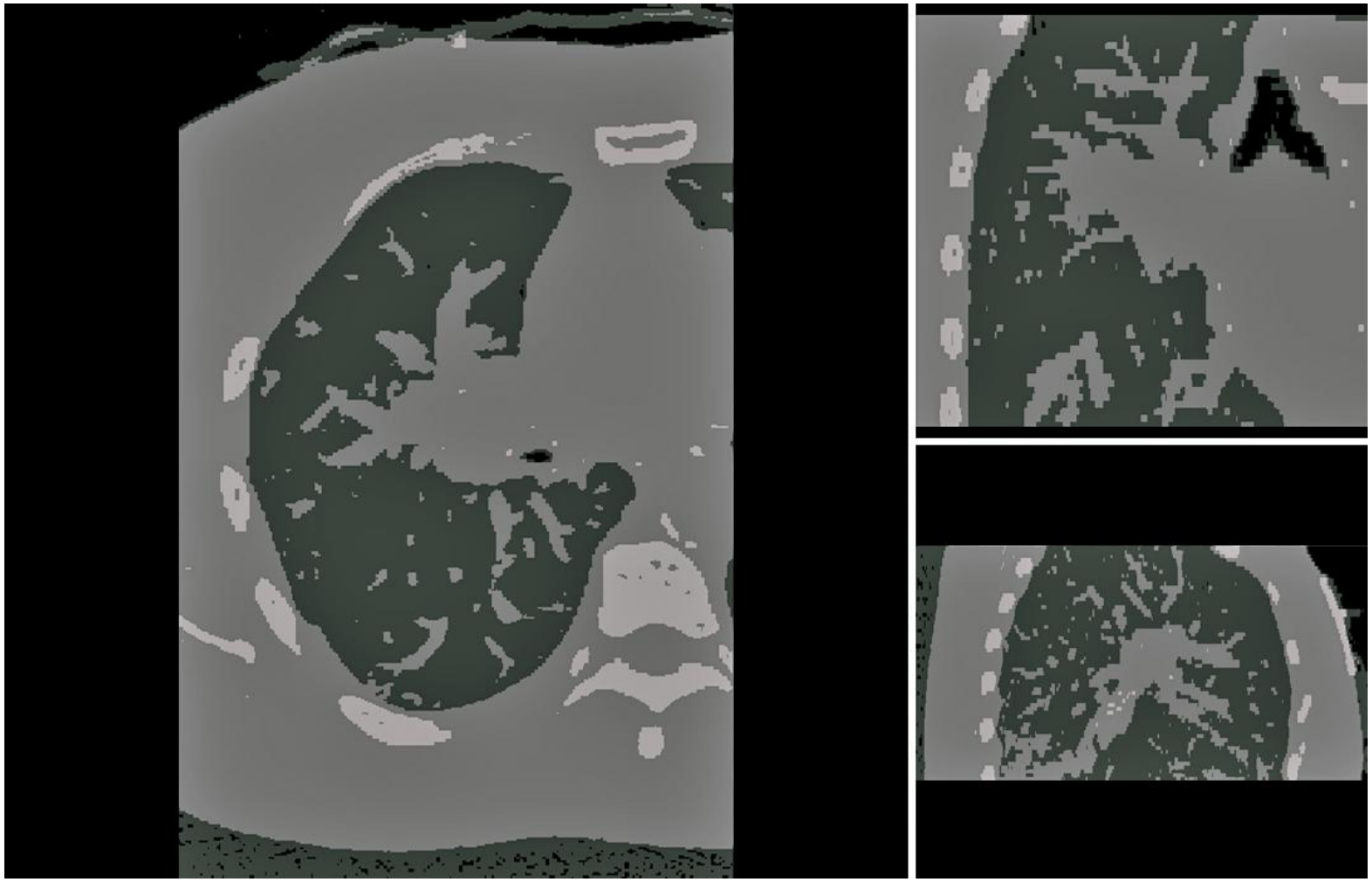

Figure 20: The truncated lung phantom mapped to 4 materials and densities

6.4 Tests for Inter-comparison

To evaluate the results of the dosimetric calculations performed with DOSXYZnrc, COMET, AAA, and AXB a series of tests were used. First all results needed to be normalized in a consistent manner. A commonly used method of normalizing to the dose maximum along the central axis was chosen. This method was applied to the homogeneous water phantom and the inhomogeneous slab phantom. This approach presents the percentage depth dose data in a format that is customary in medical physics. For the lung phantom calculations all results were normalized to the global dose maximum.

It is common when evaluating the accuracy of dose calculations to examine the central axis percentage depth dose curves and profiles at various depths. That method was adopted for both the homogeneous water phantom and the inhomogeneous slab phantom. Profiles are reported for depths of 1.5, 10, and 20 cm. The dose difference was calculated as a percentage relative to the DOSXYZnrc dose. Results are graphed and maximum and root-mean-square error is reported.

Two dimensional comparisons were also performed based on the work of Low, et al. in a technique known as the gamma method [81]. When comparing two dose distributions a simple dose difference or isodose comparison may not be appropriate. Comparisons of two dose distributions are vulnerable to misjudgment in the following cases [82]:

- The difference between two dose-distributions can be large in high-gradient regions, even if the isodoses are relatively close to each other.
- The isodose distance between two dose distributions can be large in regions with a flat dose distribution, although the difference in dose may be quite small.

The gamma method can accommodate both scenarios. The gamma value for the measurement point r_m is shown in equation 45:

$$\gamma(r_m) = \min\{\Gamma(r_m, r_c)\} \forall \{r_c\} \tag{45}$$

where

$$\Gamma(r_m, r_c) = \sqrt{\frac{r^2(r_m, r_c)}{\Delta d_M^2} + \frac{\delta^2(r_m, r_c)}{\Delta D_M^2}} \tag{46}$$

$$r(r_m, r_c) = |r_c - r_m| \tag{47}$$

and

$$\delta(r_m, r_c) = D_c(r_c) - D_m(r_m) \tag{48}$$

where r_m is the position of a single measurement point, r_c is the spatial location of the calculated distribution relative to the measurement point, Δd_M is the passing criteria for isodose distance, ΔD_M is the passing criteria for dose, $D_c(r_c)$ is the calculated dose in r_c, and $D_m(r_m)$ is the measured dose in r_m. The pass and fail criteria are shown in equations 49 and 50.

$$\gamma(r_m) \leq 1 \text{ calculation passes} \tag{49}$$

$$\gamma(r_m) \geq 1 \text{ calculation fails} \quad (50)$$

To implement the gamma method two criteria for a passing result must be chosen: the dose difference and the distance to agreement (DTA). DTA is defined as the distance between a dose point in the calculated distribution and the nearest point in the measured distribution containing the same dose value. For example a commonly used criteria IMRT quality assurance testing is 2% dose difference and 2 mm DTA with a 90% passing rate considered acceptable.

All gamma comparisons were performed with the OmniPro I'mRT software version 1.7.0021 by IBA Dosimetry (IBA Dosimetry GmbH, Schwarzenbruck, Germany). The criterion chosen for comparison of the water and slab phantoms was 1% dose difference and 1mm DTA. Such a tight tolerance was chosen to uncover deviations from the reference solution that are even smaller than that which is generally clinically acceptable. A more clinically applicable criterion of 2% dose difference and 2% DTA was used when performing gamma tests on the lung phantom.

CHAPTER 7

RESULTS

7.1 Primary Source

7.1.1 Expansion Coefficients

Estimates for the statistical error of the expansions using the FET method are shown in Tables 12 and 13 for both a full expansion and an expansion using only the zonal harmonics respectively. Some trends that can be seen in the data include the increase in variance of the overall expansion with increase in expansion order for the same number of particles and the decrease in variance with increased particle histories. One trend that is particularly important for this study is the decrease in variance for the same field size and number of particles when zonal harmonics are used when compared to the same expansion using a full expansion basis.

Table 12: Full expansion with primary photons

Field Size (cm^2)	Number of Histories	Expansion Order *l*	2-norm Variance	Average Coefficient Value
4x4	1000	10	3.62E-05	4.75E-03
	10000	10	3.38E-06	4.62E-03
	100000	10	3.31E-07	4.60E-03
	1000	25	2.17E-04	2.78E-03
	10000	25	2.02E-05	2.75E-03
	100000	25	1.99E-06	2.71E-03
	1000	35	4.40E-04	2.24E-03
	10000	35	4.11E-05	2.21E-03
	100000	35	4.05E-06	2.18E-03
10x10	1000	10	1.94E-05	3.33E-03
	10000	10	2.06E-06	3.40E-03
	100000	10	2.08E-07	3.41E-03
	1000	25	1.37E-04	1.72E-03
	10000	25	1.45E-05	1.68E-03
	100000	25	1.47E-06	1.68E-03
	1000	35	2.97E-04	1.15E-03
	10000	35	3.11E-05	1.11E-03
	100000	35	3.15E-06	1.12E-03
20x20	1000	10	1.80E-05	2.38E-03
	10000	10	1.84E-06	2.48E-03
	100000	10	1.66E-07	2.42E-03
	1000	25	1.28E-04	6.77E-04
	10000	25	1.32E-05	6.49E-04
	100000	25	1.20E-06	6.31E-04
	1000	35	2.54E-04	2.91E-04
	10000	35	2.60E-05	2.33E-04
	100000	35	2.38E-06	2.24E-04

Table 13: Zonal harmonics with primary photons

Field Size (cm^2)	Number of Histories	Expansion Order *l*	2-norm Variance	Average Coefficient Value
4x4	1000	10	2.52E-05	4.72E-03
	10000	10	2.40E-06	4.63E-03
	100000	10	2.36E-07	4.61E-03
	1000	25	1.22E-04	2.78E-03
	10000	25	1.14E-05	2.73E-03
	100000	25	1.12E-06	2.71E-03
	1000	35	2.11E-04	2.24E-03
	10000	35	2.00E-05	2.19E-03
	100000	35	1.97E-06	2.18E-03
10x10	1000	10	1.19E-05	3.38E-03
	10000	10	1.25E-06	3.39E-03
	100000	10	1.29E-07	3.42E-03
	1000	25	4.43E-05	1.69E-03
	10000	25	4.54E-06	1.68E-03
	100000	25	4.70E-07	1.70E-03
	1000	35	6.87E-05	1.13E-03
	10000	35	7.07E-06	1.12E-03
	100000	35	7.20E-07	1.13E-03
20x20	1000	10	7.77E-06	2.47E-03
	10000	10	7.44E-07	2.50E-03
	100000	10	6.47E-08	2.44E-03
	1000	25	2.31E-05	7.10E-04
	10000	25	2.31E-06	6.89E-04
	100000	25	2.09E-07	6.80E-04
	1000	35	3.61E-05	3.13E-04
	10000	35	3.68E-06	2.90E-04
	100000	35	3.65E-07	2.88E-04

7.1.2 Source Shape

In a plot of the primary photon fluence it is expected that the effect of the flattening filter be evident. Figures 21 and 22 show the plots of the primary source for increasing expansion orders generated from the 40x40 cm^2 reference phase space file using a purpose built Matlab function. Note that the scale is adjusted to better illustrate the fluence shape. The normalization is that described in section 4.1.6. For the purpose of visual inspection and comparison to previously published data, no energy discretization was used. All plots generated in this section are based on expansions and reconstructions of 100,000 particles. The fluence emanates from a single point and the value of the functional approximation is based on the expansion and reconstruction using hemispherical harmonics with adjoint Jacobi basis functions. The influence of the flattening filter and the rectilinear collimation are evident by an expansion order of $l = 15$ and clearly visible by $l = 25$. By $l = 75$ the expansion is no longer smooth for 100,000 particle histories.

For the expansion order $l = 75$, the number of coefficients necessary, given by the equation $(l + 1)^2$, is 5,776. Taking into consideration the total number of energy groups, to perform such an expansion for the primary source and 14 energy groups requires a total of 80,864 expansion coefficients. Of note is the large disc shape in the reconstruction at angles where θ approaches 90°. This is a consequence of performing the hemispherical harmonic expansion with the basis that was previously described. Attempts to correct for this phenomenon destroy the integral value of the expansion and so it was not accounted for in this work. The radiation emanating from the head of linear accelerator from such large polar angles does not reach the patient and therefore does not influence the final dose calculations.

A large number of expansion coefficients takes away some of the advantage of using an orthogonal expansion technique, namely the computational simplicity. For example the integration of a product of any two arbitrary piecewise continuous functions using this technique is simplified to a series of dot product computations of the expansion coefficients. This is a prime format for parallel computation, thus further reducing calculation times. When the total number of expansion coefficients increases to such large numbers, it is clear that the computational burden can quickly become unacceptable. It is desirable to reduce the total number of expansion coefficients to a manageable size, while retaining the primary photon source properties necessary for accurate dose calculation. Since the primary source has small or no azimuthal dependence, it is reasonable to drop the expansion coefficients with $m \neq 0$, and retain only the zonal harmonics [46]. Figures 23 and 24 show the zonal harmonic expansion using increasing orders. The influence of the flattening filter is quickly apparent, even in the lower order expansions.

The primary fluence is only one factor in the complex transport processes involved in radiotherapy dose deposition. To ensure that an expansion order is adopted that produces optimal end results further testing is required, but the estimates for the statistical error in Tables 12 and 13 and the reconstructions in Figures 21, 22, 23, and 24 strongly indicate that zonal harmonics be adopted.

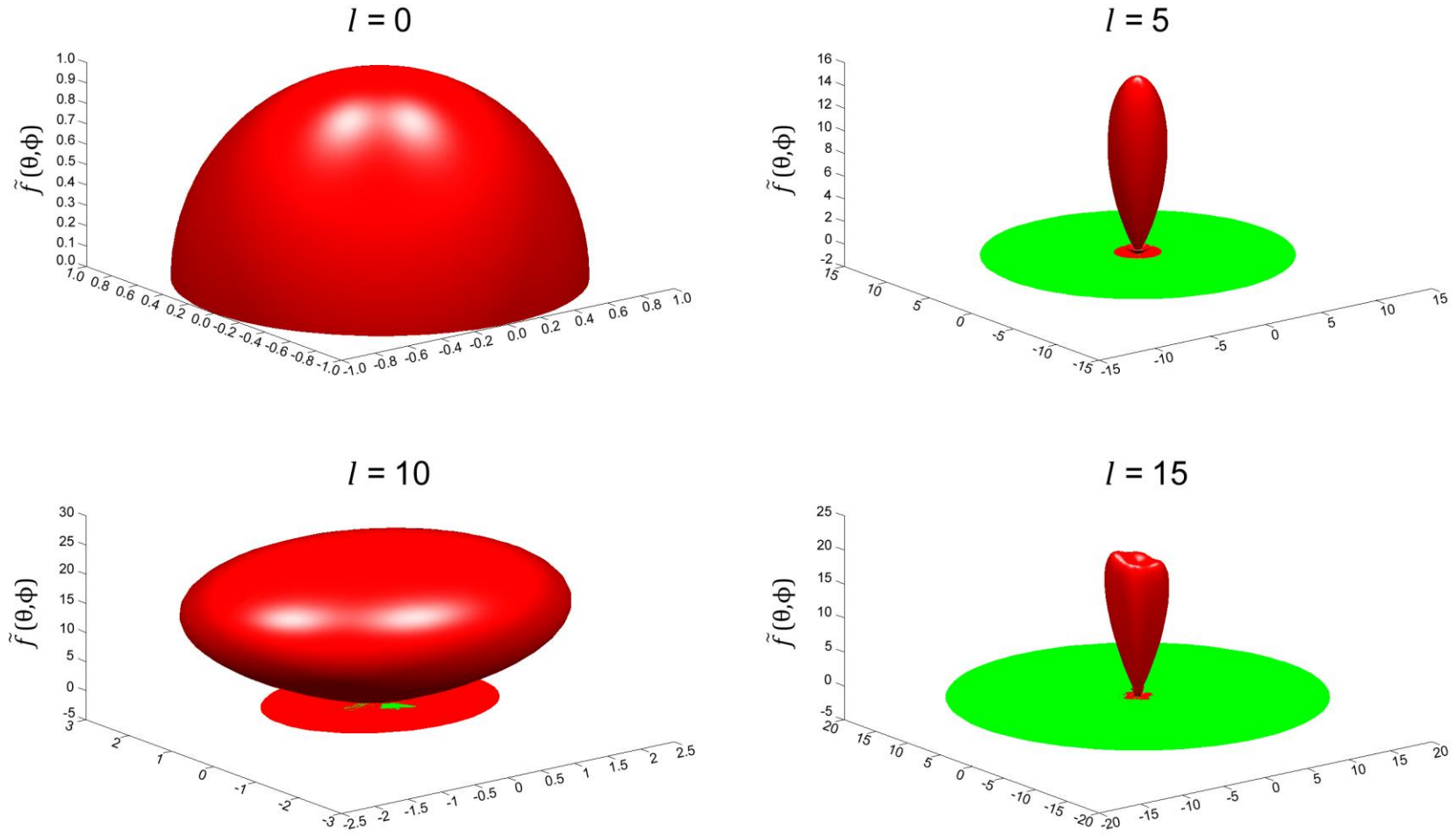

Figure 21: Reconstruction of the approximate function describing the primary fluence derived from phase space files. Expansion orders *l* = 0, 5, 10, 15.

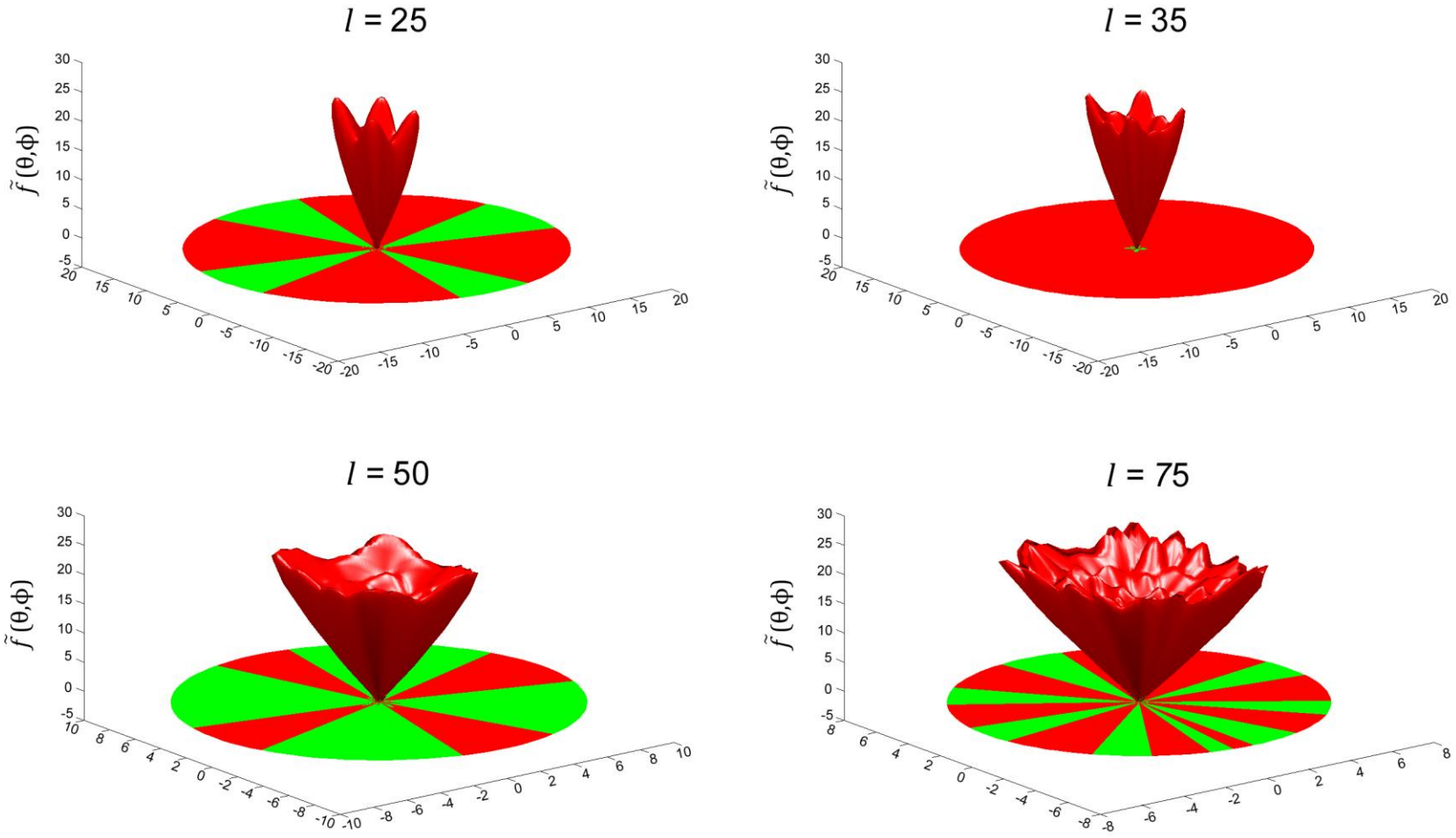

Figure 22: Reconstruction of the approximate function describing the primary fluence derived from phase space files. Expansion orders *l* = 25, 35, 50, 75.

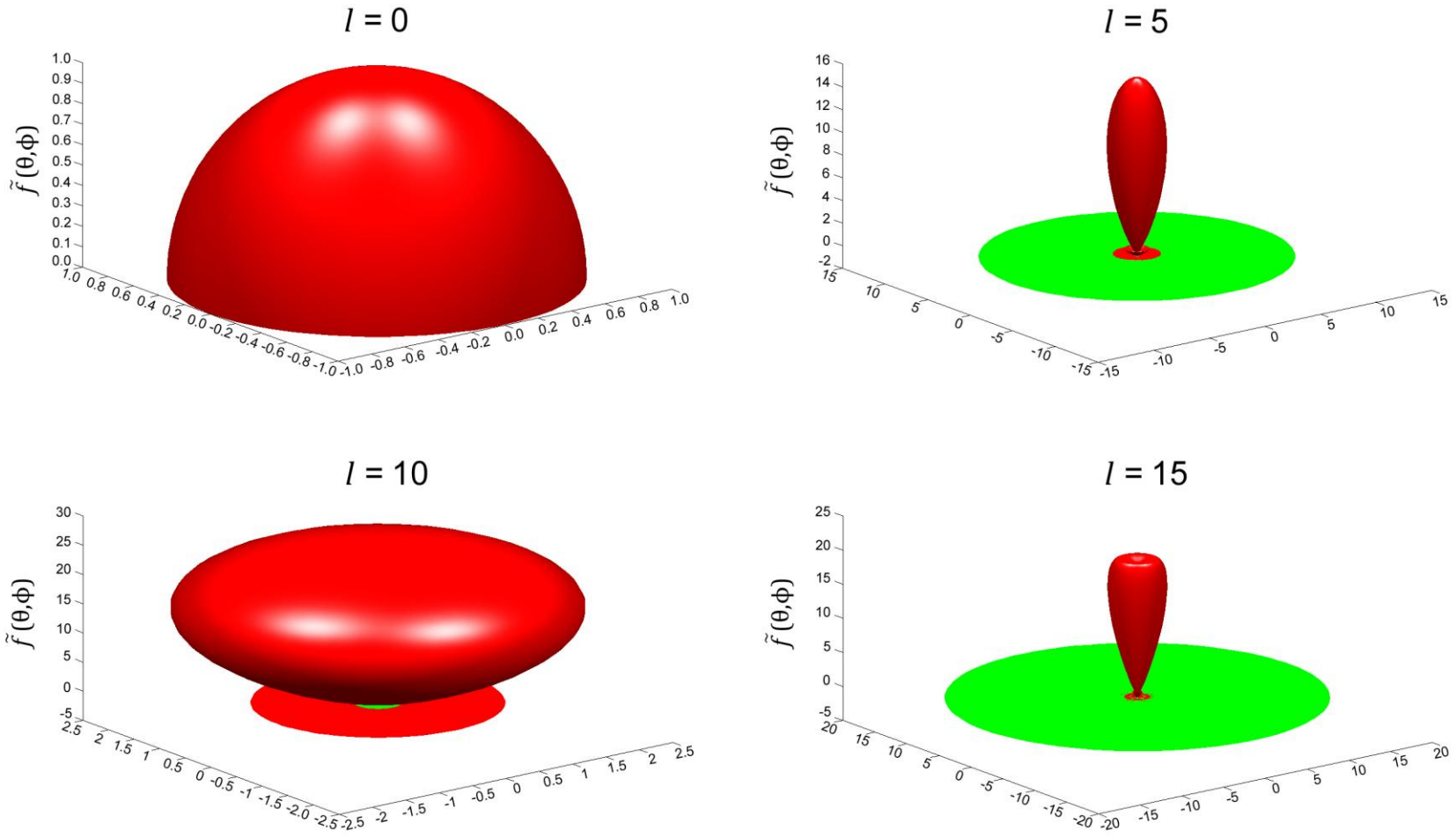

Figure 23: Reconstruction of the approximate function describing the primary fluence derived from phase space files using zonal harmonics. Expansion orders *l* = 0, 5, 10, 15.

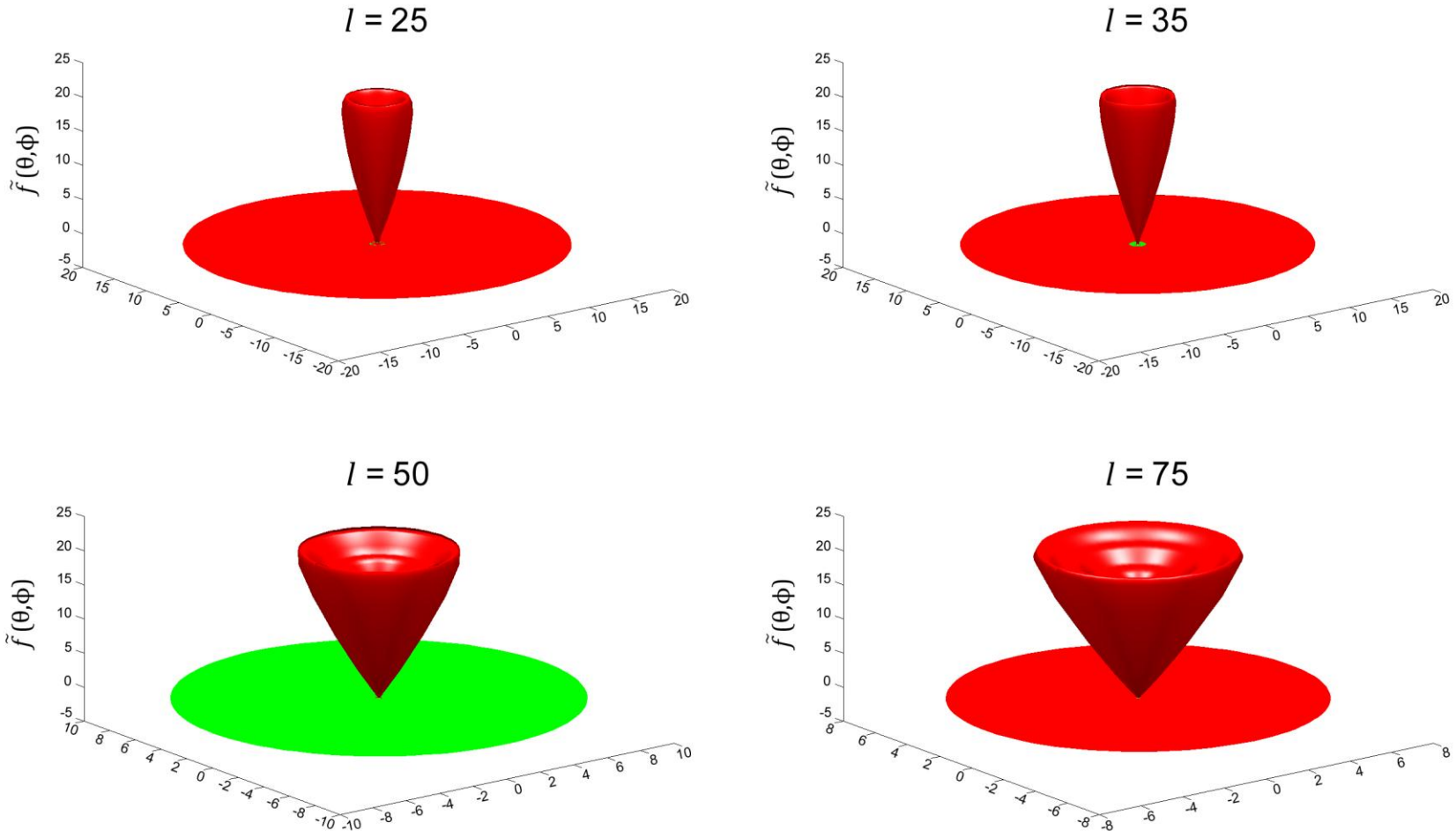

Figure 24: Reconstruction of the approximate function describing the primary fluence derived from phase space files using zonal harmonics. Expansion orders *l* = 25, 35, 50, 75.

7.2 Extra-Focal Source

7.2.1 Expansion Coefficients

Tables 14 and 15 display estimates of the 2-norm variance for expansions of the extra-focal photons. Similar trends to the primary source expansion variance are seen here. The statistical uncertainty of the overall expansion decreases with the increase in the number of particle histories. The statistical uncertainty of the overall expansion increases with expansion order for the same number of particles. The trend that is particularly important for this study is the decrease in statistical uncertainty for the same field size and number of particles when zonal harmonics are used when compared to the same expansion using a full expansion basis.

Table 14: Variance estimates for full expansion with extra-focal photons

Field Size (cm^2)	Number of Histories	Expansion Order *l*	2-norm Variance	Average Coefficient Value
4x4	1000	10	1.68E-04	9.23E-04
	10000	10	1.46E-05	1.00E-03
	100000	10	1.45E-06	1.06E-03
	1000	25	9.27E-04	2.93E-04
	10000	25	8.06E-05	3.62E-04
	100000	25	8.00E-06	3.90E-04
	1000	35	1.77E-03	1.80E-04
	10000	35	1.54E-04	2.52E-04
	100000	35	1.53E-05	2.69E-04
10x10	1000	10	8.59E-05	8.50E-04
	10000	10	8.38E-06	8.03E-04
	100000	10	8.26E-07	7.76E-04
	1000	25	4.70E-04	2.84E-04
	10000	25	4.59E-05	2.89E-04
	100000	25	4.53E-06	2.77E-04
	1000	35	8.98E-04	1.65E-04
	10000	35	8.75E-05	1.79E-04
	100000	35	8.65E-06	1.67E-04
20x20	1000	10	5.69E-05	8.41E-04
	10000	10	5.90E-06	6.46E-04
	100000	10	6.08E-07	6.39E-04
	1000	25	3.11E-04	1.88E-04
	10000	25	3.23E-05	1.69E-04
	100000	25	3.33E-06	1.43E-04
	1000	35	5.93E-04	7.25E-05
	10000	35	6.16E-05	8.07E-05
	100000	35	6.35E-06	6.49E-05

Table 15: Variance estimates for zonal harmonics with extra-focal photons

Field Size (cm^2)	Number of Histories	Expansion Order *l*	2-norm Variance	Average Coefficient Value
4x4	1000	10	2.89E-05	1.08E-03
	10000	10	2.77E-06	1.12E-03
	100000	10	2.84E-07	1.16E-03
	1000	25	9.47E-05	4.01E-04
	10000	25	9.07E-06	4.08E-04
	100000	25	9.34E-07	4.24E-04
	1000	35	1.42E-04	2.71E-04
	10000	35	1.34E-05	2.76E-04
	100000	35	1.39E-06	2.87E-04
10x10	1000	10	2.04E-05	9.02E-04
	10000	10	1.86E-06	8.18E-04
	100000	10	1.89E-07	8.30E-04
	1000	25	6.30E-05	3.38E-04
	10000	25	5.41E-06	2.84E-04
	100000	25	5.54E-07	2.95E-04
	1000	35	8.74E-05	2.09E-04
	10000	35	7.51E-06	1.71E-04
	100000	35	7.77E-07	1.78E-04
20x20	1000	10	1.29E-05	7.59E-04
	10000	10	1.29E-06	7.03E-04
	100000	10	1.28E-07	6.85E-04
	1000	25	2.71E-05	1.44E-04
	10000	25	2.97E-06	1.54E-04
	100000	25	3.05E-07	1.56E-04
	1000	35	3.78E-05	5.28E-05
	10000	35	4.19E-06	6.70E-05
	100000	35	4.27E-07	7.26E-05

7.2.2 Source Shape

Figures 25 and 26 display the reconstructed functional approximation of the extra-focal photon fluence based on a full hemispherical harmonic expansion. Figures 27 and 28 represent the reconstructed functional approximation of the extra-focal photon fluence using only the zonal harmonics. All plots were generated using the RPSD with 40x40 cm^2 field size. As with the primary photon source no energy discretization was used to generate these plots. All plots generated in this section are based on expansions and reconstructions of 100,000 particles. The scale of the plots was adjusted to best illustrate the shape of the plots.

While no published image could be found for the shape of the secondary source to use as a reference, these plots are instructive. The full expansion begins displaying the effect of the flattening filter and the rectilinear collimation by expansion order $l = 15$. This is not surprising as most of the extra-focal photons are generated in either the primary collimator or the flattening filter and thus travel through both the flattening filter and the collimator jaws on their way out of the head of the machine. There is more fluence at large polar angles than with the primary source as expected because all photons in the extra-focal source have undergone at least one scattering event.

As with the primary source, the evidence from the variance analysis and the plots of the source shape strongly favor using zonal harmonics rather than a full hemispherical harmonic expansion. Adopting this approach has the added advantage of reducing the computational time necessary to calculate the fluence at each point within the phantom.

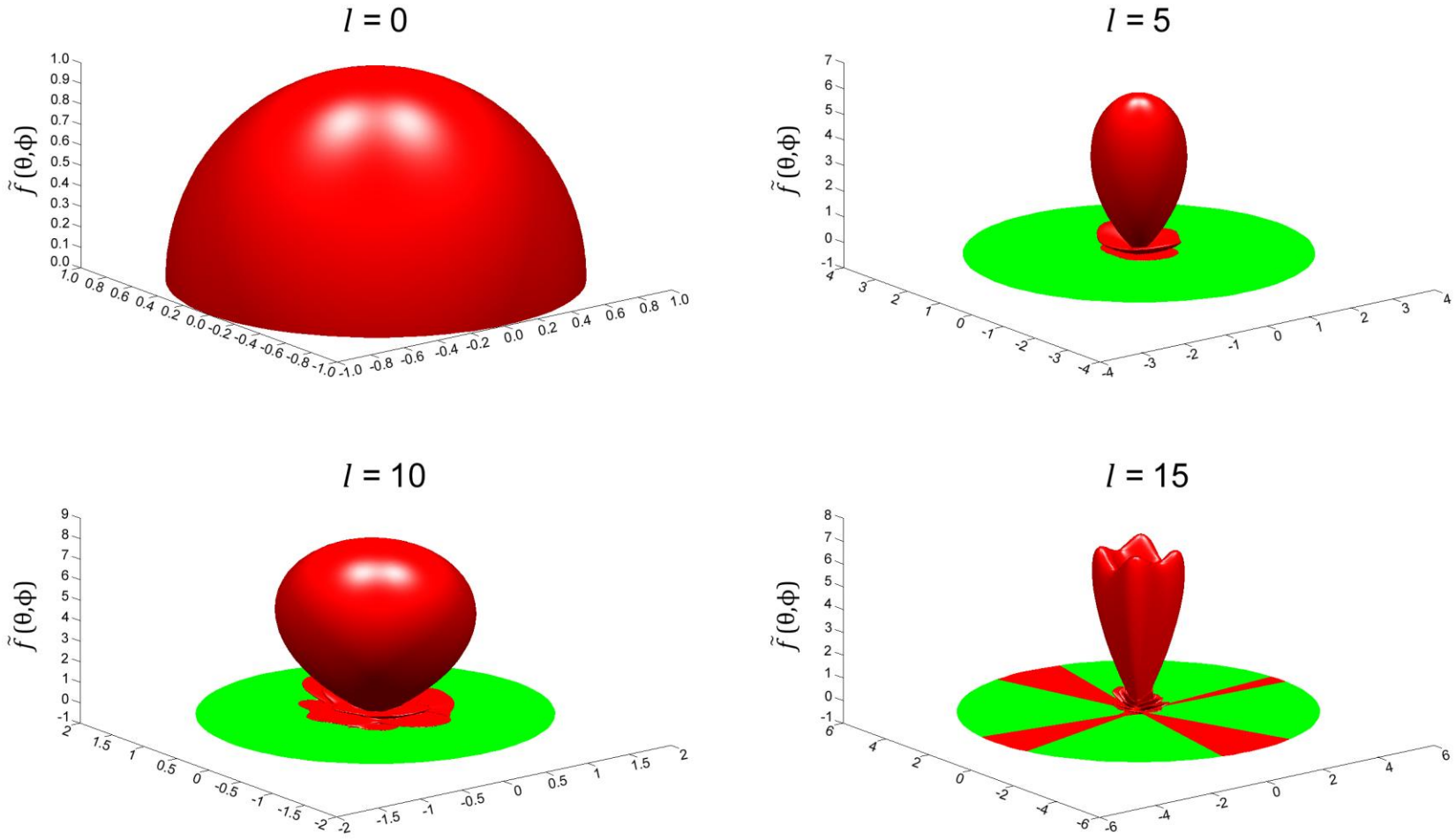

Figure 25: Reconstruction of the approximate function describing the extra-focal photon fluence derived from phase space files. Expansion orders *l* = 0, 5, 10, 15.

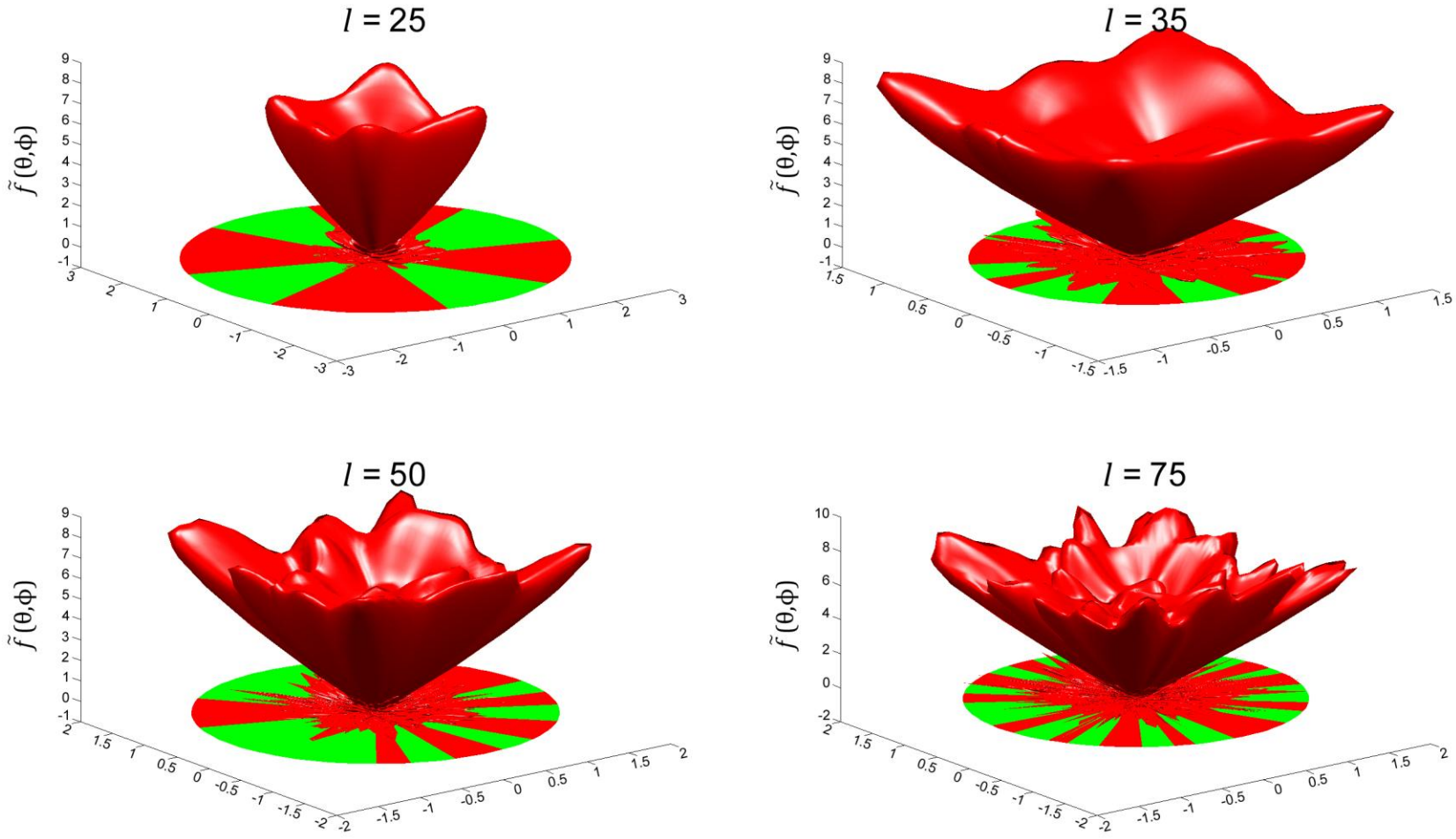

Figure 26: Reconstruction of the approximate function describing the extra-focal photon fluence derived from phase space files. Expansion orders *l* = 25, 35, 50, 75.

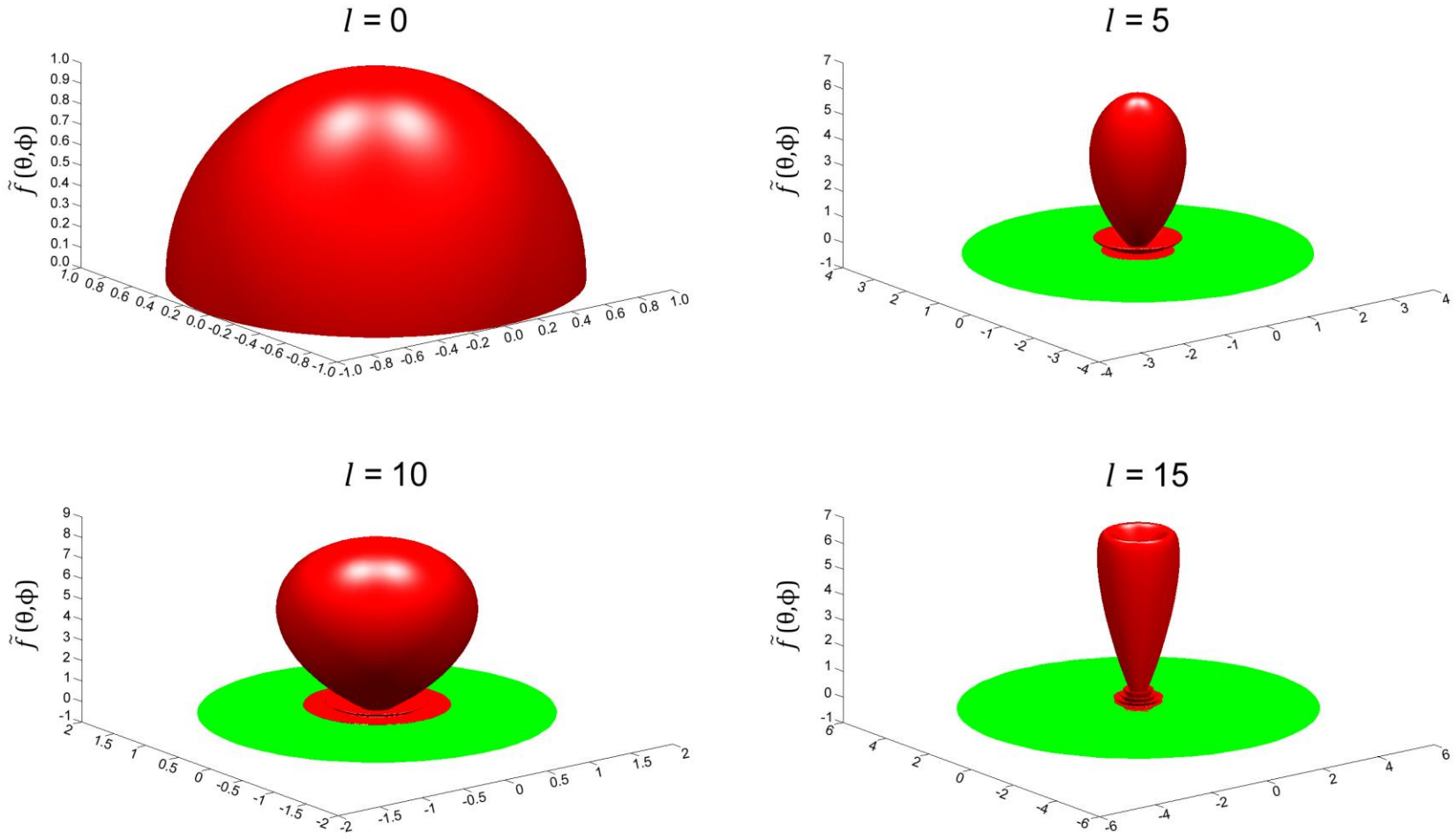

Figure 27: Reconstruction of the approximate function describing the extra-focal photon fluence derived from phase space files using zonal harmonics. Expansion orders *l* = 0, 5, 10, 15.

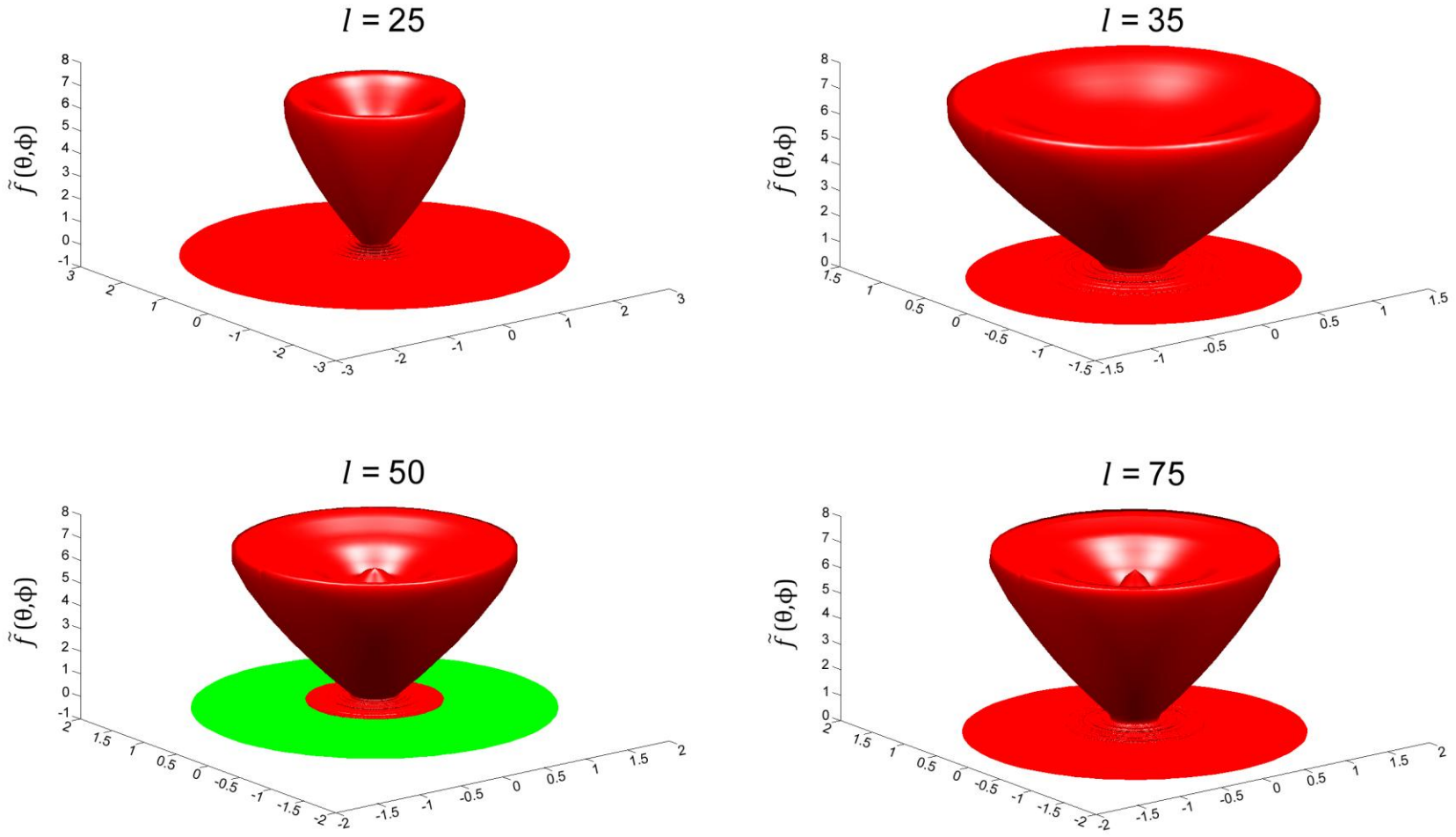

Figure 28: Reconstruction of the approximate function describing the extra-focal photon fluence derived from phase space files using zonal harmonics. Expansion orders *l* = 25, 35, 50, 75.

7.3 Expansion Order Analysis

While it is tempting to adopt the coefficients generated from the highest expansion order, it is also necessary to consider the broader context. The ultimate goal is to produce a source model and radiative transport method that when coupled produce dosimetric calculations that closely reflect the actual dose delivered. The ability of a calculation model to perform is often evaluated when compared to measurement or Monte Carlo calculations. To investigate further what expansion order produces optimal results, COMET(515151) calculations were performed using expansion orders of l = 0, 5, 15, 25, 35, and 45 for a 20x20 cm^2 field size. The 20x20 cm^2 field size was chosen to best illustrate the change associated with increasing the expansion order. Given the evidence from the preceding sections, zonal harmonics were exclusively used to generate the results. The resultant profiles at depths of 3 cm, 5 cm, and 10 cm were normalized to 100% at the central axis and compared with a DOSXYZnrc calculation using RPSD. The central 80% of the profile was used for this analysis so that the large dose differences seen in the penumbra region would not obscure the results.

Figure 29 shows dose in color wash format calculated by DOSXYZnrc with RPSD and COMET with increasing expansion orders. The lowest expansion order $l = 0$ is an isotropic point source and because of the large distance from source to phantom results in distribution that is almost flat at a plane perpendicular to the impinging radiation. As the expansion order increases the influence of the flattening filter can be seen. Also the dose falloff near the edge of the field increases with increasing expansion order.

Figures 30, 31, and 32 show plots of the profiles at depths of 3 cm, 5 cm, and 10 cm all normalized to 100% at the central axis. It is difficult to visually decide which

expansion best fits the reference calculation and the data from these profiles was used to generate Table 16. The data shows that for all depths, $l = 25$ has the lowest root-mean-square error. At 3 cm depth $l = 25$ and $l = 35$ have the same maximum error and at 5 cm and 10 cm $l = 25$ has the lowest maximum error.

The optimal expansion order therefore was chosen to be $l = 25$.

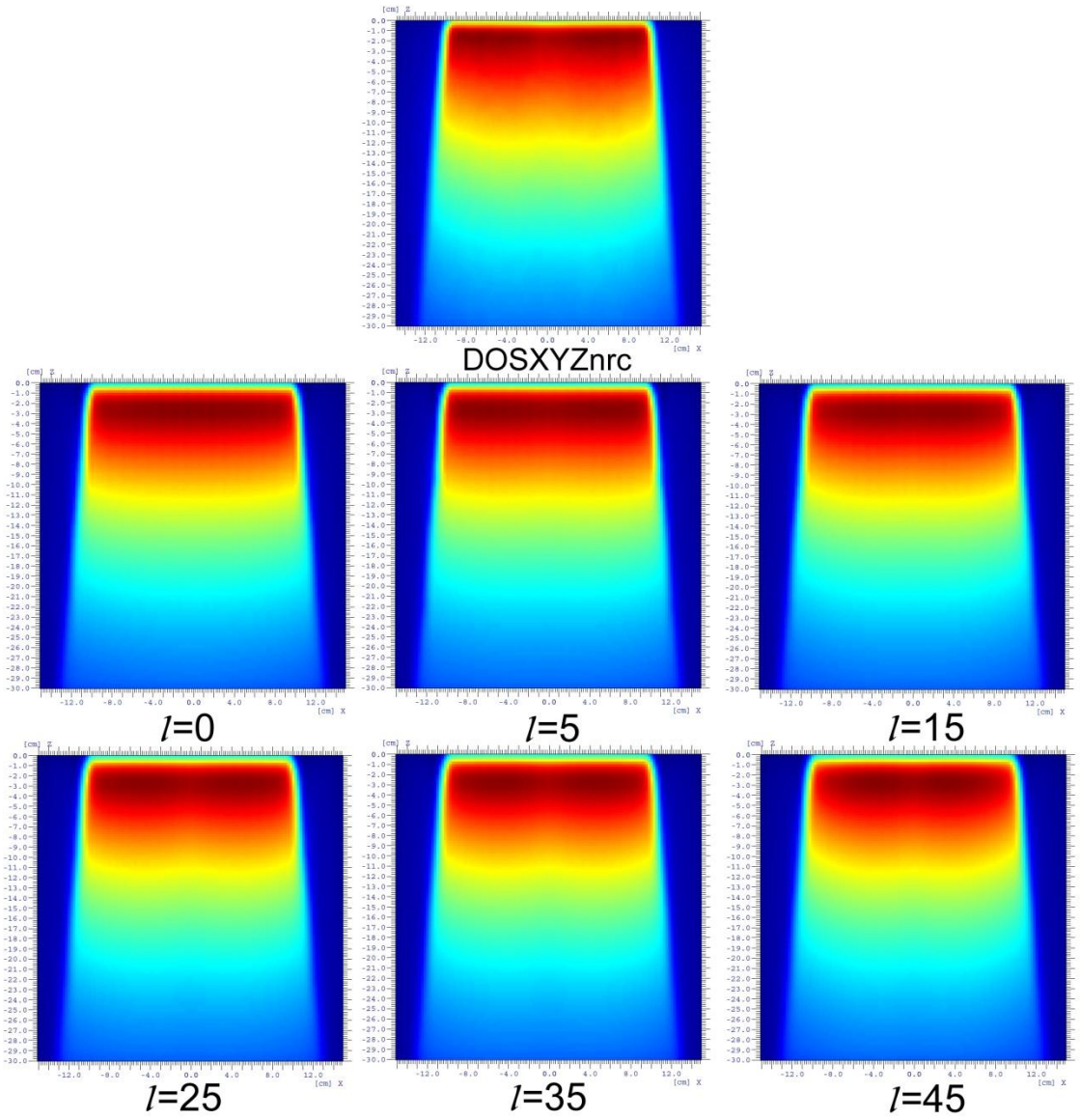

Figure 29: DOSXYZnrc calculation performed with RPSD and COMET calculations performed with increasing zonal harmonic expansion orders. A 6 MV photon beam with 20x20 cm^2 field size is impinging on a 30x30x30 cm^3 water phantom.

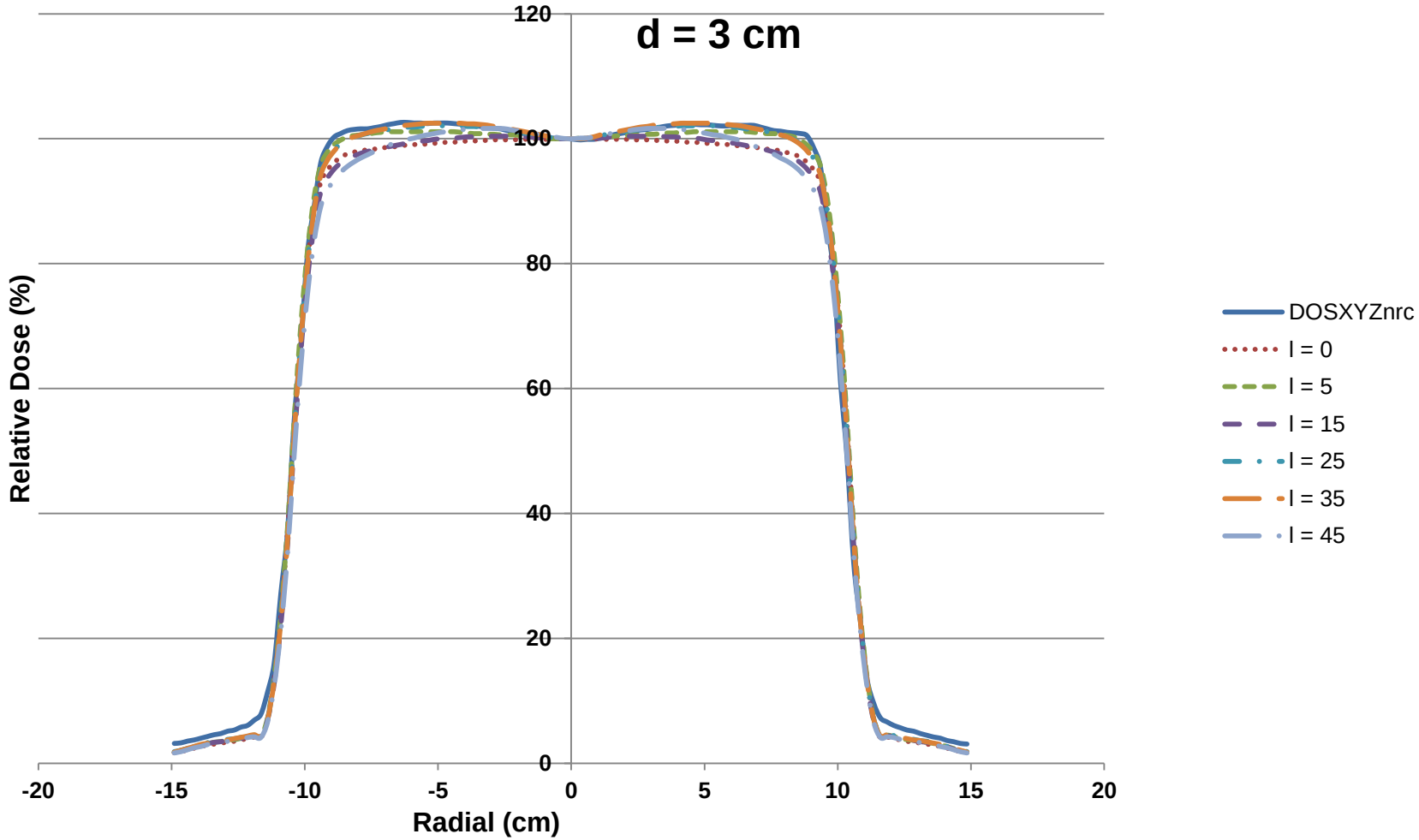

Figure 30: Profile comparison for a DOSXYZnrc calculation with RPSD and COMET calculations with increasing expansion orders at a depth of 3 cm.

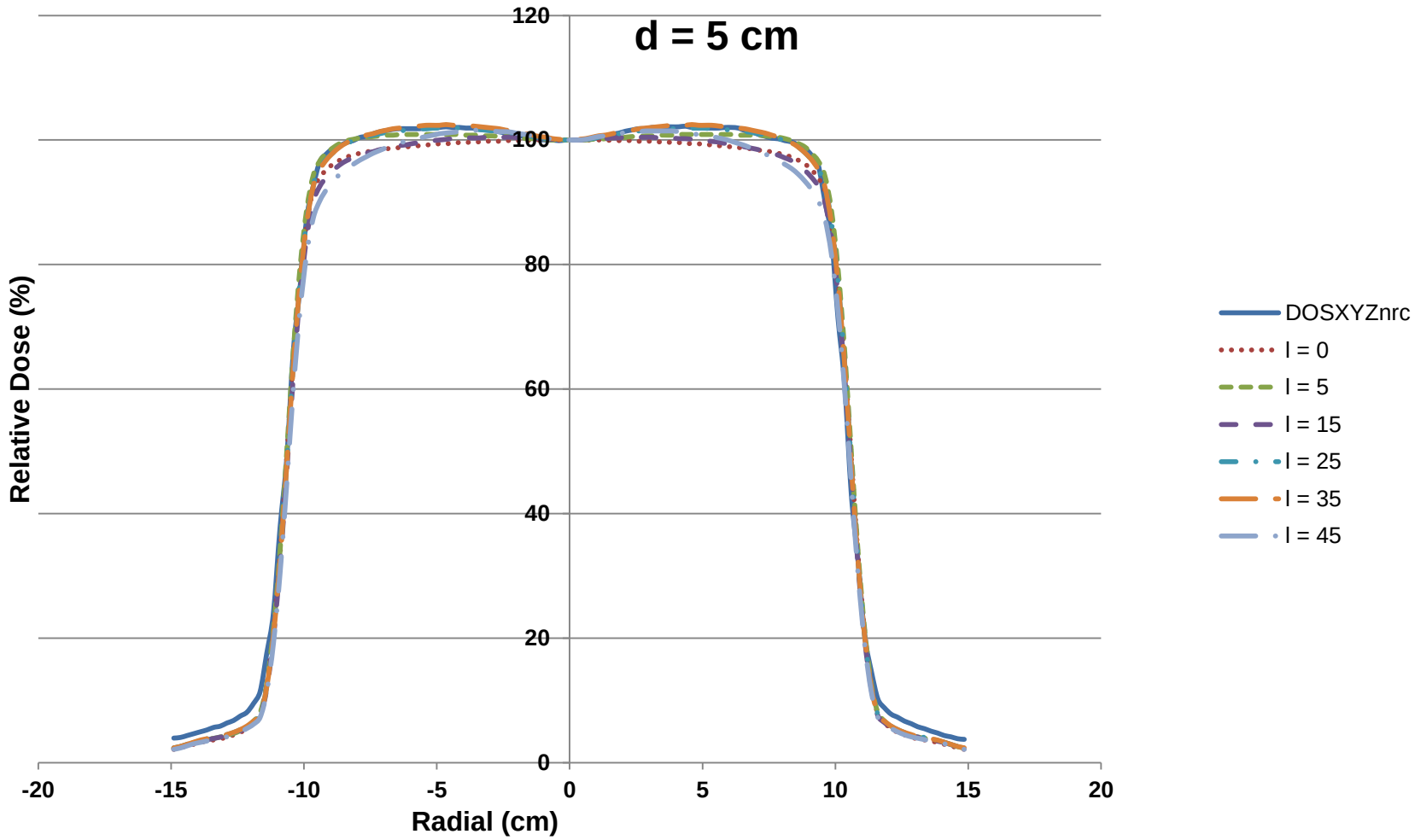

Figure 31: Profile comparison for a DOSXYZnrc calculation with RPSD and COMET calculations with increasing expansion orders at a depth of 5 cm.

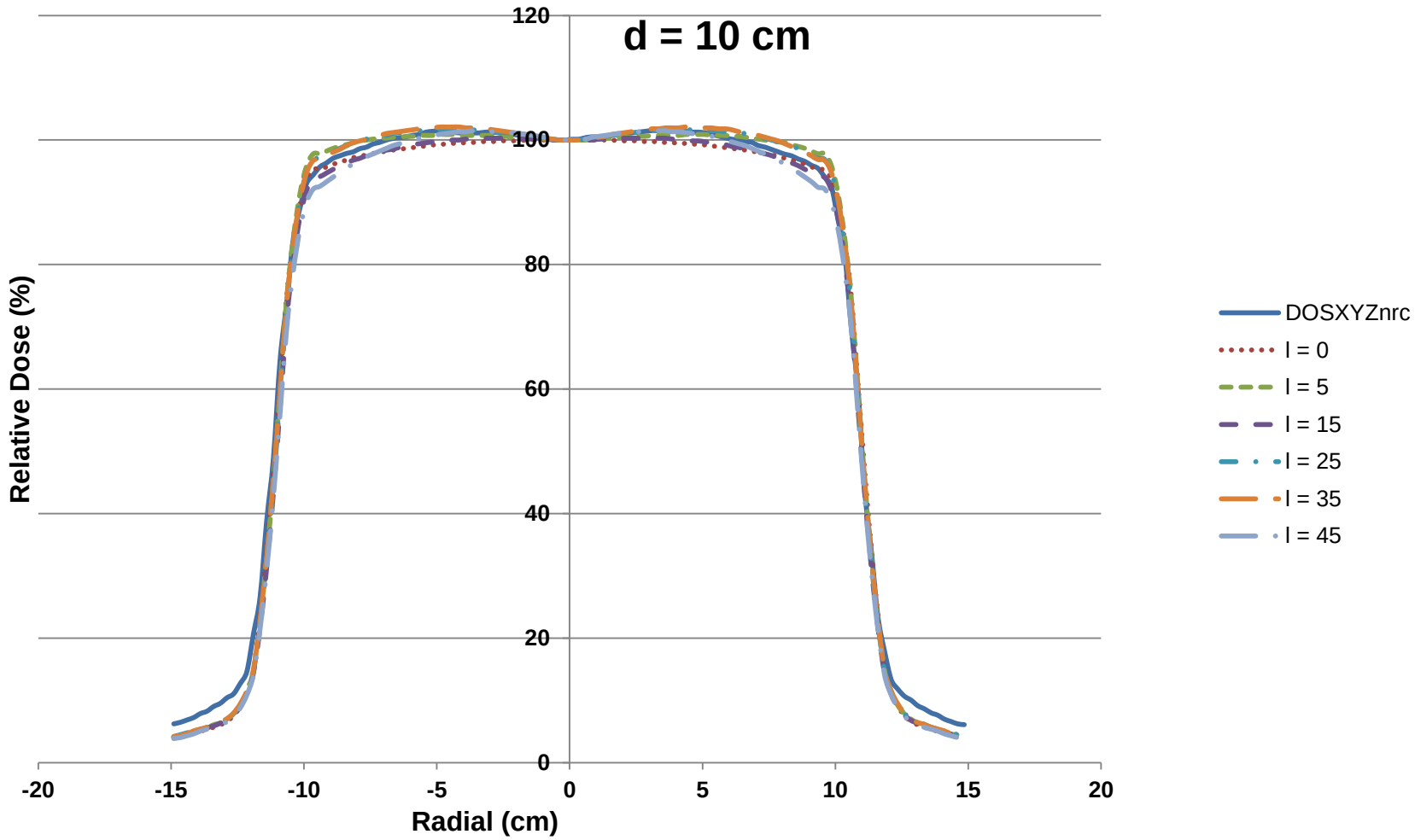

Figure 32: Profile comparison for a DOSXYZnrc calculation with RPSD and COMET calculations with increasing expansion orders at a depth of 10 cm.

Table 16: Profile relative dose error analysis for increasing zonal harmonic expansion orders at depths of 3, 5, and 10 cm. RPSD was used to generate the reference to which these profiles were compared.

depth (cm)	Expansion Order	Maximum Error (%)	RMS Error
3	$l = 0$	3.66	2.53
	$l = 5$	1.45	0.92
	$l = 15$	4.39	2.34
	$l = 25$	1.39	0.47
	$l = 35$	1.39	0.44
	$l = 45$	5.65	2.20
5	$l = 0$	3.07	2.16
	$l = 5$	1.32	0.80
	$l = 15$	3.20	1.94
	$l = 25$	0.45	0.21
	$l = 35$	0.55	0.30
	$l = 45$	4.71	1.93
10	$l = 0$	2.18	1.38
	$l = 5$	2.38	0.86
	$l = 15$	1.84	1.15
	$l = 25$	1.76	0.80
	$l = 35$	1.79	0.93
	$l = 45$	3.12	1.04

7.4 Electron Contamination

The free parameters α and β of the electron contamination curve were manually selected to best match the dose in the buildup region to the reference dose calculated by DOSXYZnrc. The electron contamination accounts for less than 10% of the dose at the surface and exhibits a rapid falloff with depth. These characteristics are reflected in the electron contamination curve used for COMET calculations and shown in Figure 33.

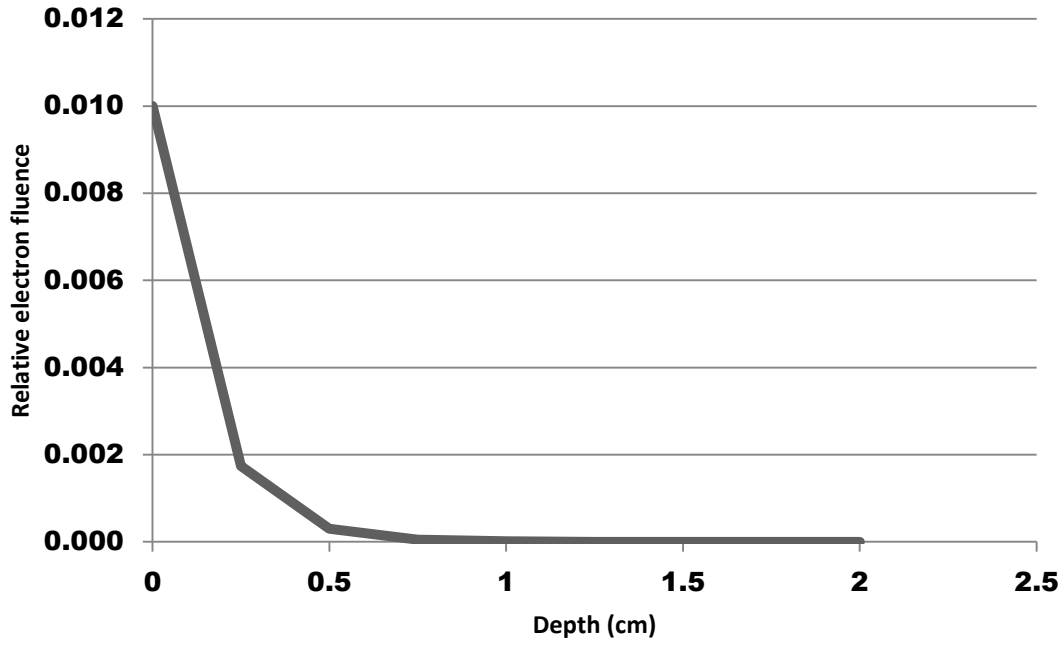

Figure 33: Relative electron fluence

7.5 Water Phantom

7.5.1 Profiles

The percentage axis depth doses and profiles for a 30x30x30 cm^2 water phantom at depths of 1.5, 5, and 10 cm were compared and the maximum and root-mean-square

error is reported. All dose distributions were normalized with the point of maximum dose along central axis equal to 100%. This method of normalization is customary when presenting PDDs. The prescription dose was also set as 100 cGy the point of maximum dose along central axis. The percentage depth doses and profiles for field sizes 4x4, 10x10, and 20x20 cm^2 are illustrated in Figures 34-45. Tables 17 and 18 summarize the results of the error analysis.

COMET(515151) had a lower maximum percentage error and lower root-mean-square error in all percentage depth dose comparisons performed except in the root-mean-square error past D_{max} for the 20x20 cm^2 field and the maximum error past D_{max} for the 4x4 cm^2 and 20x20 cm^2 field. Both AAA and AXB exhibited very high errors in the buildup region when compared to the DOSXYZnrc calculation.

The results of the comparisons of the profiles at depth varied more than the percentage depth doses. AAA had the lowest error values in 3 out of the 36 tests, AXB had the lowest error values in 10 out of the 36 tests, and COMET had the lowest error values in 23 out of the 36 tests. The highest percentage error values were seen in the penumbra regions with maximum percentage error reaching as high as 62.82%. This is expected and illustrates the importance of also using a method of comparison that takes into account both dose and spatial agreement such as the gamma method.

Table 17: Maximum and root-mean-square error for central axis percentage depth doses in a water phantom. All curves are normalized with D_{max}=100%.

	4x4 cm^2		10x10 cm^2		20x20 cm^2	
	All Depths		All Depths		All Depths	
	Maximum Error (%)	RMS Error	Maximum Error (%)	RMS Error	Maximum Error (%)	RMS Error
AAA	35.33	4.35	28.73	3.34	37.41	4.21
AXB	40.20	4.61	16.96	1.83	34.57	4.14
COMET(515151)	27.51	3.79	2.01	0.81	3.19	0.71
	Past D_{max}		Past D_{max}		Past D_{max}	
	Maximum Error (%)	RMS Error	Maximum Error (%)	RMS Error	Maximum Error (%)	RMS Error
AAA	4.46	2.54	5.05	1.68	4.08	2.26
AXB	4.38	2.46	2.40	0.92	2.89	1.39
COMET(515151)	5.00	2.22	2.01	0.80	3.19	0.68

Table 18: Maximum and root-mean-square relative dose error for profiles in a water phantom.

	4x4 cm^2		10x10 cm^2		20x20 cm^2	
d=1.5 cm	Central 80%		Central 80%		Central 80%	
	Maximum Error (%)	RMS Error	Maximum Error (%)	RMS Error	Maximum Error (%)	RMS Error
AAA	0.90	0.37	1.29	0.62	1.74	0.68
AXB	0.80	0.35	1.11	0.48	1.45	0.81
COMET(515151)	1.28	0.59	1.79	1.07	3.81	1.90
	80-120%		80-120%		80-120%	
	Maximum Error (%)	RMS Error	Maximum Error (%)	RMS Error	Maximum Error (%)	RMS Error
AAA	23.08	14.28	47.04	24.39	62.82	27.63
AXB	23.08	14.09	47.04	23.36	62.71	25.30
COMET(515151)	45.17	19.61	47.59	24.58	61.41	22.94
d=10 cm	Central 80%		Central 80%		Central 80%	
	Maximum Error (%)	RMS Error	Maximum Error (%)	RMS Error	Maximum Error (%)	RMS Error
AAA	1.61	1.03	1.22	0.75	3.05	2.04
AXB	1.45	0.91	0.90	0.57	2.07	1.21
COMET(515151)	1.31	1.03	1.35	0.53	1.13	0.58
	80-120%		80-120%		80-120%	
	Maximum Error (%)	RMS Error	Maximum Error (%)	RMS Error	Maximum Error (%)	RMS Error
AAA	42.84	19.42	41.40	17.82	50.58	18.86
AXB	42.84	19.45	40.81	13.69	52.17	19.13
COMET(515151)	23.24	9.94	22.16	10.55	39.52	12.87
d=20 cm	Central 80%		Central 80%		Central 80%	
	Maximum Error (%)	RMS Error	Maximum Error (%)	RMS Error	Maximum Error (%)	RMS Error
AAA	2.99	2.46	2.39	1.40	1.49	1.00
AXB	2.99	2.46	1.31	0.78	1.19	0.73
COMET(515151)	1.83	0.68	1.03	0.49	1.83	0.68
	80-120%		80-120%		80-120%	
	Maximum Error (%)	RMS Error	Maximum Error (%)	RMS Error	Maximum Error (%)	RMS Error
AAA	37.03	13.59	32.62	11.31	36.06	13.43
AXB	37.03	13.59	31.59	6.82	36.06	13.42
COMET(515151)	14.92	6.13	17.98	6.59	14.92	6.13

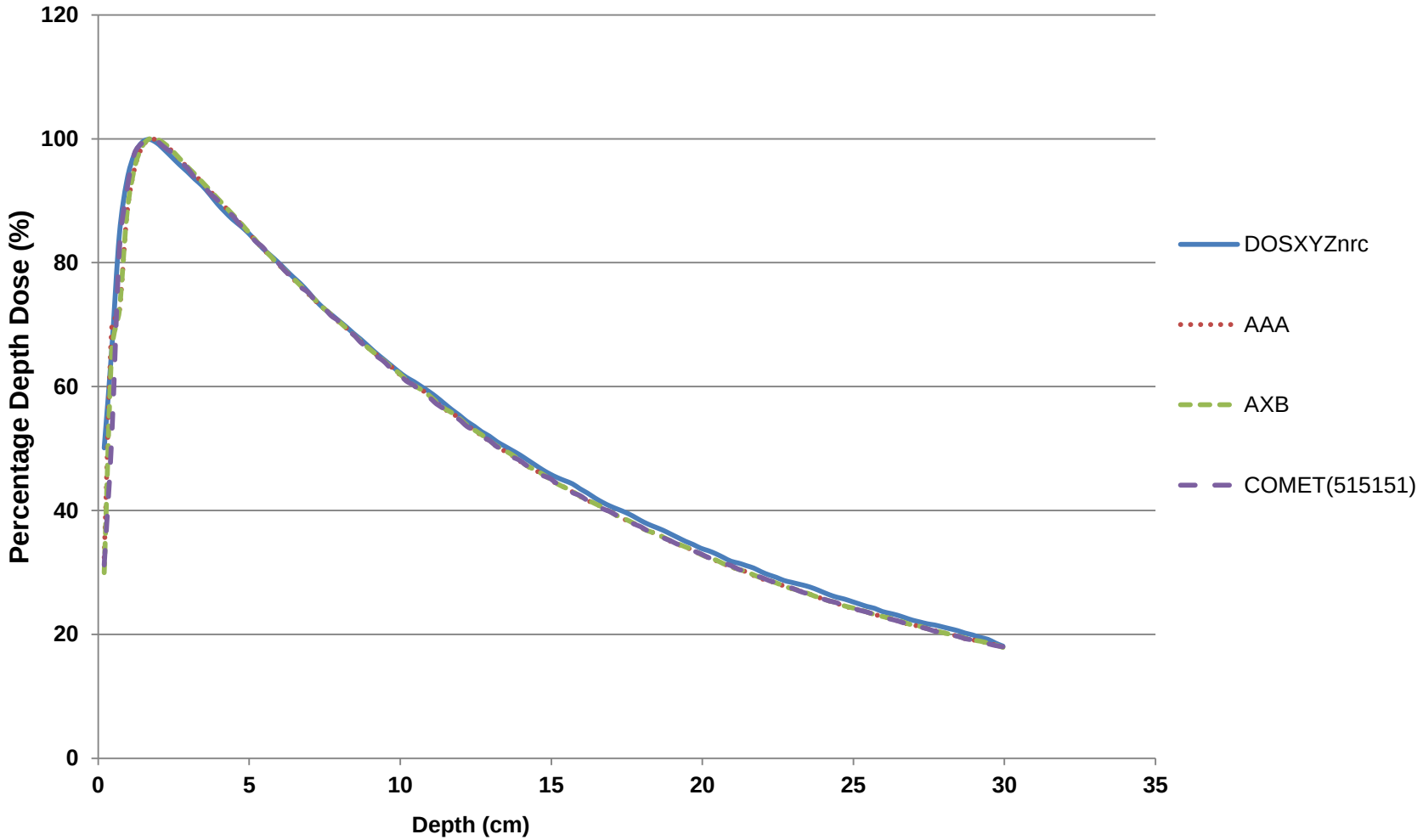

Figure 34: Water phantom percentage depth dose with a field size of 4x4 cm^2

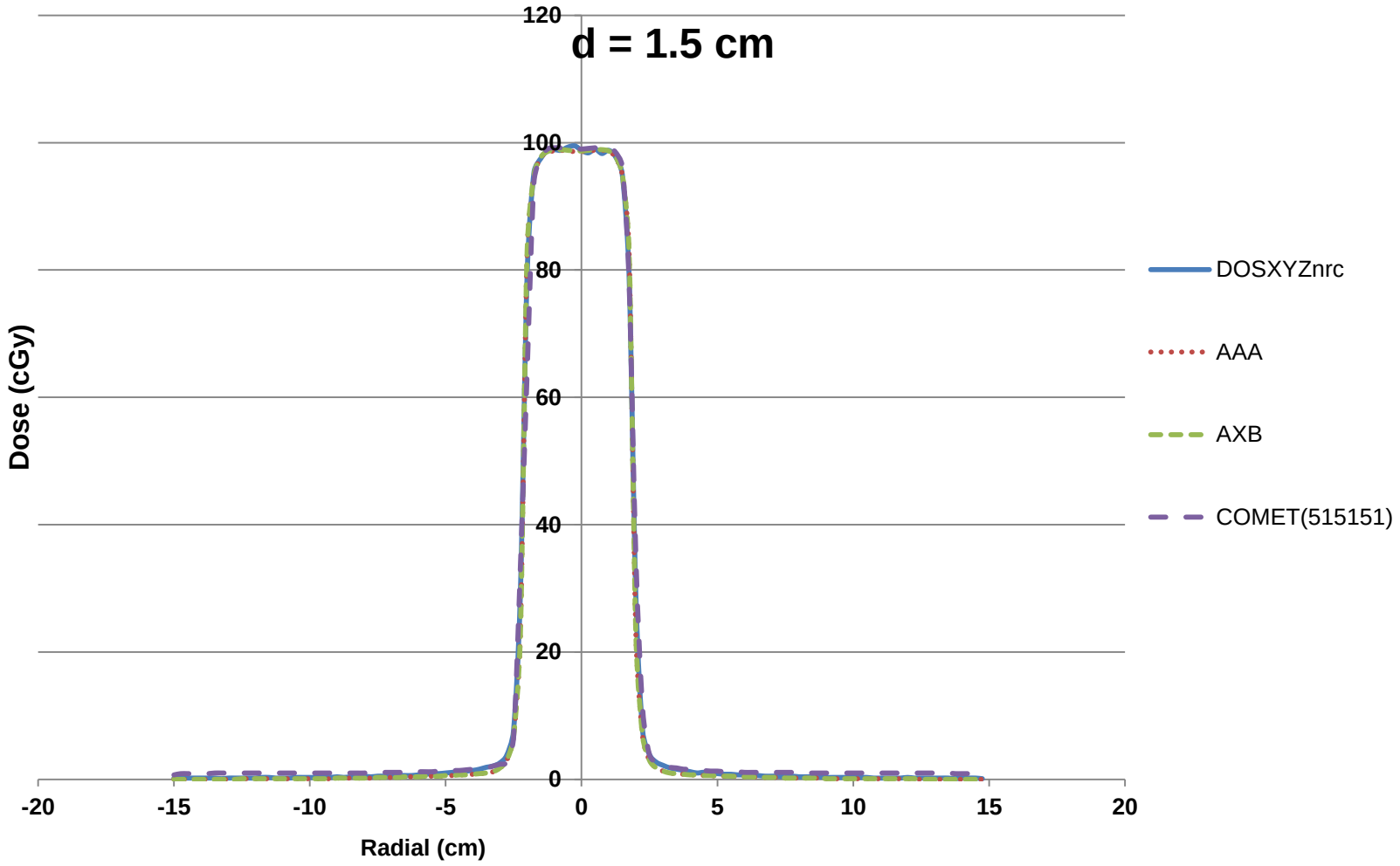

Figure 35: Water phantom profile at a depth of 1.5 cm with a 4x4 cm^2 field size

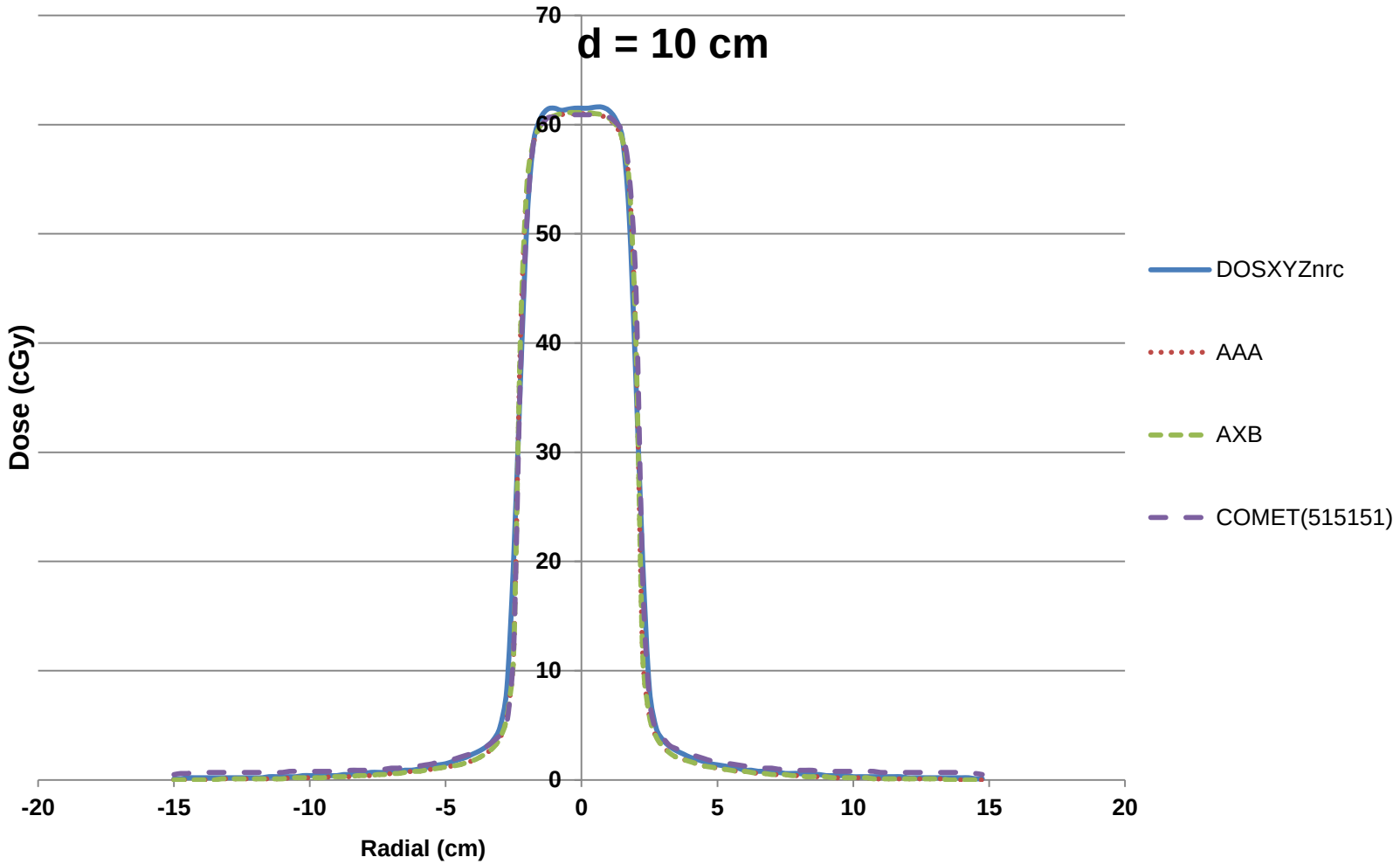

Figure 36: Water phantom profile at a depth of 10 cm with a 4x4 cm^2 field size

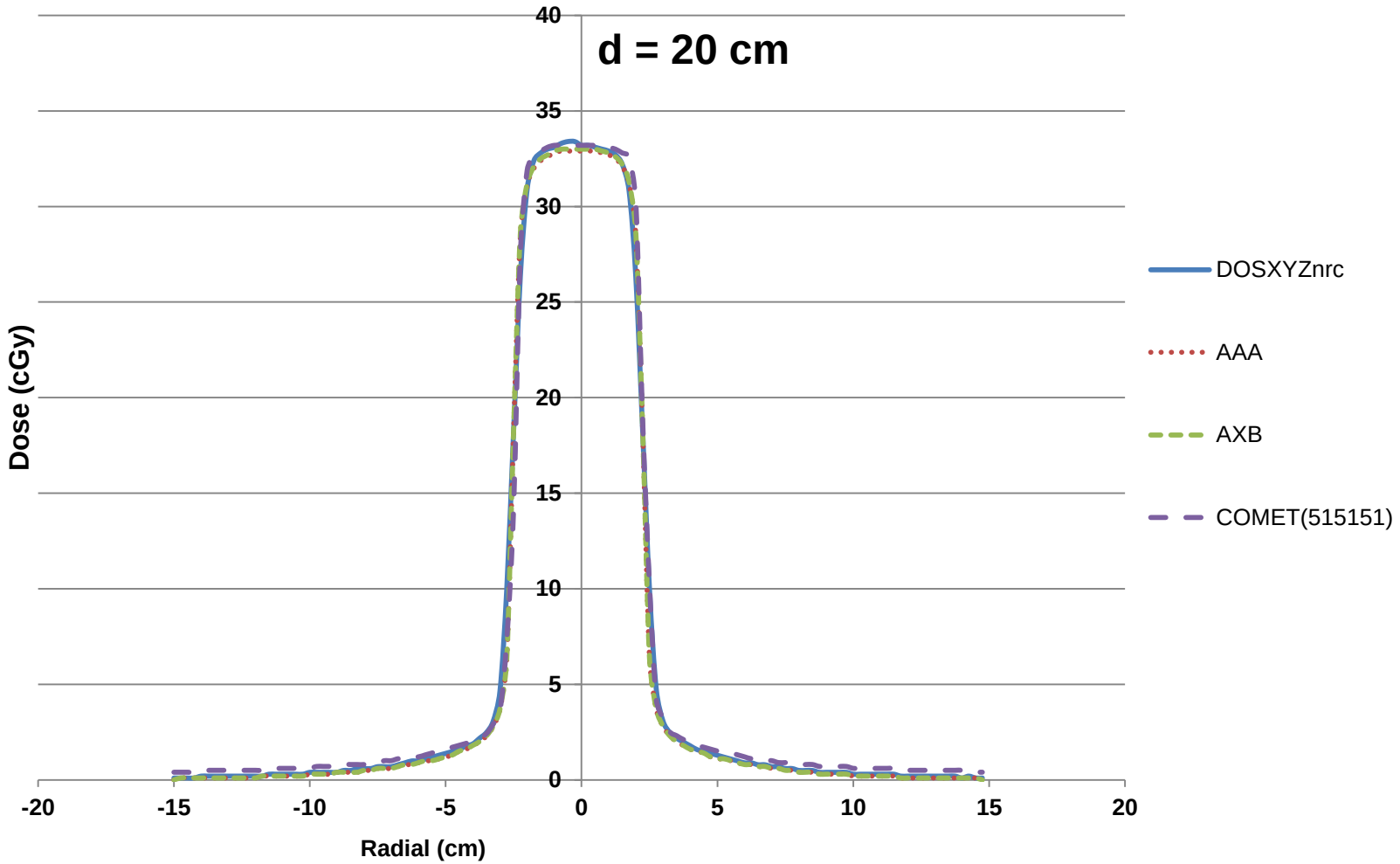

Figure 37: Water phantom profile at a depth of 20 cm with a 4x4 cm^2 field size

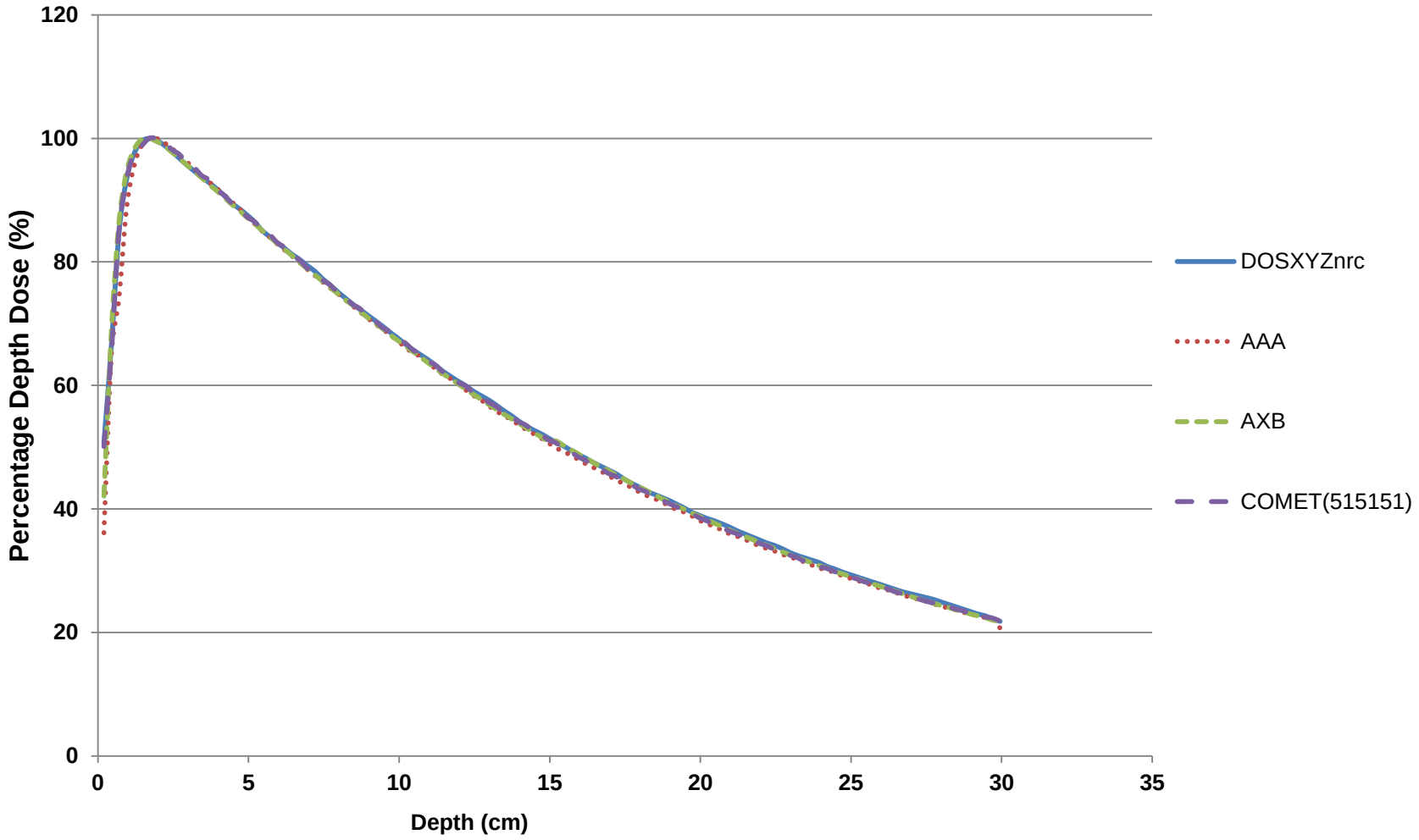

Figure 38: Water phantom percentage depth dose with a field size of 10x10 cm^2

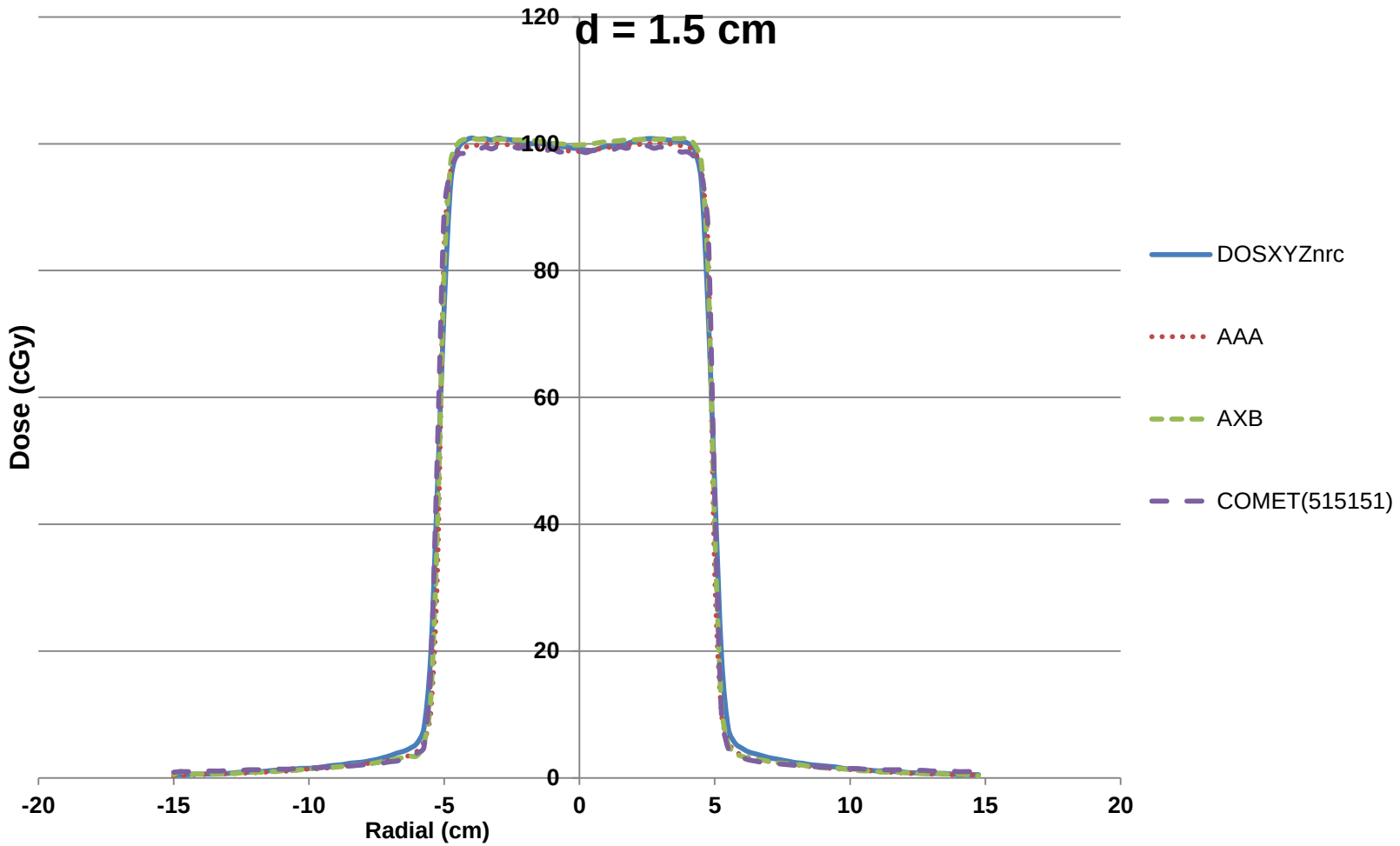

Figure 39: Water phantom profile at a depth of 1.5 cm with a 10x10 cm^2 field size

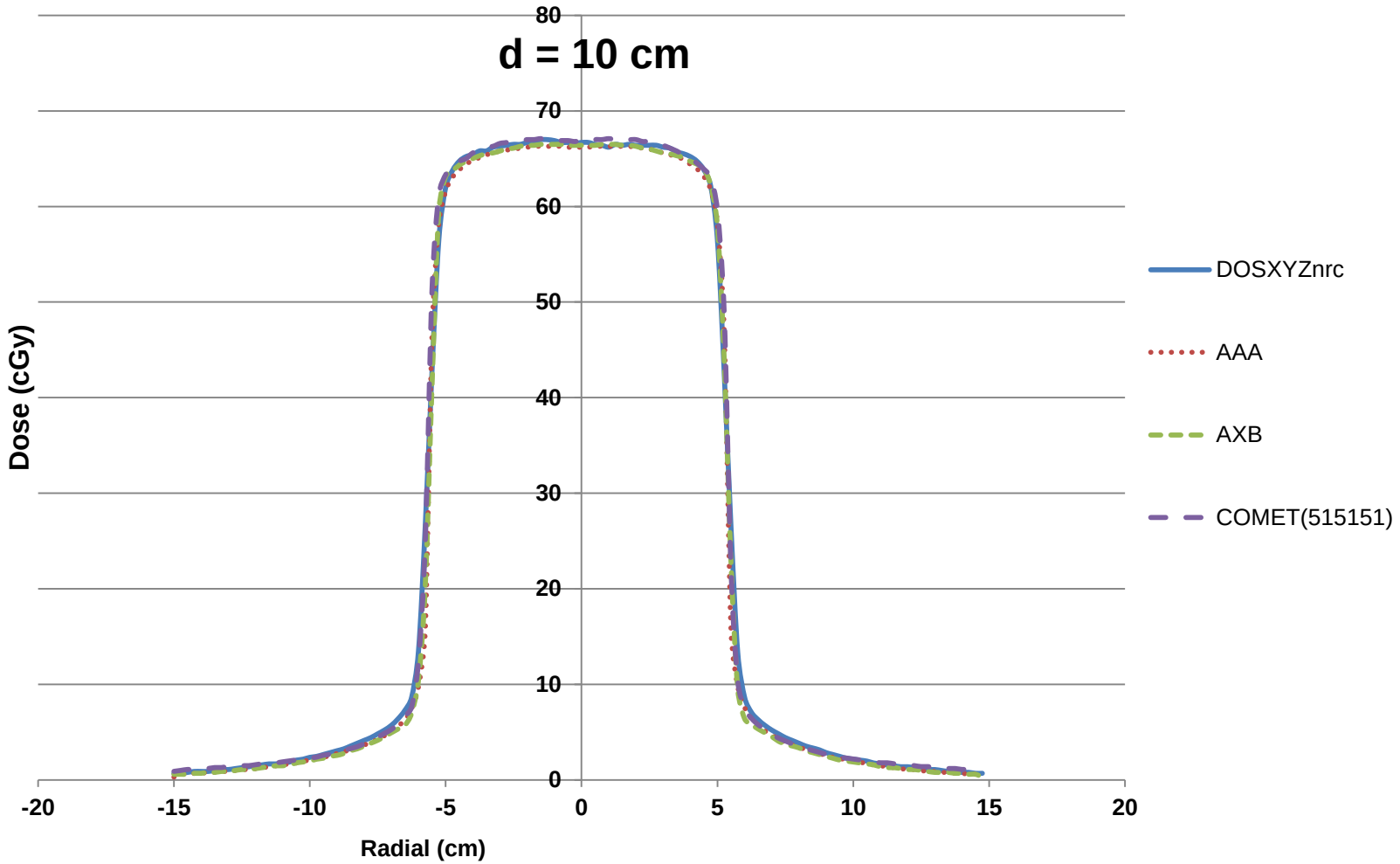

Figure 40: Water phantom profile at a depth of 10 cm with a 10x10 cm^2 field size

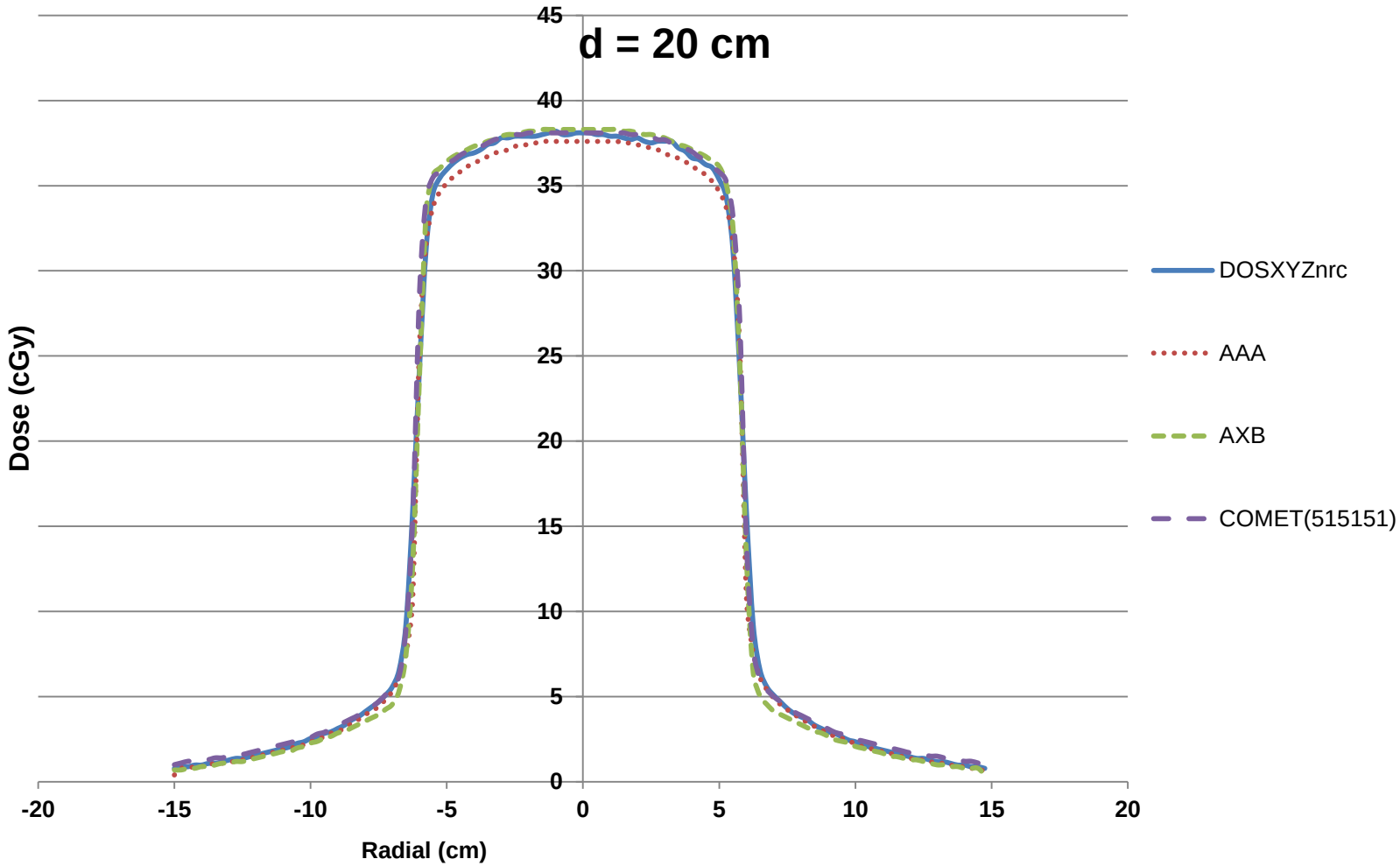

Figure 41: Water phantom profile at a depth of 20 cm with a 10x10 cm^2 field size

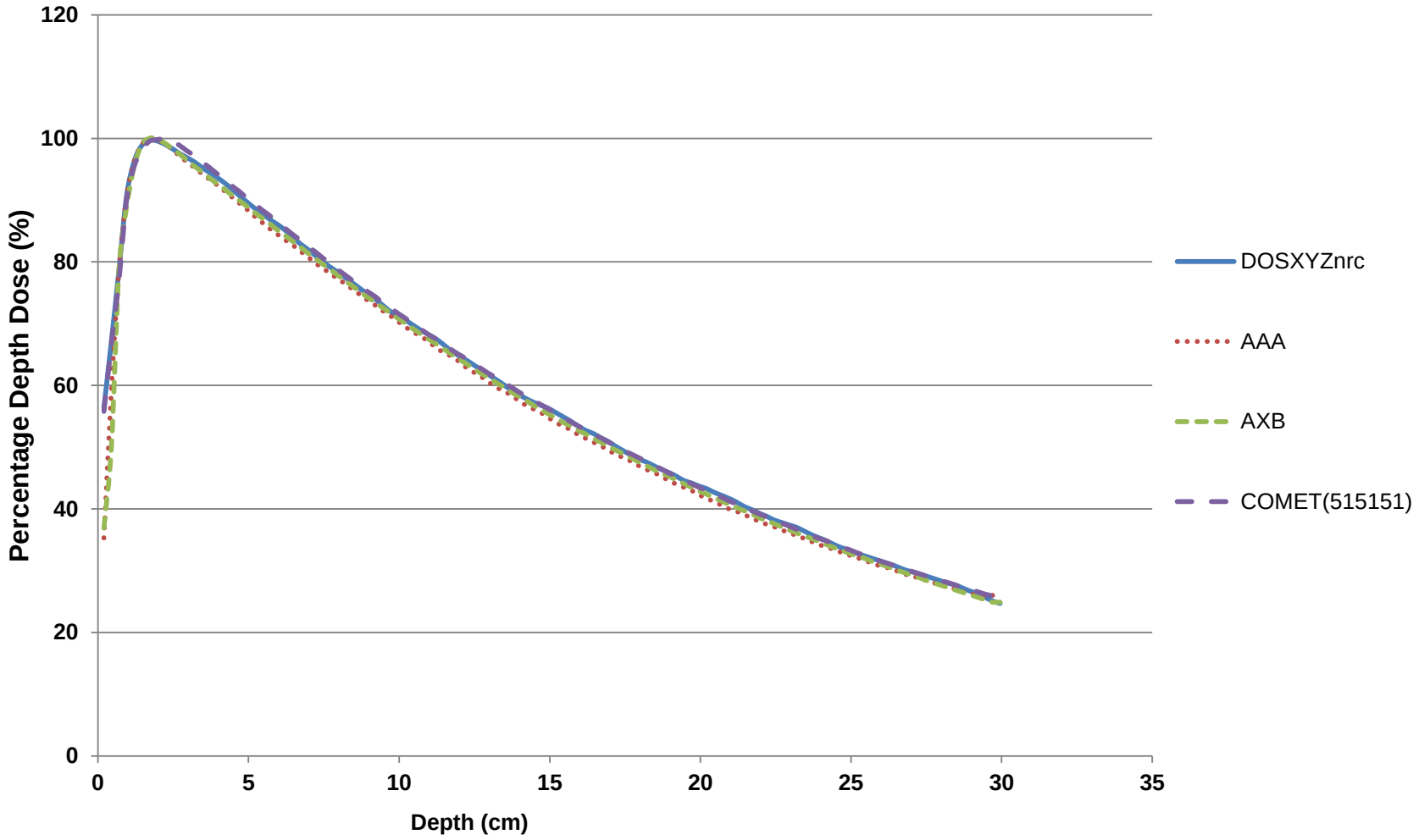

Figure 42: Water phantom percentage depth dose with a field size of 20x20 cm^2

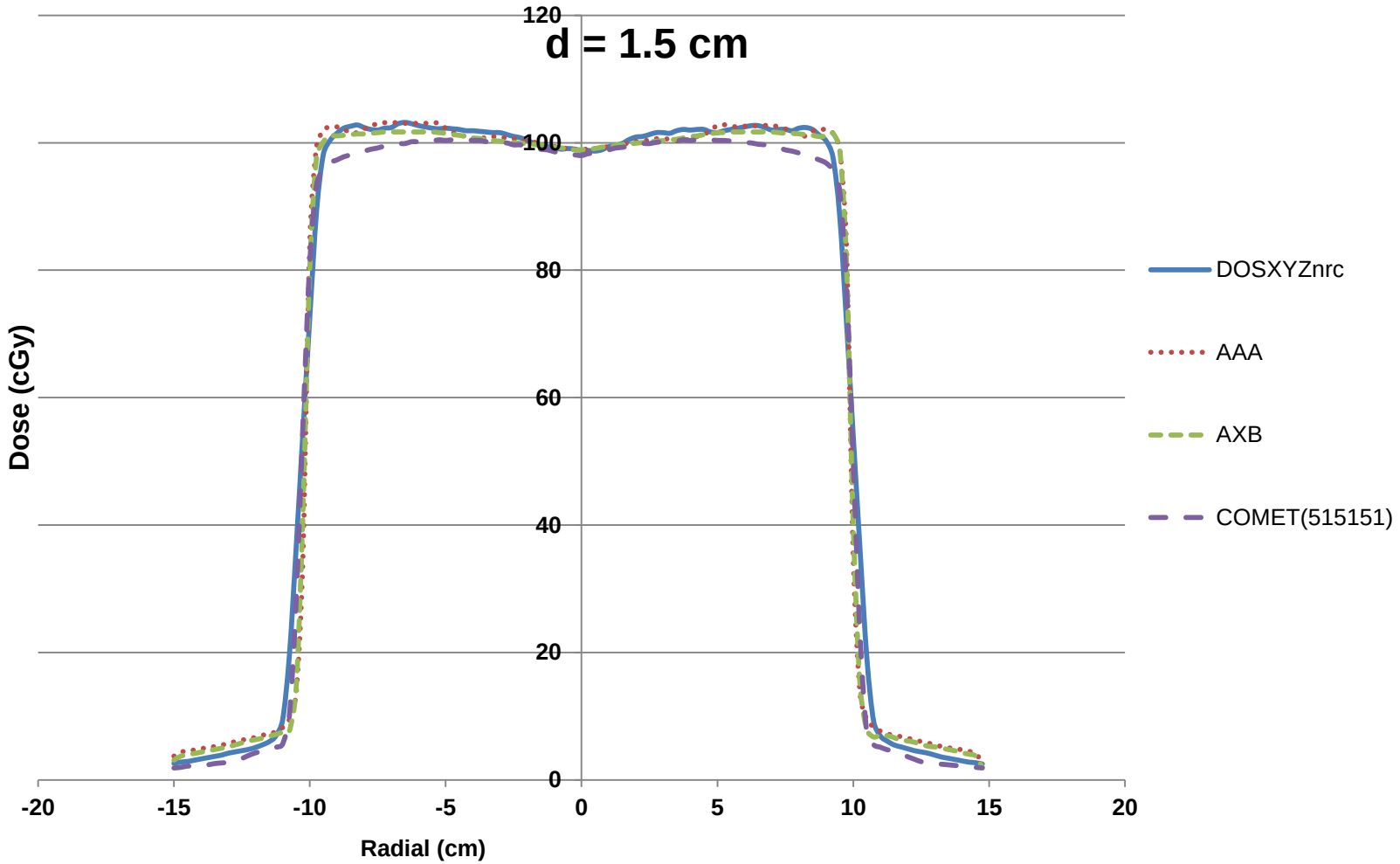

Figure 43: Water phantom profile at a depth of 1.5 cm with a 20x20 cm^2 field size

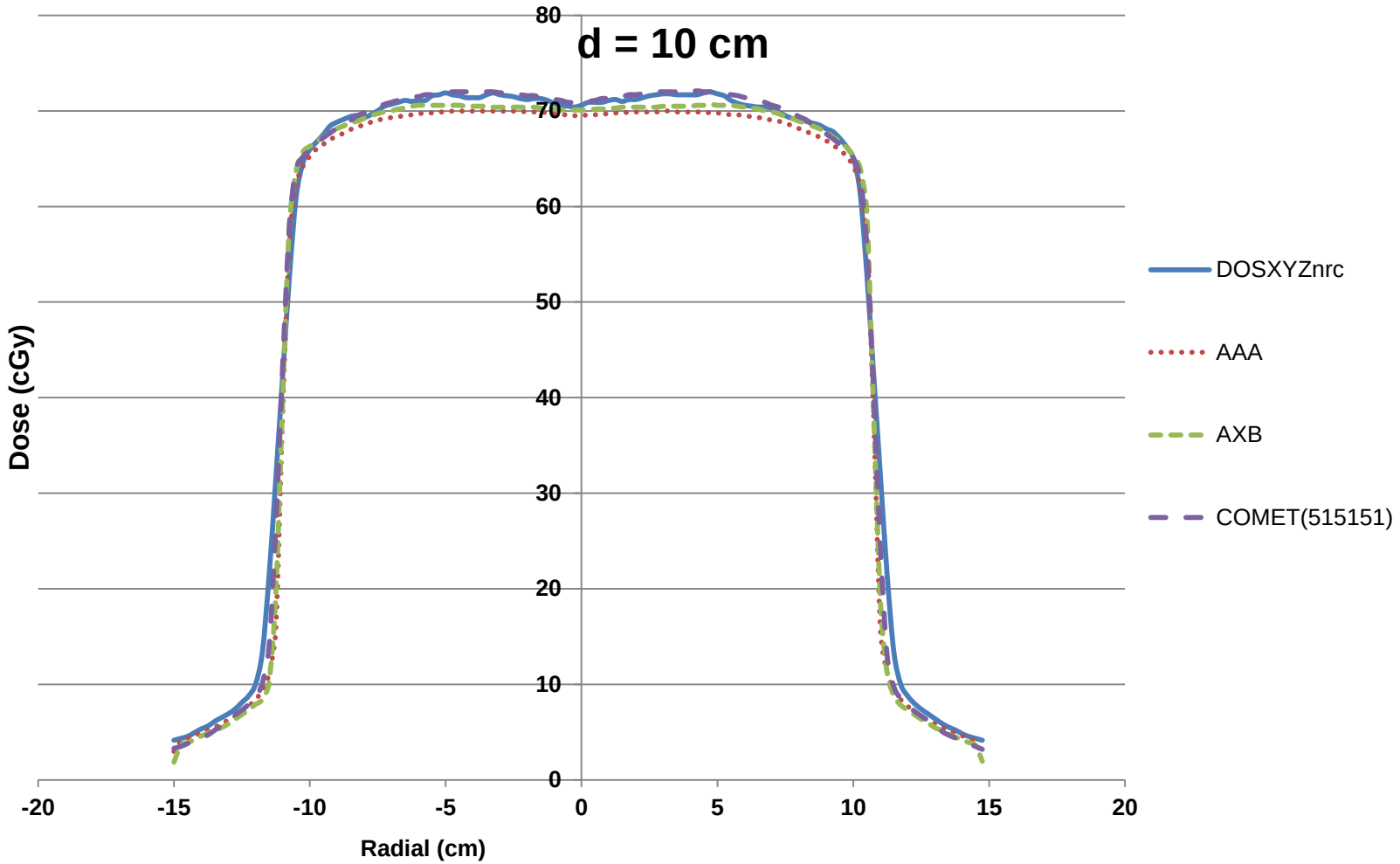

Figure 44: Water phantom profile at a depth of 10 cm with a 20x20 cm^2 field size

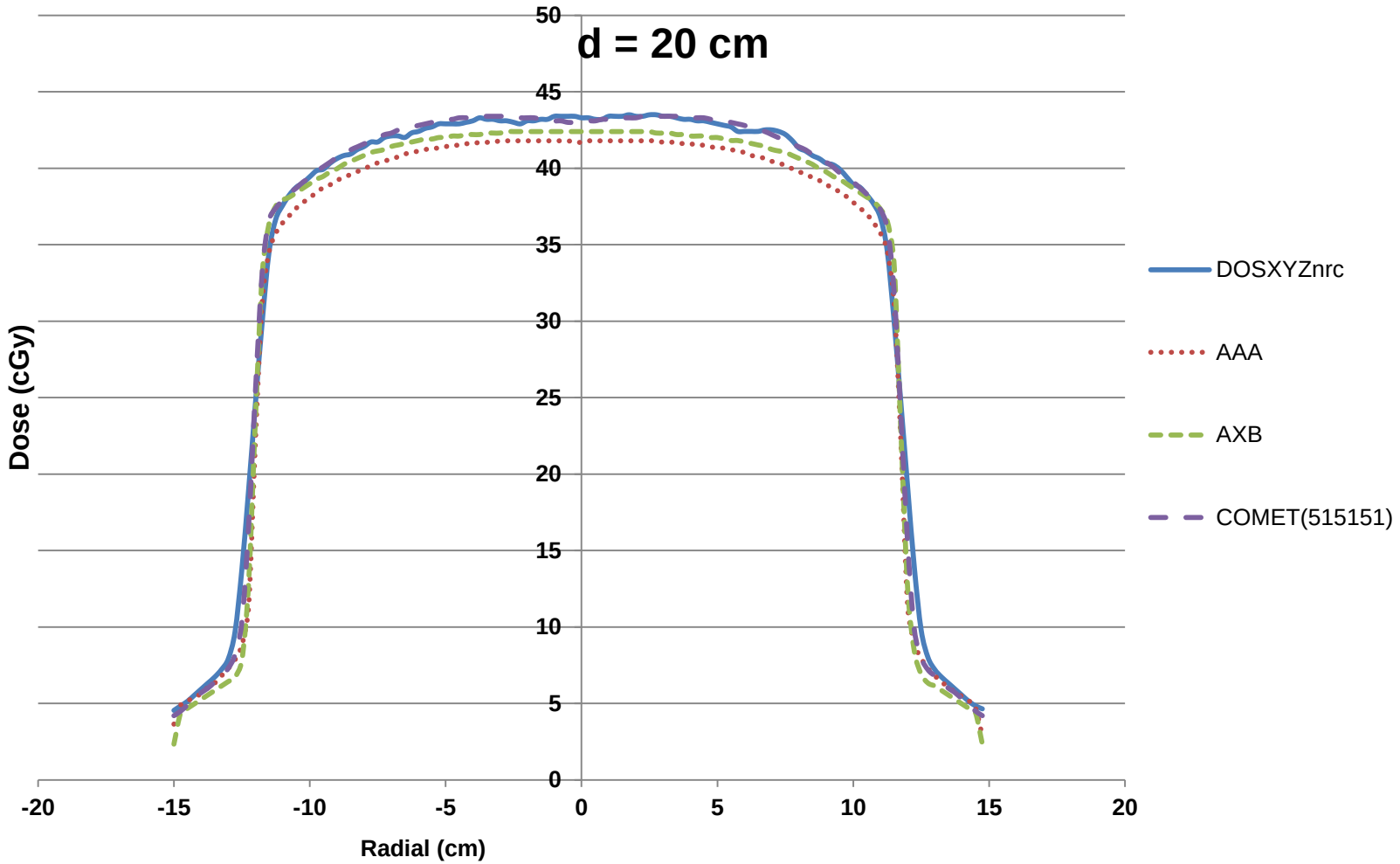

Figure 45: Water phantom profile at a depth of 20 cm with a 20x20 cm^2 field size

7.5.2 Gamma Evaluation

Calculations were performed that represent the dose deposited in a 30x30x30 cm^3 water phantom by a 6 MV therapeutic radiation beam. The results of each method were compared to the reference calculation generated using RPSD and DOSXYZnrc. The gamma method was used to compare the dose planes along the central axis in the radial direction. The region of interest used for evaluating each result was set as a rectangle that encompasses the entire 30 cm depth and 1 cm laterally beyond the field edge at the point where the field exits the phantom. For example the region of interest for the 4x4 cm^2 field size is a rectangle 30 cm in the z-direction and 5.2 cm in the x-direction. The results are shown in Figures 46, 47, and 48. Blue represents the pixels that have passed with a 1%/1mm DTA criteria and red represents those that have failed. In all calculation methods failing pixels occur mainly in the buildup region and in the penumbra. This is expected because of the tight pass/fail criteria.

Table 19 summarizes the percentage of pixels in each analysis that have passed. COMET(515151) calculations in water demonstrate a higher percentage of pixels with passing gamma scores than both AAA and AXB for all field sizes tested. AAA exhibited the lowest percentage of passing pixels for the 4x4 cm^2 and the 10x10 cm^2 field sizes and AXB had the lowest percentage for the 20x20 cm^2 field size, although the difference between AAA and AXB at 20x20 cm^2 was only 0.23%.

Table 19: Gamma Scores for Water Phantom

Field Size	4x4 cm^2	10x10 cm^2	20x20 cm^2
	$\Gamma < 1$ (%)	$\Gamma < 1$ (%)	$\Gamma < 1$ (%)
AAA	60.79	76.50	78.35
AXB	65.05	78.07	78.12
COMET(515151)	83.89	84.94	83.62

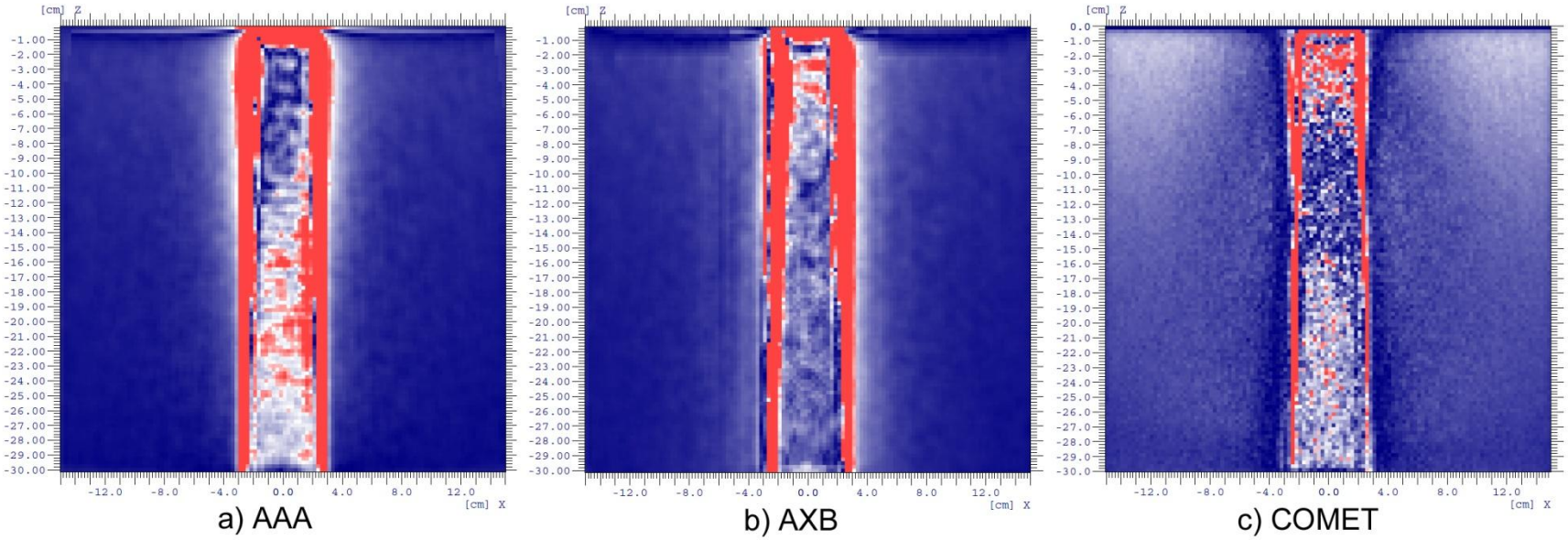

Figure 46: Gamma results in water phantom 4x4 cm^2

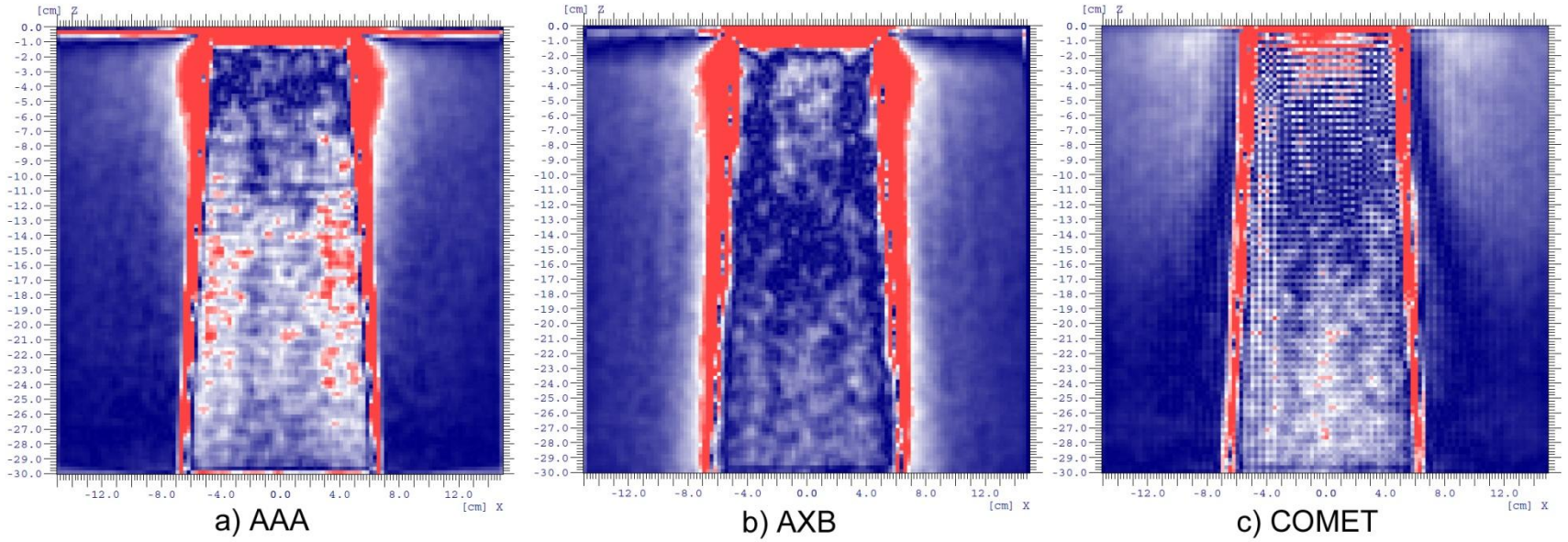

Figure 47: Gamma results in water phantom 10x10 cm^2

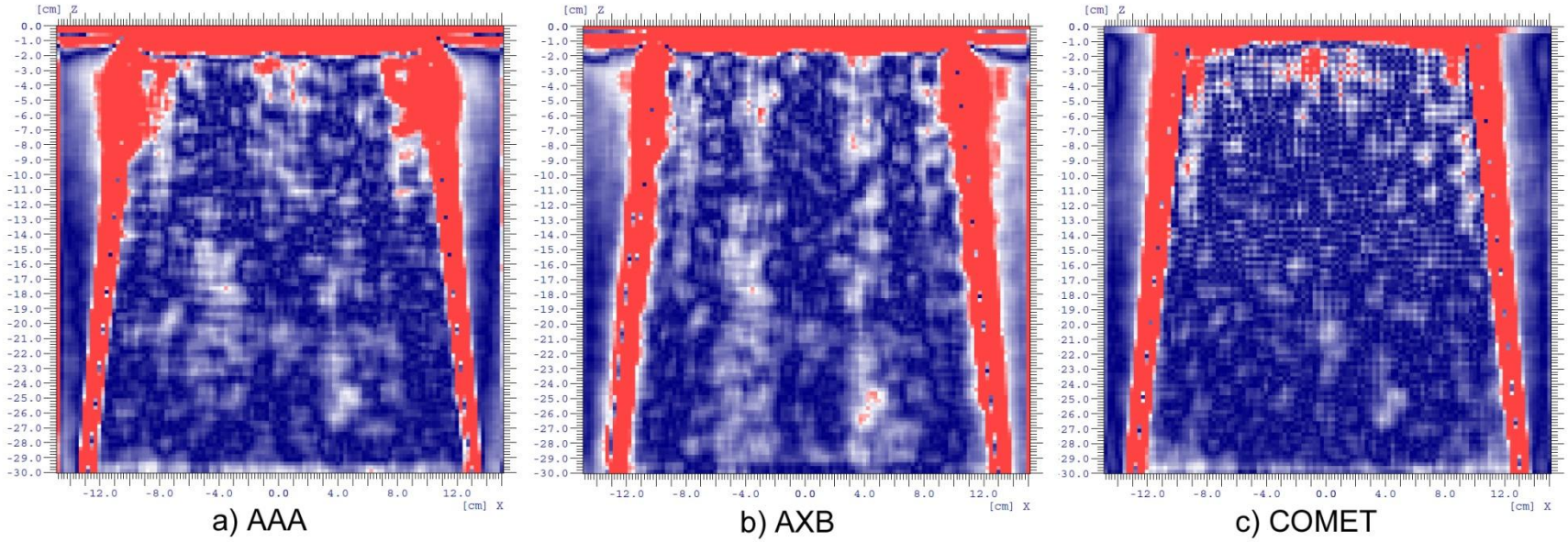

Figure 48: Gamma results in water phantom 20x20 cm^2

7.6 Slab Phantom

7.6.1 Profiles

Analysis of the percentage depth doses and profiles at various depths were performed similar to that of the water phantom. However for the percentage depth dose curves, each slab was analyzed separately. Using the same convention as section 7.5, central axis percentage depth doses are normalized with the maximum dose equaling 100%.

Tables 20 and 21 summarize the numerical results of the error analysis. Figures 49-60 show the percentage depth doses and profiles at depths of 1.5, 10, and 20 cm. COMET and AXB had very similar results along the central axis. AXB did outperform COMET in the 4x4 cm^2 field. AAA did not have the lowest error in any tests along the central axis.

The highest maximum relative error in central axis percentage depth dose was 14.38% in the bone region using AAA and a 4x4 cm^2 field size. AAA consistently underestimated the dose deposited in the lung region for all field sizes. It also did not predict the peak-and-trough curves caused by the backscatter effect near the bone interfaces.

The profiles again had varied results, but overall COMET had the lowest error in 18 of the 36 tests performed. AAA performed poorly with the lowest error in only 5 of the 36 tests. The error remains high in the penumbra region but these regions of the beam are better evaluated using the gamma method due the rapid dose falloff.

Table 20: Maximum and root-mean-square error for central axis percentage depth doses in a slab phantom. All curves are normalized with D_{max}=100%. Results are reported in each slab. Note that the results in Tissue 1 are reported at depths > 1 cm to exclude the high percentage differences in the buildup region.

	4x4 cm^2		10x10 cm^2		20x20 cm^2	
	All Depths		All Depths		All Depths	
AAA	Maximum Error (%)	RMS Error	Maximum Error (%)	RMS Error	Maximum Error (%)	RMS Error
Tissue 1	2.58	0.96	2.85	1.13	2.87	1.45
Bone	14.38	6.71	11.64	6.20	12.08	5.17
Lung	9.36	7.64	11.64	9.59	12.08	8.57
Tissue 2	14.38	6.54	10.30	4.40	10.27	2.90
AXB	Maximum Error (%)	RMS Error	Maximum Error (%)	RMS Error	Maximum Error (%)	RMS Error
Tissue 1	2.03	0.83	1.49	0.67	1.72	1.08
Bone	2.70	1.00	4.89	2.30	4.53	2.11
Lung	2.70	1.34	2.79	2.00	3.84	2.40
Tissue 2	2.36	0.68	4.89	2.51	4.53	2.07
COMET(515151)	Maximum Error (%)	RMS Error	Maximum Error (%)	RMS Error	Maximum Error (%)	RMS Error
Tissue 1	3.28	1.60	2.56	1.93	3.76	1.62
Bone	3.58	1.90	3.87	1.20	3.77	1.56
Lung	3.58	2.84	1.72	0.79	3.30	1.82
Tissue 2	2.28	1.48	2.72	1.10	3.77	1.49

Table 21: Slab phantom profile error at depth of 1.5, 10 and 20 cm^2. Results are reported for the central 80% and 80-120% of the field size.

	4x4 cm^2		10x10 cm^2		20x20 cm^2	
d=1.5 cm	Central 80%		Central 80%		Central 80%	
	Maximum Error (%)	RMS Error	Maximum Error (%)	RMS Error	Maximum Error (%)	RMS Error
AAA	0.75	0.41	1.23	0.52	2.82	1.21
AXB	1.35	0.49	1.63	0.74	2.23	0.91
COMET(515151)	1.47	0.61	0.92	0.54	3.42	1.44
	80-120%		80-120%		80-120%	
	Maximum Error (%)	RMS Error	Maximum Error (%)	RMS Error	Maximum Error (%)	RMS Error
AAA	49.13	25.37	19.75	10.34	19.58	7.17
AXB	49.13	17.97	28.33	16.25	19.48	6.71
COMET(515151)	27.38	15.55	42.44	23.74	42.30	23.47
d=10 cm	Central 80%		Central 80%		Central 80%	
	Maximum Error (%)	RMS Error	Maximum Error (%)	RMS Error	Maximum Error (%)	RMS Error
AAA	9.22	7.82	11.80	10.86	11.95	10.37
AXB	4.71	1.81	3.25	2.26	3.93	2.31
COMET(515151)	4.26	2.66	3.55	2.22	3.44	1.51
	80-120%		80-120%		80-120%	
	Maximum Error (%)	RMS Error	Maximum Error (%)	RMS Error	Maximum Error (%)	RMS Error
AAA	29.00	15.47	23.82	15.12	28.66	16.27
AXB	29.00	5.90	22.65	4.61	28.43	5.88
COMET(515151)	9.65	5.93	15.94	5.66	22.52	9.32
d=20 cm	Central 80%		Central 80%		Central 80%	
	Maximum Error (%)	RMS Error	Maximum Error (%)	RMS Error	Maximum Error (%)	RMS Error
AAA	8.02	7.22	5.84	4.59	3.33	1.88
AXB	2.10	1.27	3.78	2.84	3.08	1.65
COMET(515151)	2.79	2.46	1.66	1.41	2.91	1.06
	80-120%		80-120%		80-120%	
	Maximum Error (%)	RMS Error	Maximum Error (%)	RMS Error	Maximum Error (%)	RMS Error
AAA	40.02	15.25	34.06	11.41	22.68	6.36
AXB	40.02	13.81	34.06	8.98	21.64	6.04
COMET(515151)	5.60	3.74	23.07	8.40	26.65	6.70

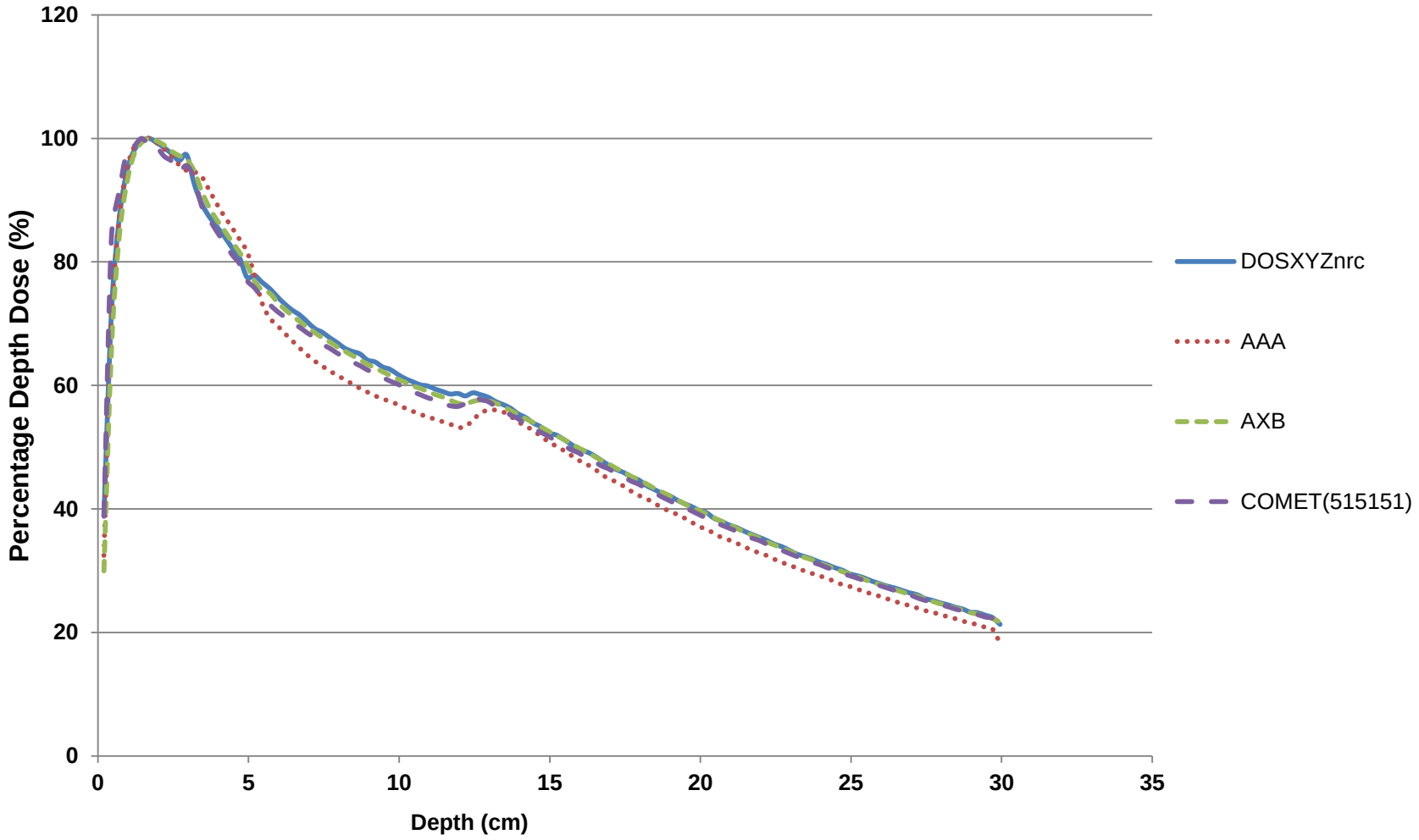

Figure 49: Slab phantom percentage depth dose with a field size of 4x4 cm^2

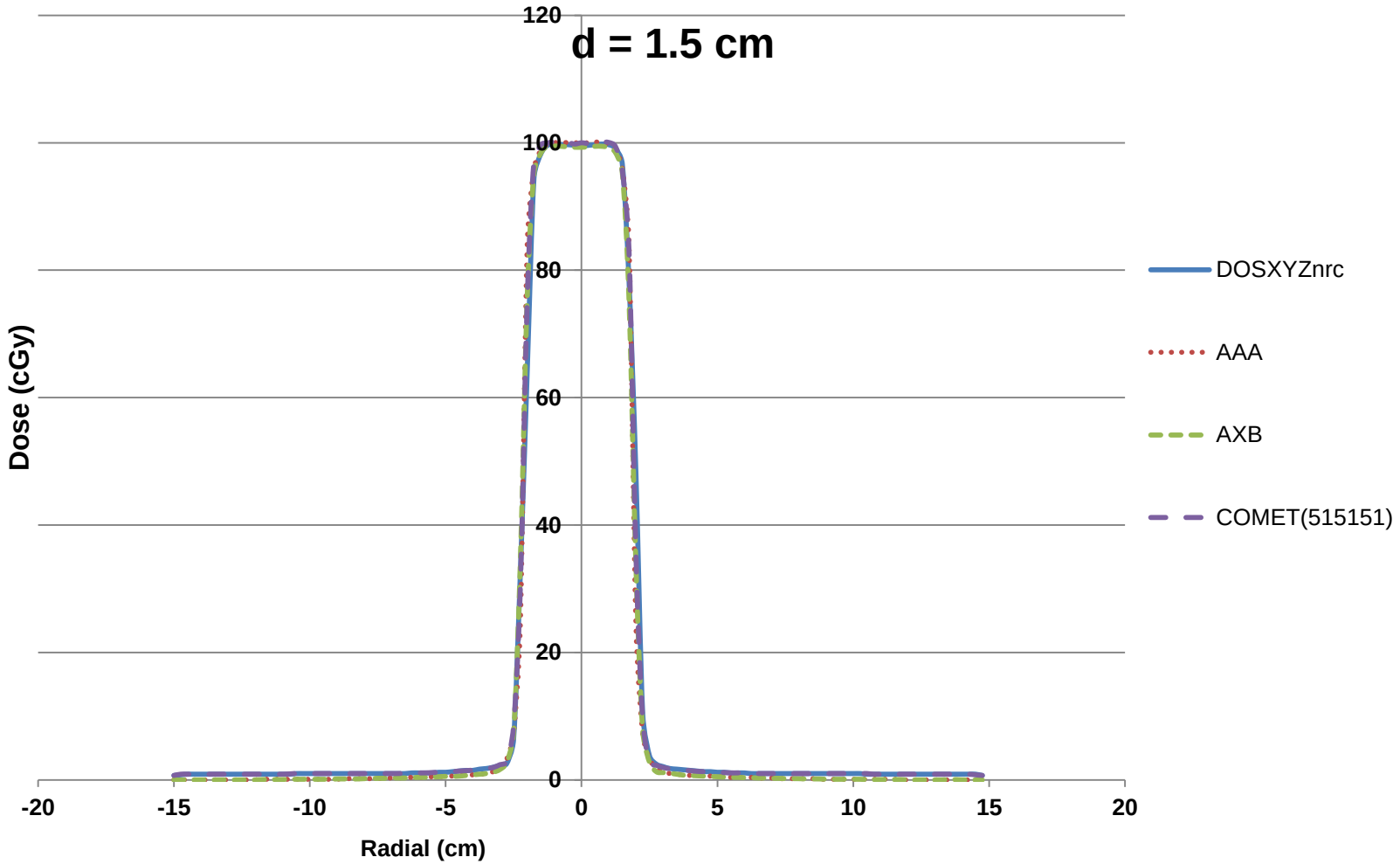

Figure 50: Slab phantom profile at a depth of 1.5 cm with a 4x4 cm^2 field size

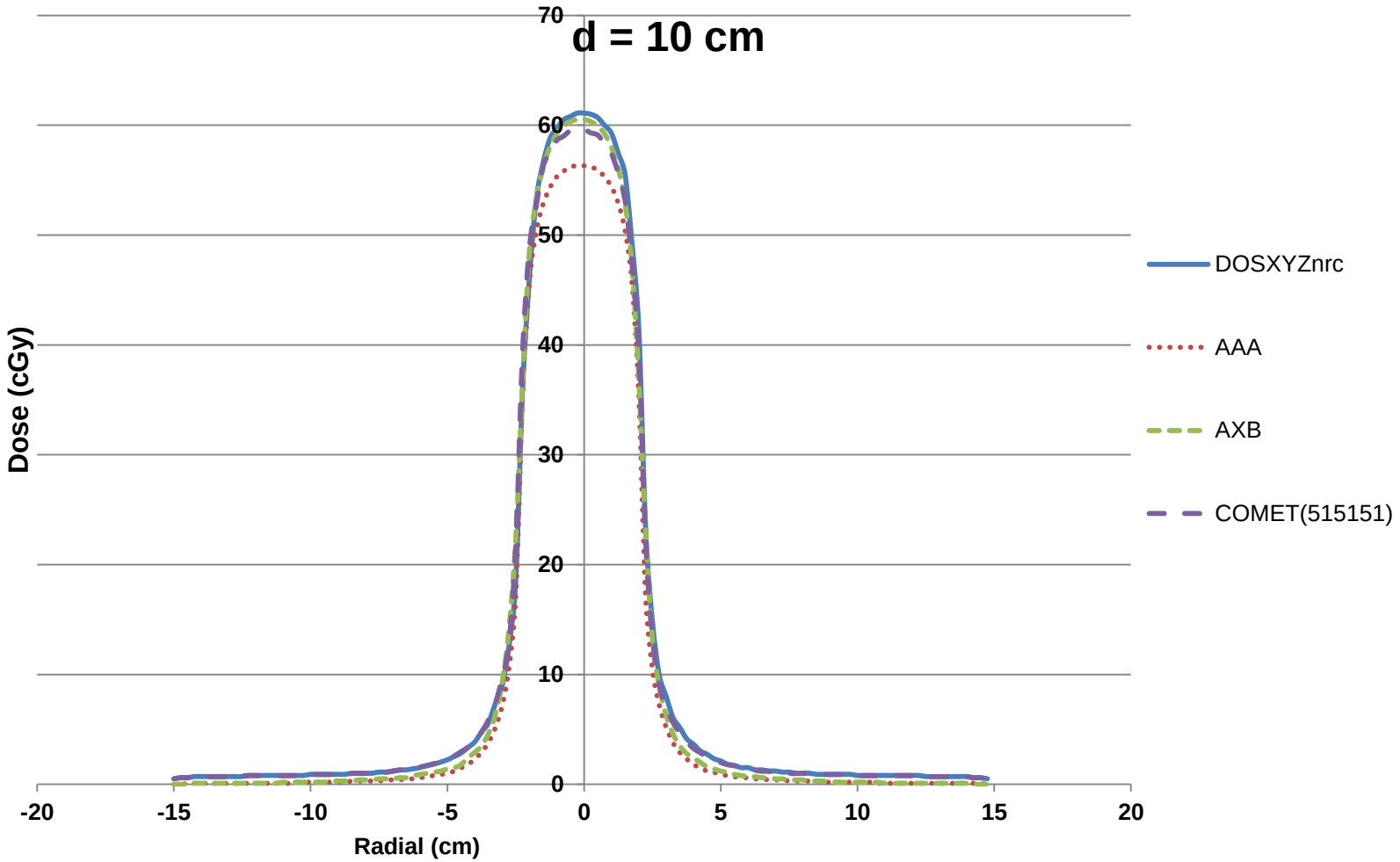

Figure 51: Slab phantom profile at a depth of 10 cm with a 4x4 cm^2 field size

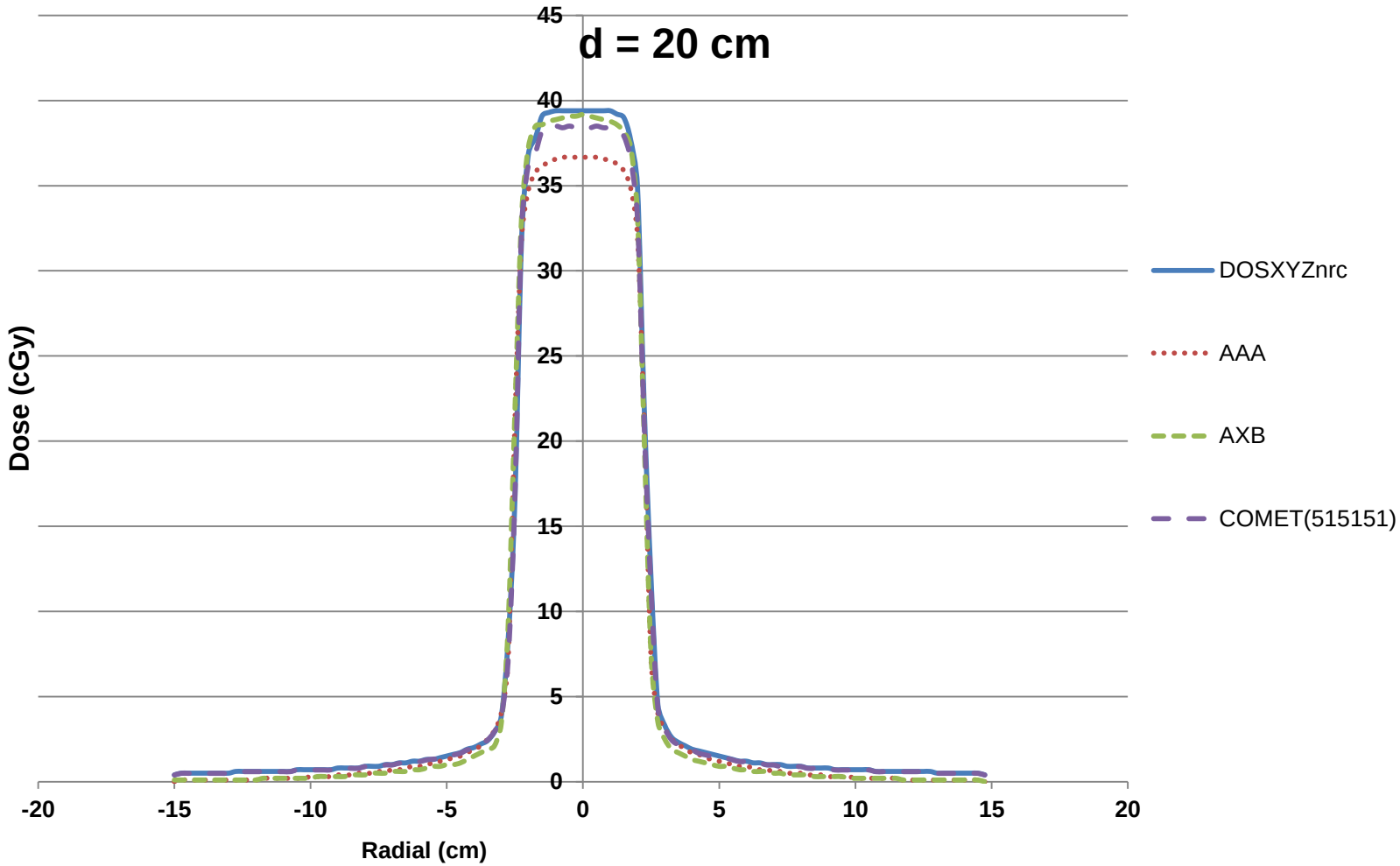

Figure 52: Slab phantom profile at a depth of 20 cm with a 4x4 cm^2 field size

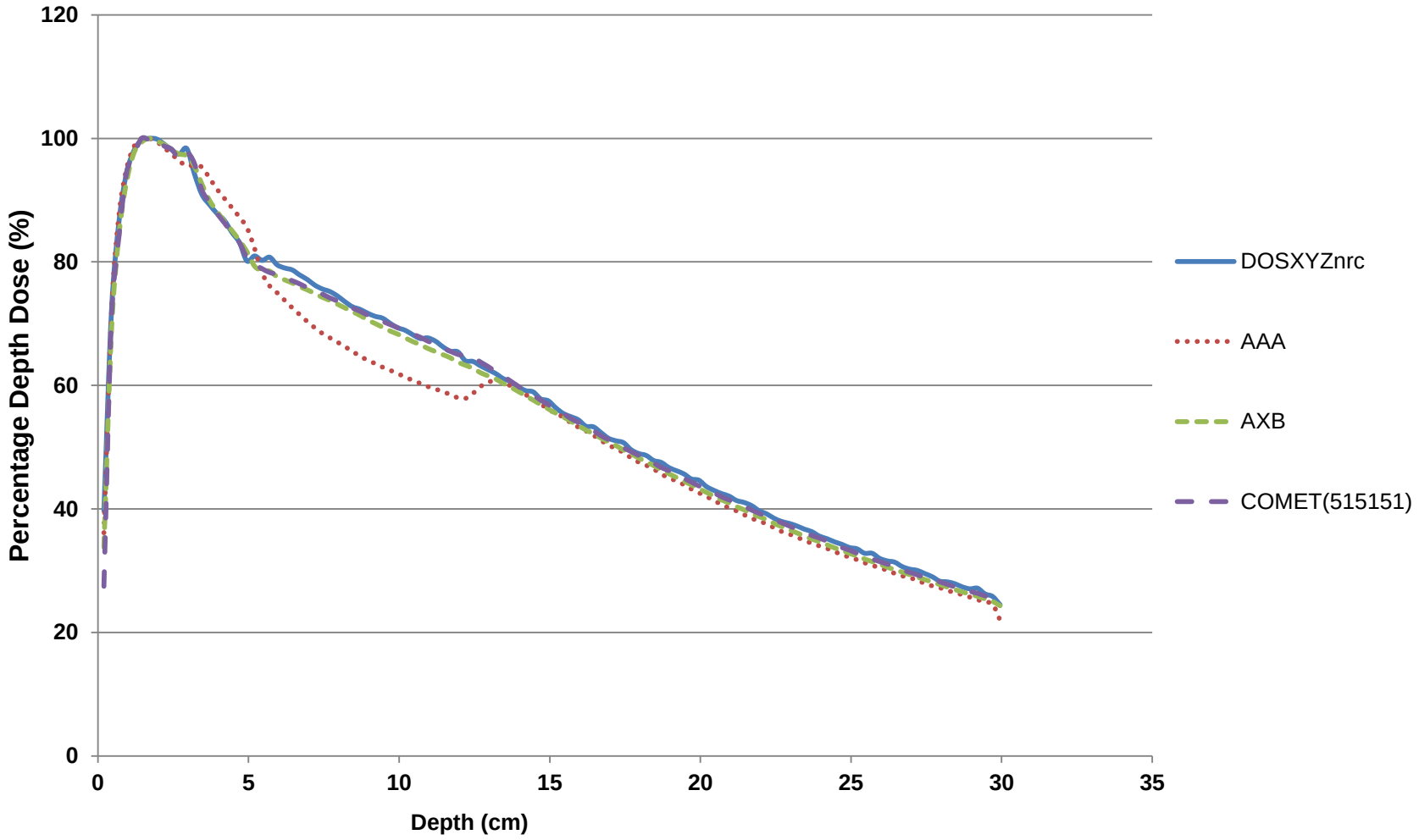

Figure 53: Slab phantom percentage depth dose with a field size of 10x10 cm^2

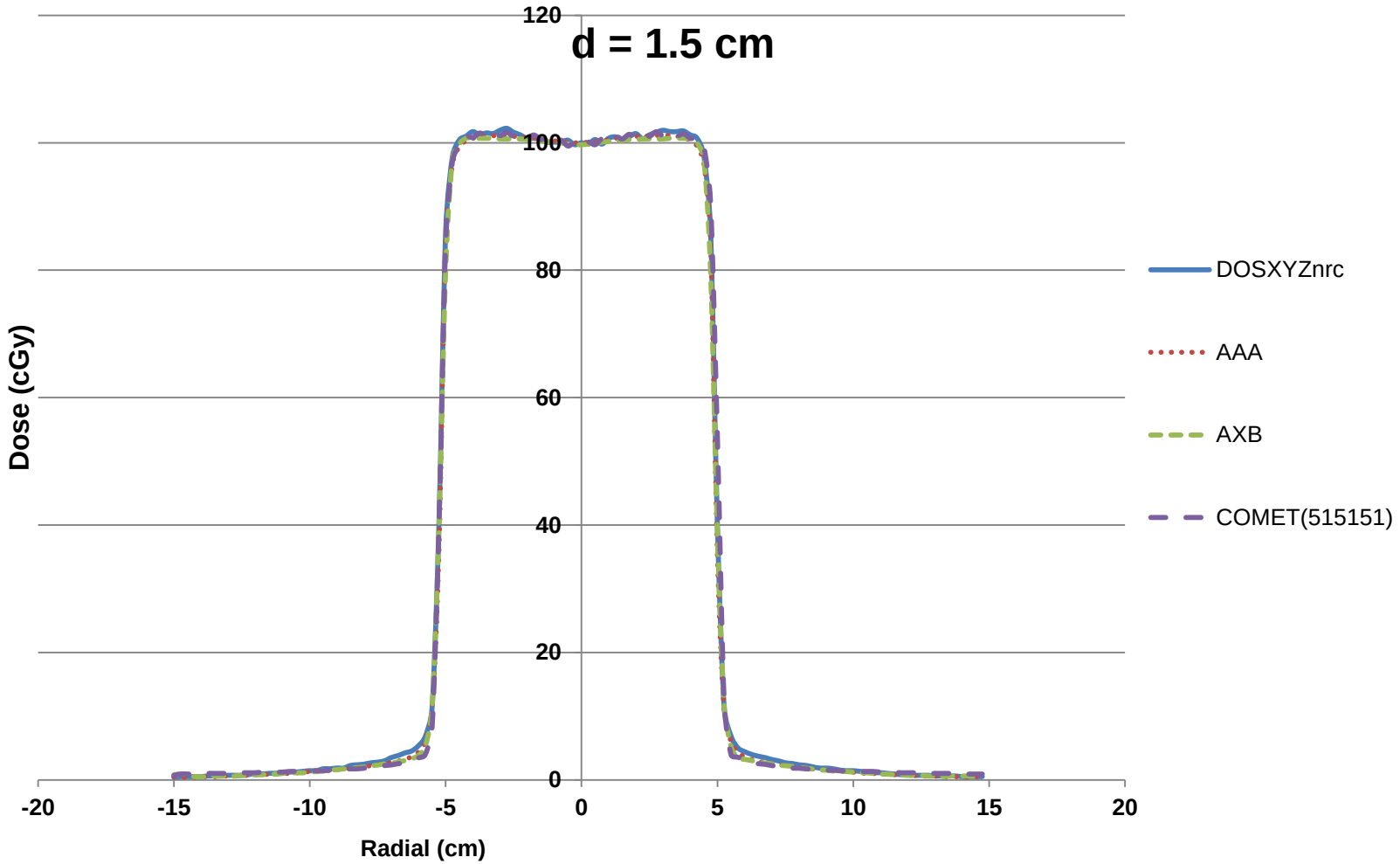

Figure 54: Slab phantom profile at a depth of 1.5 cm with a 10x10 cm^2 field size

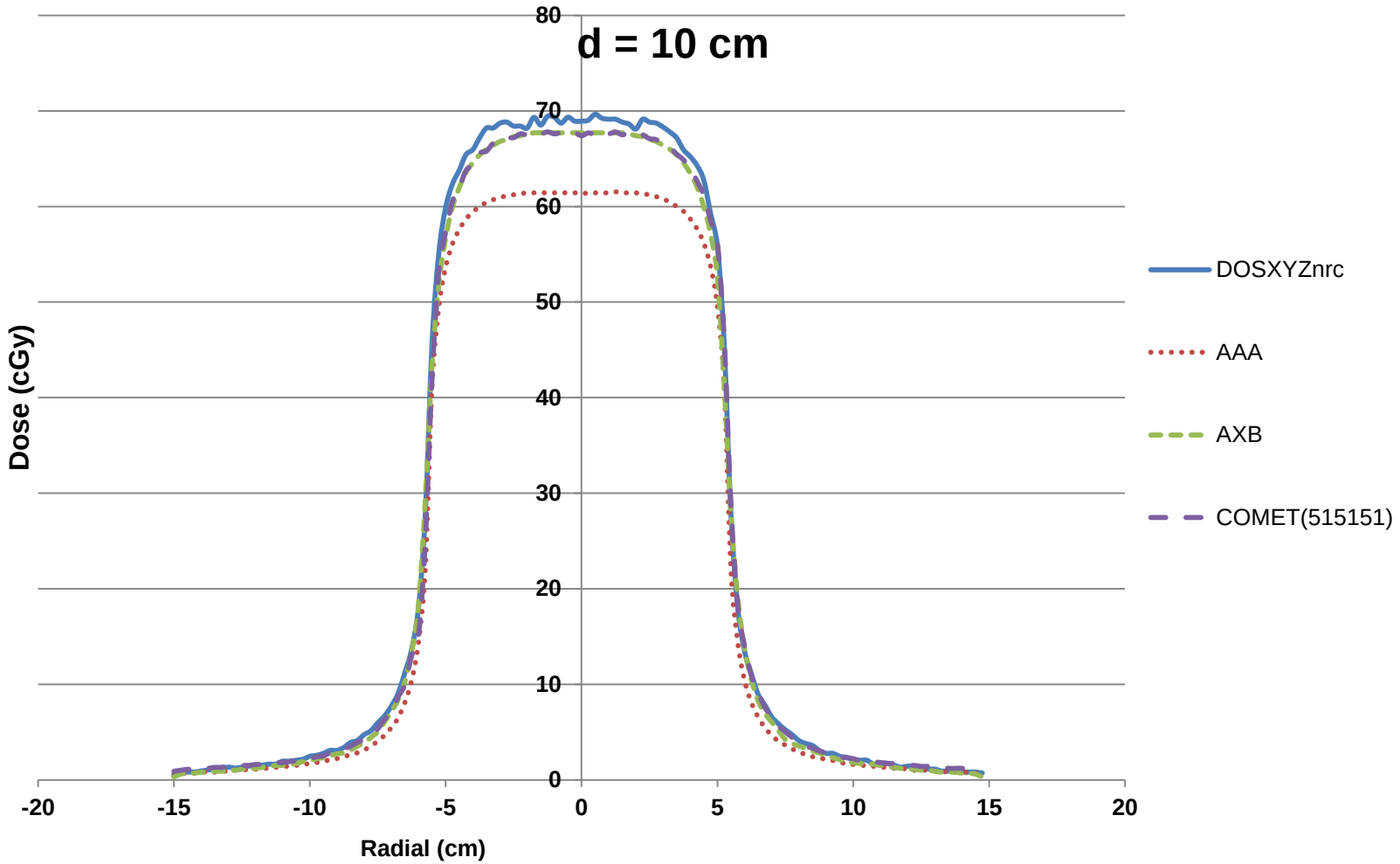

Figure 55: Slab phantom profile at a depth of 10 cm with a 10x10 cm^2 field size

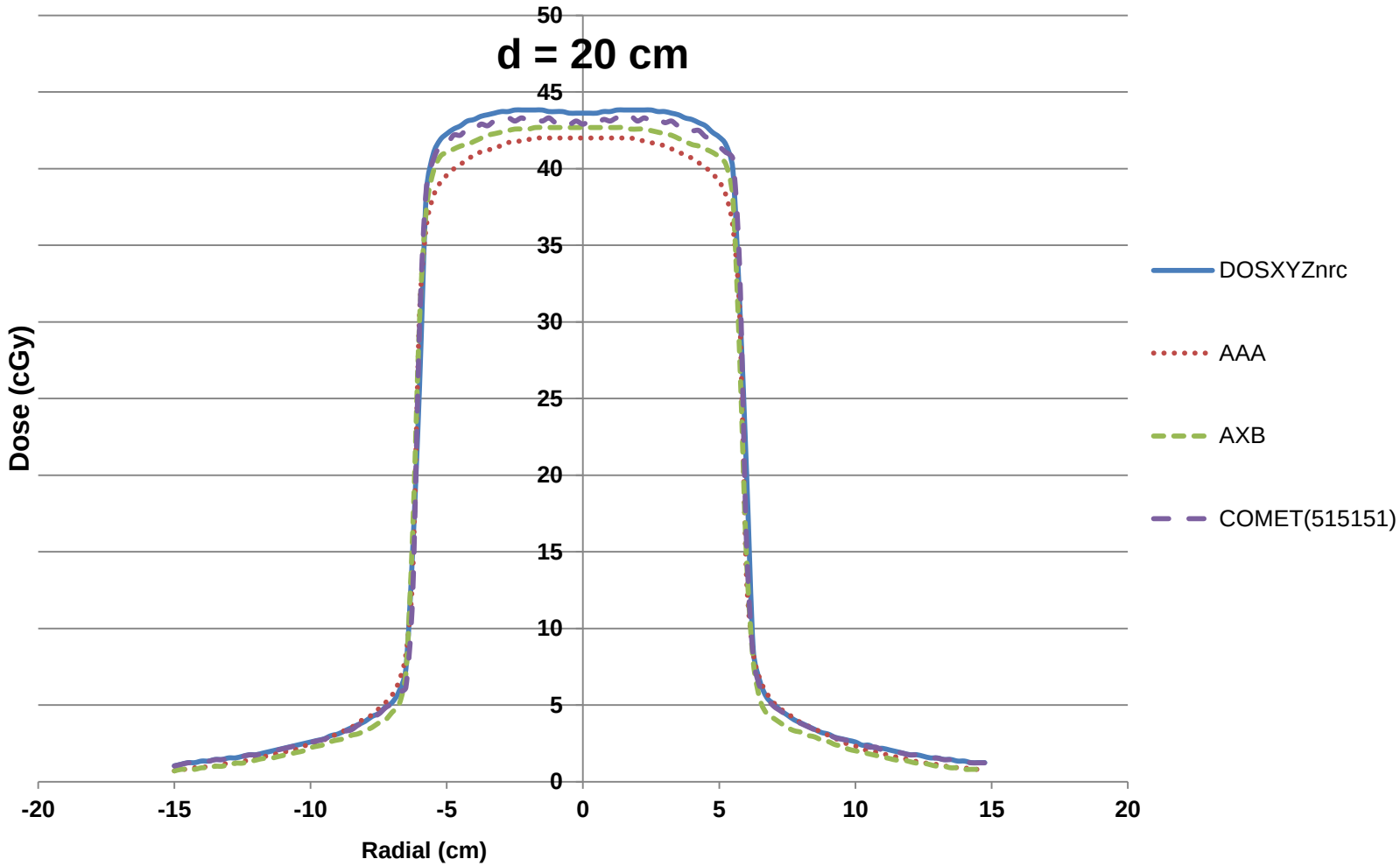

Figure 56: Slab phantom profile at a depth of 20 cm with a 10x10 cm^2 field size

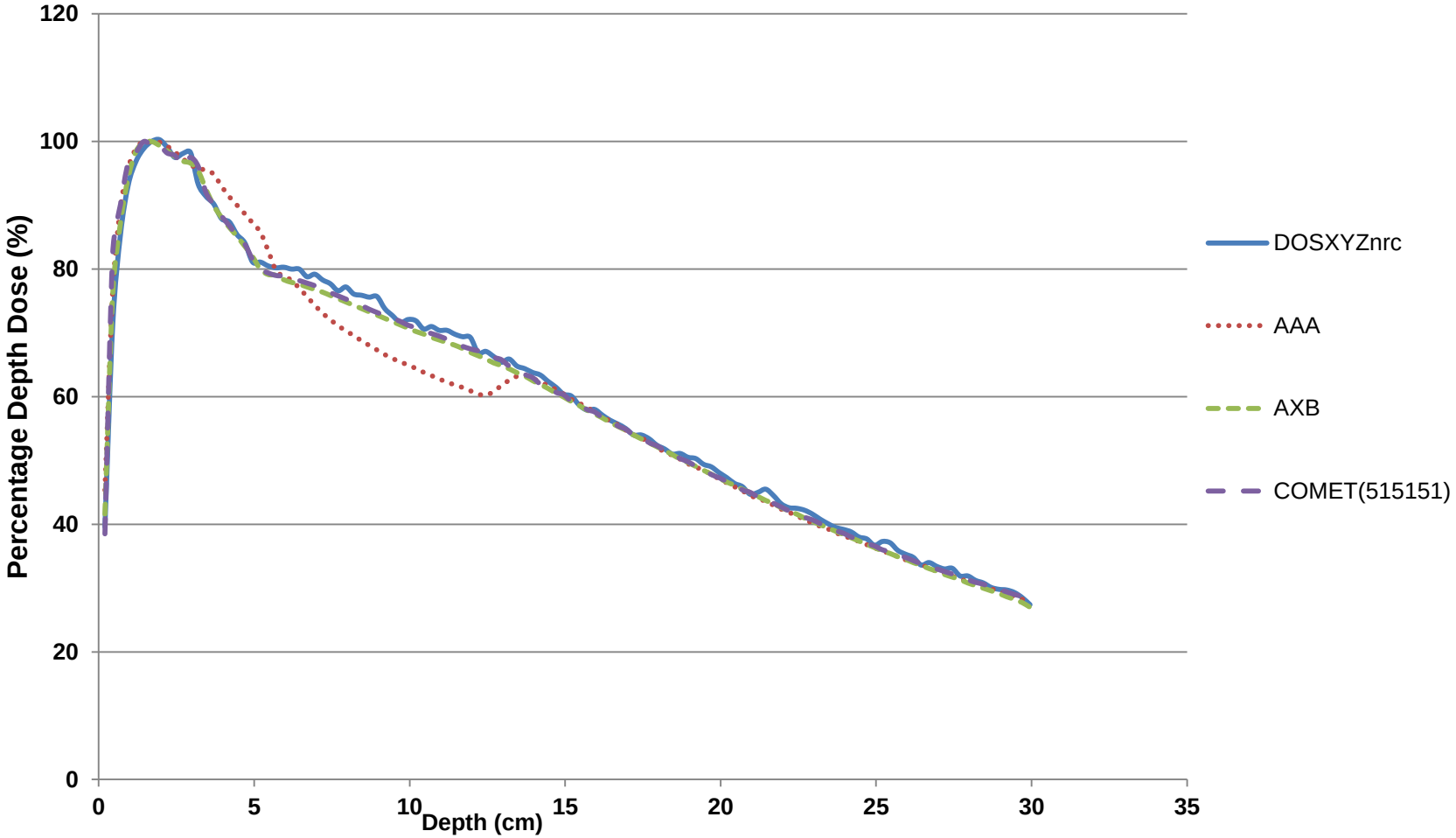

Figure 57: Slab phantom percentage depth dose with a field size of 20x20 cm

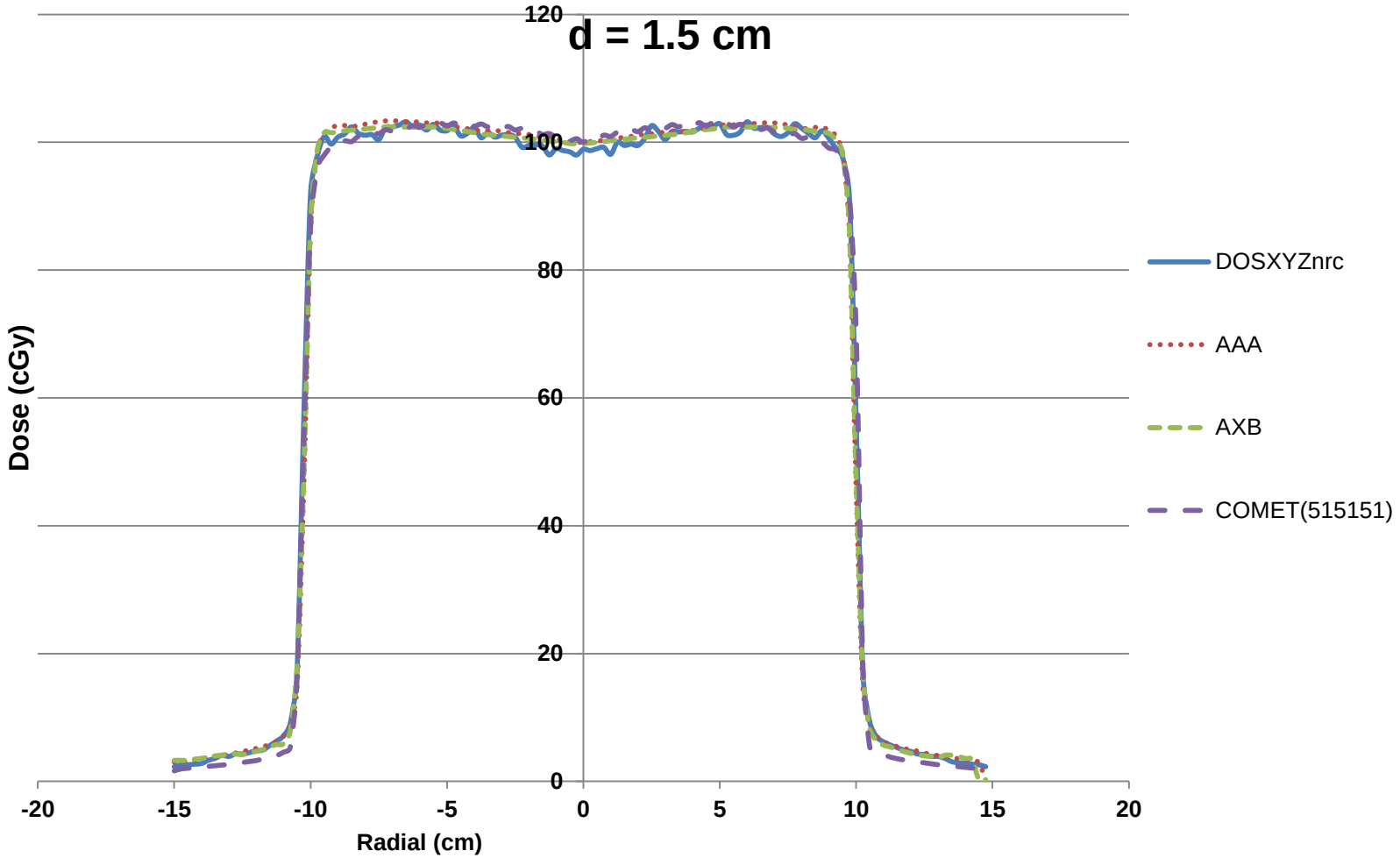

Figure 58: Slab phantom profile at a depth of 1.5 cm with a 20x20 cm^2 field size

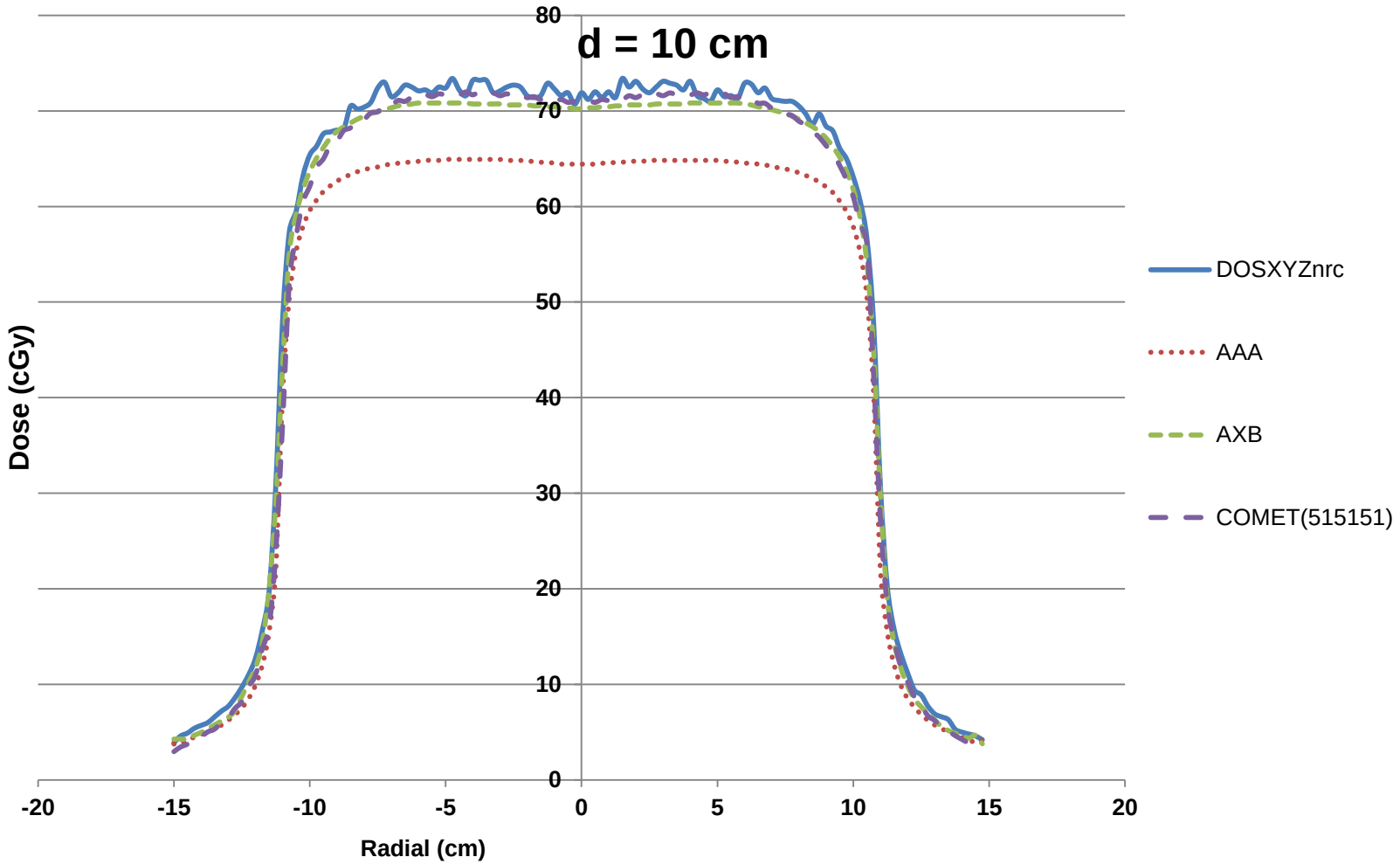

Figure 59: Slab phantom profile at a depth of 10 cm with a 20x20 cm^2 field size

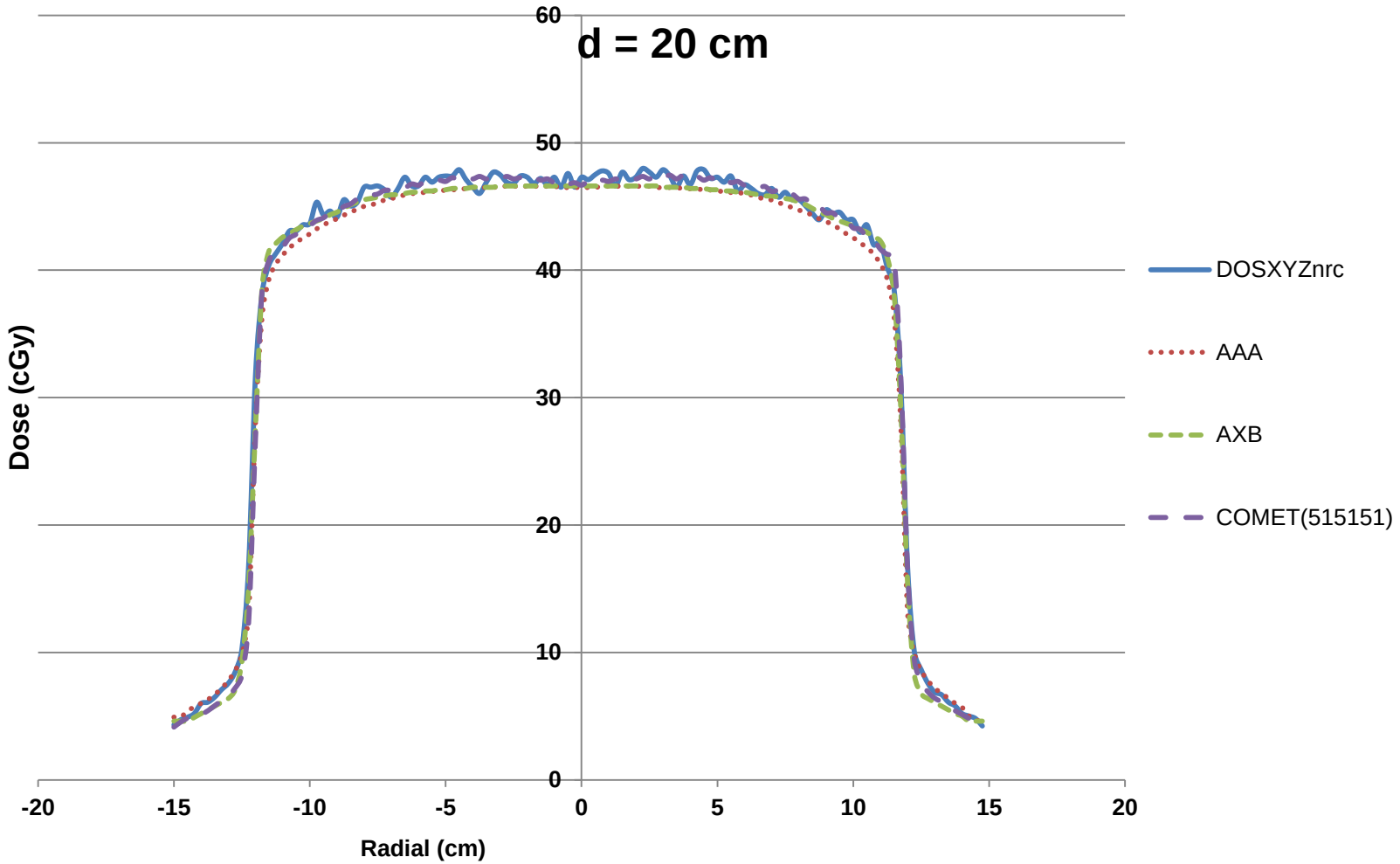

Figure 60: Slab phantom profile at a depth of 20 cm with a 20x20 cm^2 field size

7.6.2 Gamma Evaluation

The gamma evaluation of the slab phantom results are summarized in Table 22 and shown in Figures 61, 62, and 63. COMET had the highest percentage of pixels with a passing score with the 10x10 cm^2 and 20x20 cm^2 field size and AXB had the highest percentage of pixels passing with the 4x4 cm^2 field size. This is due mainly to COMET underestimating the dose in the lung region for this field size. The effect can be seen along the central axis percentage depth dose in Figure 49. The smaller field size calculations are greatly affected by how well the field edge is modeled. If the field size is slightly increased more lateral scatter adds dose to the central region of the field.

Table 22: Gamma Scores for Slab Phantom

Field Size	4x4 cm^2	10x10 cm^2	20x20 cm^2
	$\Gamma < 1$ (%)	$\Gamma < 1$ (%)	$\Gamma < 1$ (%)
AAA	36.26	58.43	56.69
AXB	81.78	81.50	72.62
COMET(515151)	77.40	82.09	79.03

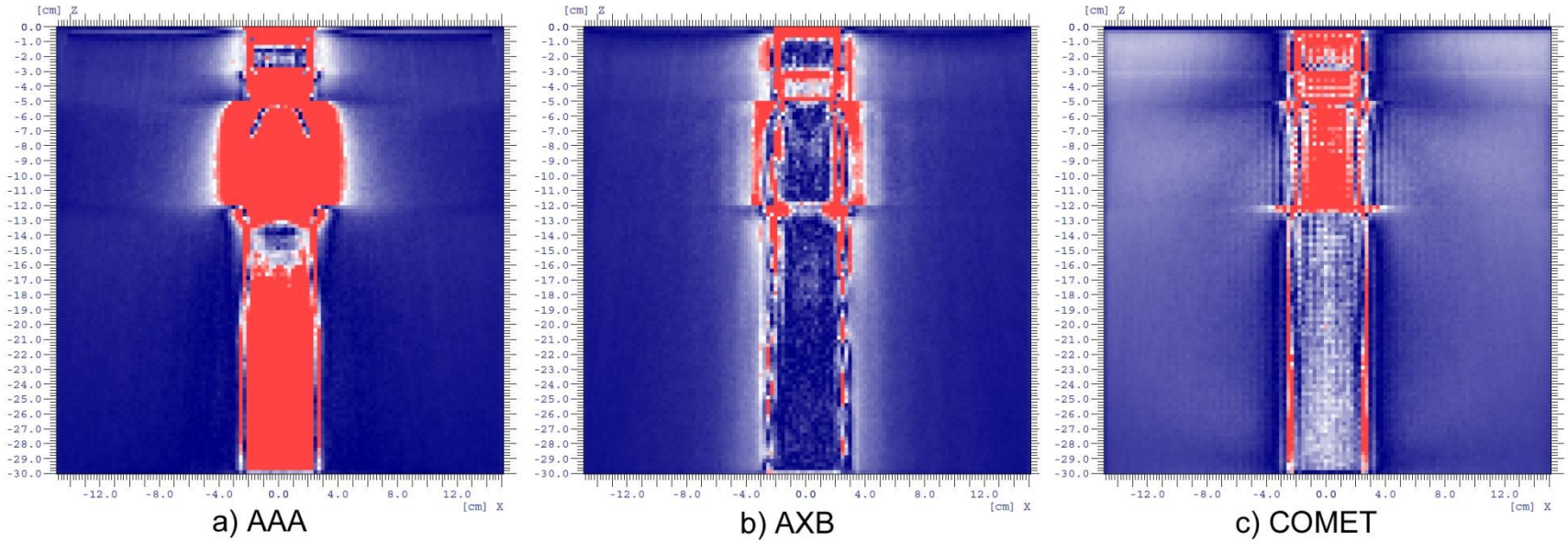

Figure 61: Gamma results in slab phantom 4x4 cm^2

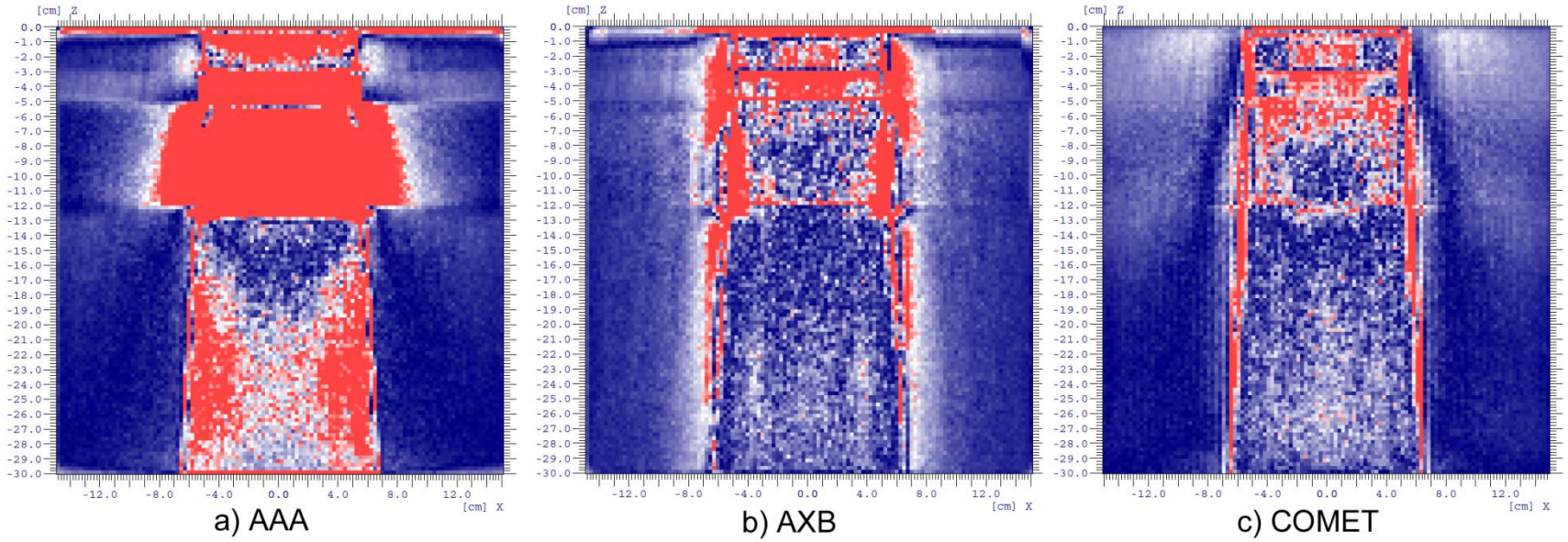

Figure 62: Gamma results in slab phantom 10x10 cm^2

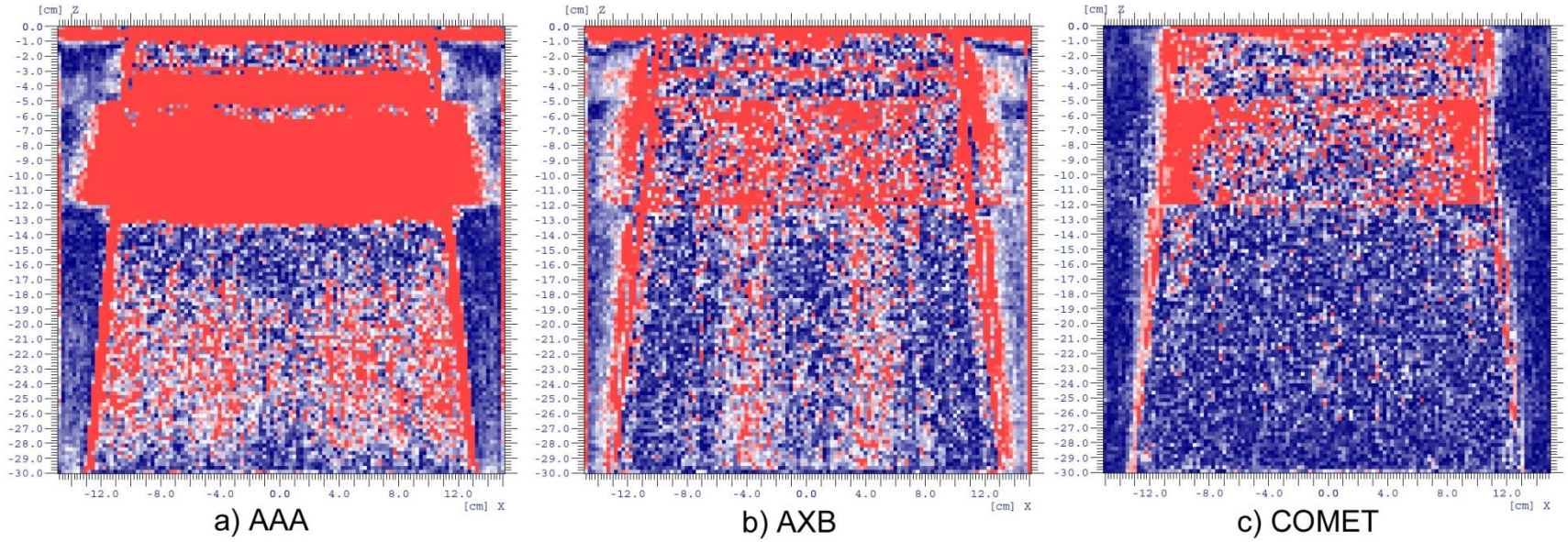

Figure 63: Gamma results in slab phantom 20x20 cm^2

7.7 Sensitivity Study

The influence of selecting various values for the expansion orders with regard to the response functions was investigated. To that end five calculations were performed and compared to the reference Monte Carlo calculation using the gamma method with a 1%/1mm DTA. To reduce the calculation time, calculations were performed with a 10x10 cm^2 field size in a 15x15x30 cm^3 slab phantom with the same material composition as the slab phantom previously described. The region of interest was set at the borders of the phantom. All calculations were performed on 10 processors. Figure 64 shows the results. The results are summarized in Table 23.

Table 23: Gamma comparison of COMET results for 10x10 cm^2 field size and various expansion orders in the response functions

	Γ < 1 (%)	Calculation Time (h)
COMET(313131)	51.48	1.52
COMET(323232)	54.14	5.38
COMET(515151)	76.70	3.00
COMET(525252)	76.70	7.35
COMET(717171)	80.78	5.93
COMET(727272)	80.84	13.56

These results indicate that the increase in angular expansion order has a much greater impact on the final results than the spatial expansion order. The increase in spatial expansion order also dramatically increases the calculation time with little or no improvement in percentage of pixels passing the gamma tests. Expansion orders (515151) were adopted for general use in this work as they generated results with good agreement with the reference solution and an acceptable calculation time.

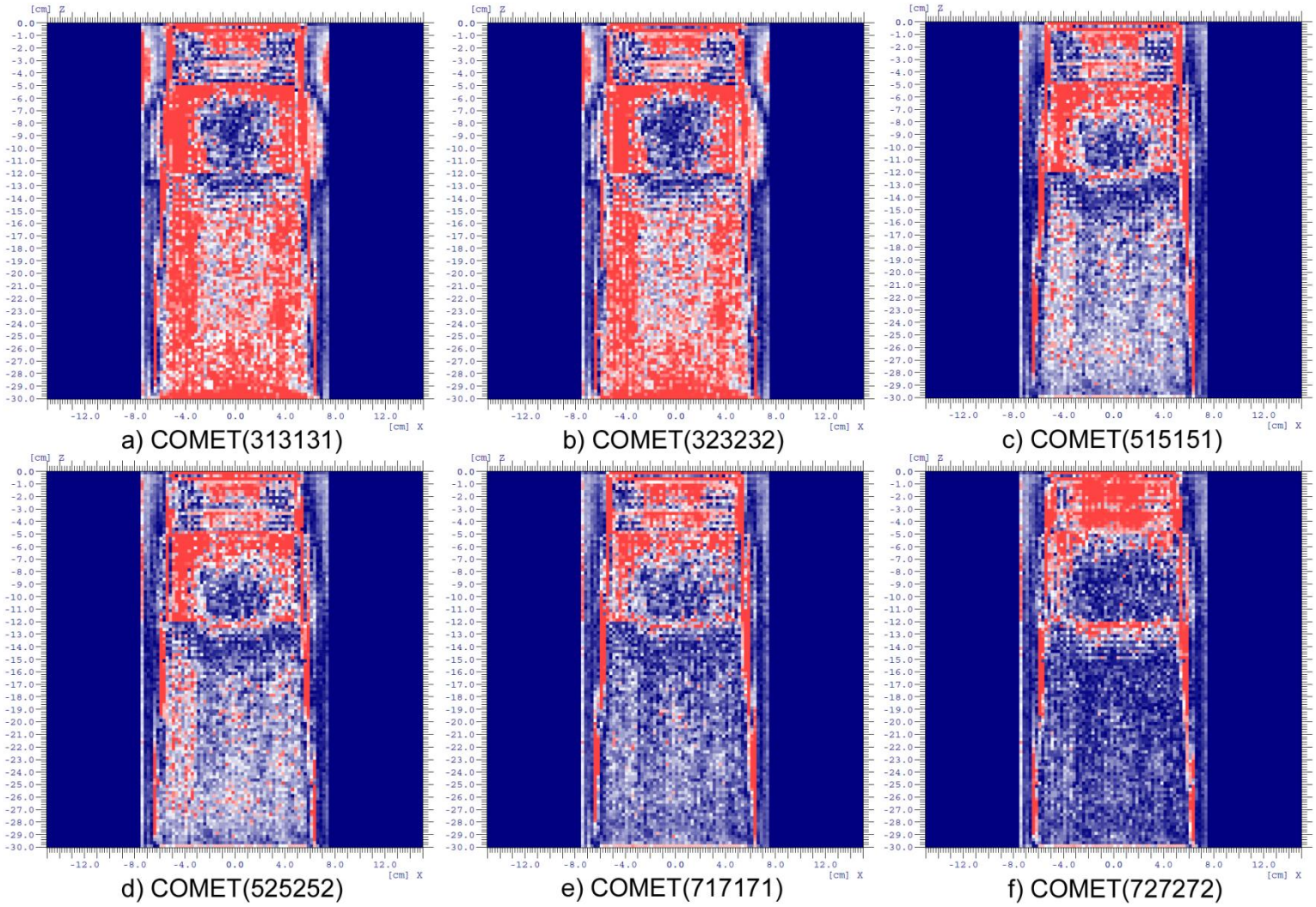

Figure 64: Gamma results for 10x10 cm^2 field size with various spatial and angular expansion orders set in COMET

7.8 Calculation Times

Calculations with DOSXYZnrc and COMET were performed on a Linux cluster with 4 nodes each with 31 GB of memory and 12 six-core AMD Opteron 2427s clocked at 2.2 GHz. Due to availability on the cluster, computations were performed with 10 and 30 processors. The AAA and AXB calculations were performed on a Dell Optiplex 755 computer (Dell Inc., Round Rock, TX) with an Intel Core 2 Duo CPU at 2.33GHz and 8.00 GB of RAM.

Table 24 compares calculation times necessary for calculations of the water and slab phantoms. The calculations performed with AAA and AXB were dramatically faster than those with DOSXYZnrc or COMET. It is instructive to consider that COMET treats the voxels inside the treatment field equally to those outside the treatment field. The treatment time for the same response function expansion coefficients and 10x10 cm^2 field size reported in section 7.7 was 2.21 hours as opposed to the 7.42 hours reported in this section. The difference is that the lateral phantom dimensions were reduced from 30 cm to 15 cm for section 7.7 indicating that a significant reduction in the calculation time of COMET can be achieved by treating low dose regions outside the field with less mathematical rigor.

COMET was faster than the DOSXYZnrc calculations by factors ranging from 2.87 to 12.15. COMET computations were performed using more than 10 processors but this did not result in decreased calculation times.

Table 24: Calculation times for water and slab phantom

Water Phantom

	Time (h:m:s)			Processors		
	4x4 cm^2	10x10 cm^2	20x20 cm^2	4x4 cm^2	10x10 cm^2	20x20 cm^2
DOSXYZnrc	21:20:47	101:17:50	101:19:48	10	30	30
AAA	0:00:11	0:00:15	0:00:22	1	1	1
AXB	0:00:26	0:01:03	0:02:19	1	1	1
COMET(515151)	6:36:45	7:03:56	9:10:42	10	10	10

Slab Phantom

	Time (h:m:s)			Processors		
	4x4 cm^2	10x10 cm^2	20x20 cm^2	4x4 cm^2	10x10 cm^2	20x20 cm^2
DOSXYZnrc	21:00:47	105:33:43	101:31:34	10	30	30
AAA	0:00:13	0:00:16	0:00:23	1	1	1
AXB	0:00:26	0:01:10	0:02:57	1	1	1
COMET(515151)	7:18:57	7:25:59	8:21:20	10	10	10

7.9 Lung Phantom

Figures 65-68 show the isodose plots of the axial, coronal, and sagittal slices for calculations performed with DOSXYZnrc, AAA, AXB, and COMET respectively. All calculations were performed with a 10x10 cm^2 6MV field centered on the mediastinal tumor. The field size is larger than necessary to treat the mass and would typically be collimated further using a block or multileaf collimator. Calculating a 10x10 cm^2 field through such a highly inhomogeneous region should illuminate any deficiencies in the calculation methods.

The isodose plots for DOSXYZnrc and COMET calculations were generated using the *dosxyz_show* utility provided in the DOSXYZnrc distribution. The AAA and AXB isodose plots were generated using the Eclipse treatment planning system. The immediate difference is that *dosxyz_show* does not smooth the isodose lines for display. A moderate smoothing would be desirable in the clinical setting but is not necessary for the analytical purposes of this work.

All three calculations produce isodose plots that are similar in shape to the DOSXYZnrc reference calculation. The most apparent differences on the axial slices occur in the tumor at the 60-70% isodose levels. AAA does not account for the tissue inhomogeneities as well as the other algorithms.

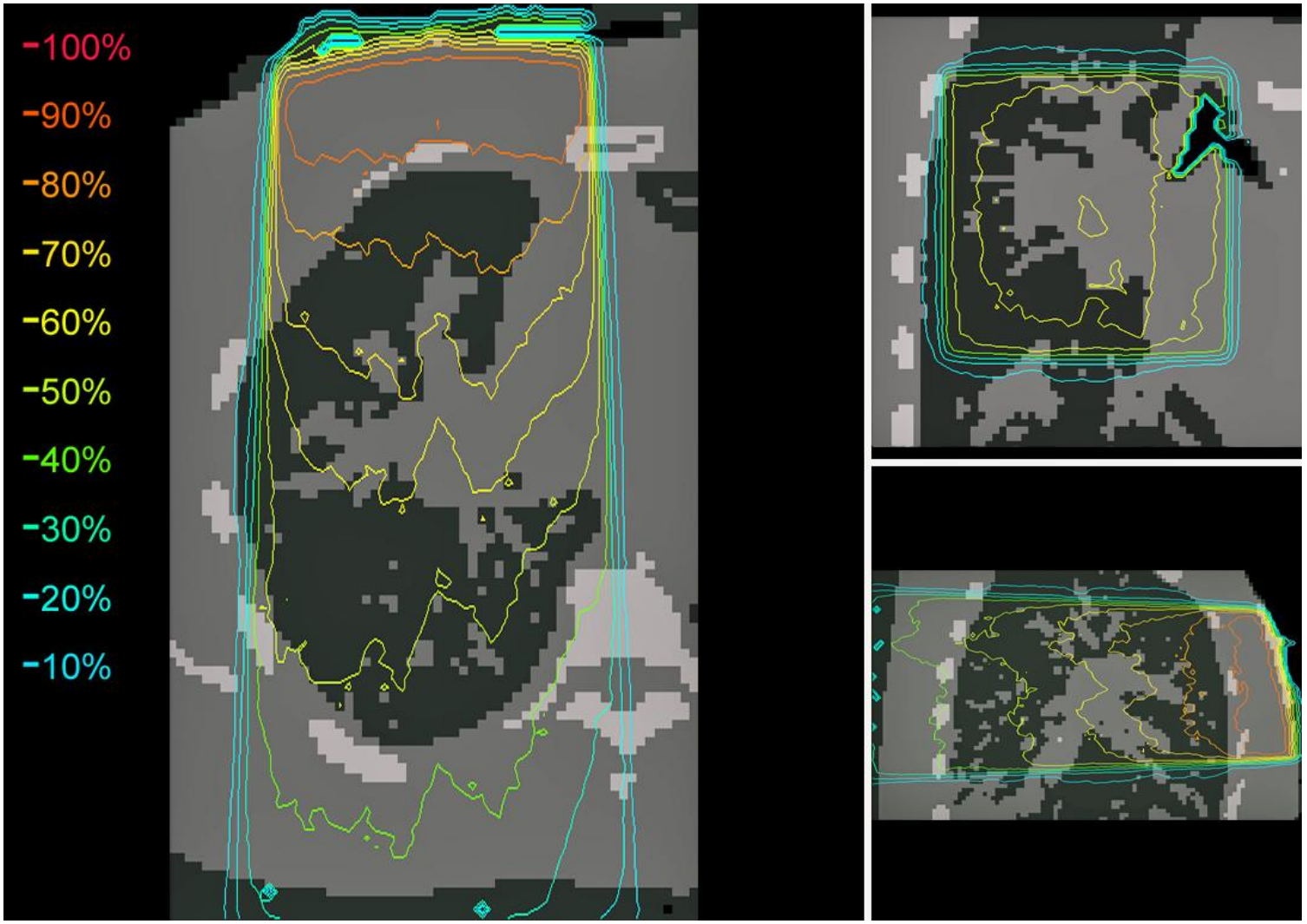

Figure 65: DOXYZnrc isodose plots for a 10x10 cm^2 field

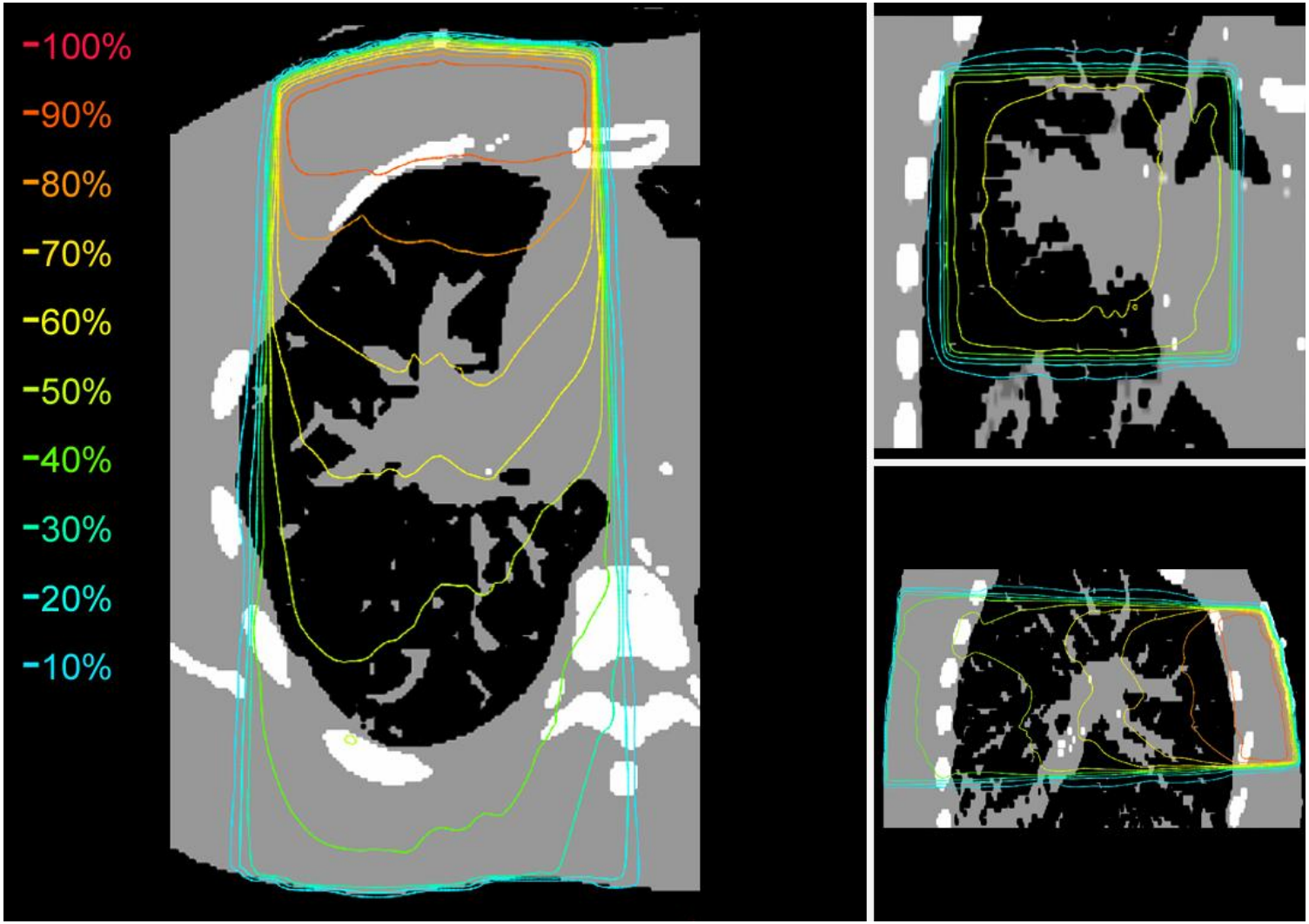

Figure 66: AAA isodose plots for a 10x10 cm^2 field

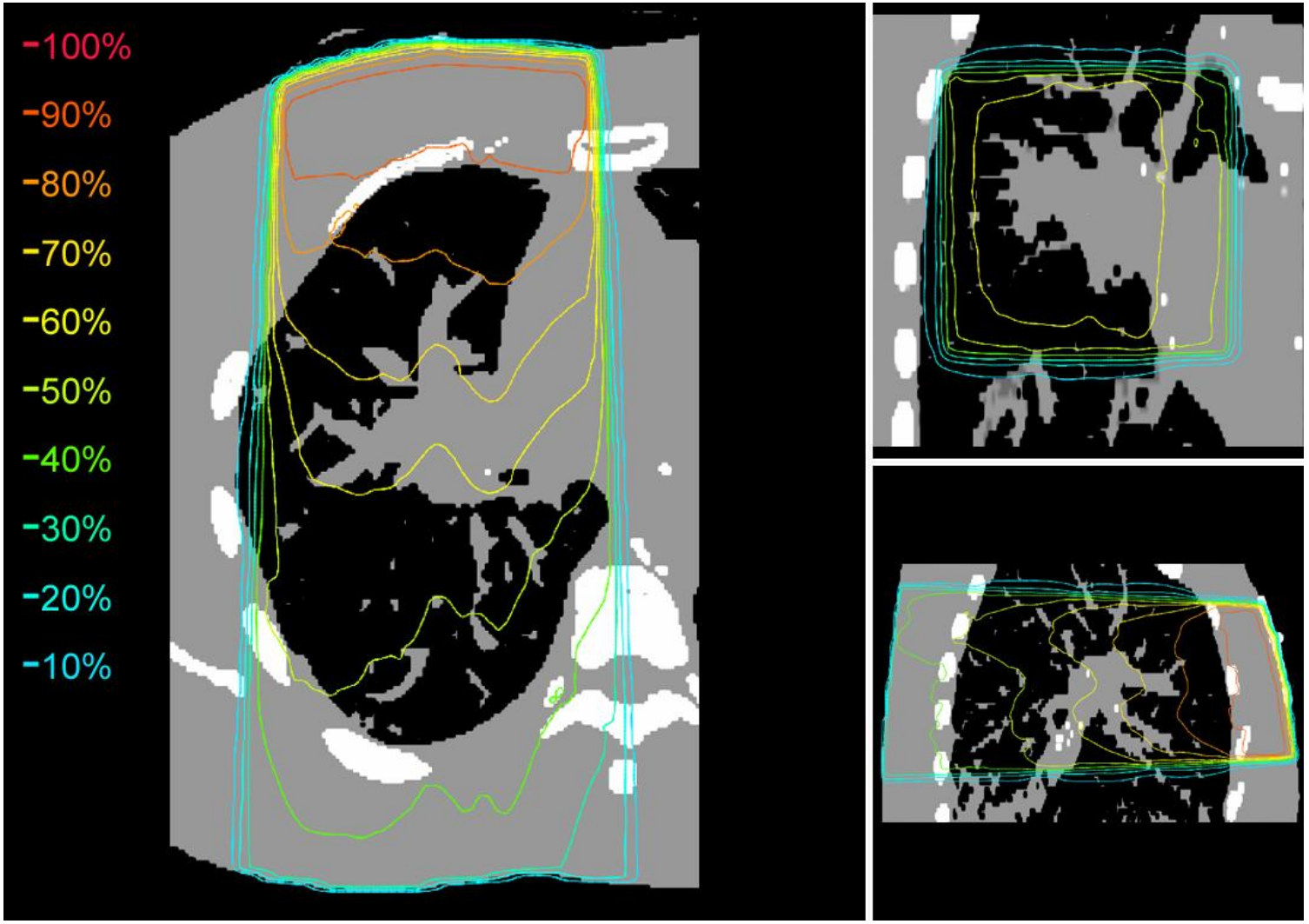

Figure 67: AcurosXB isodose plots for a 10x10 cm^2 field

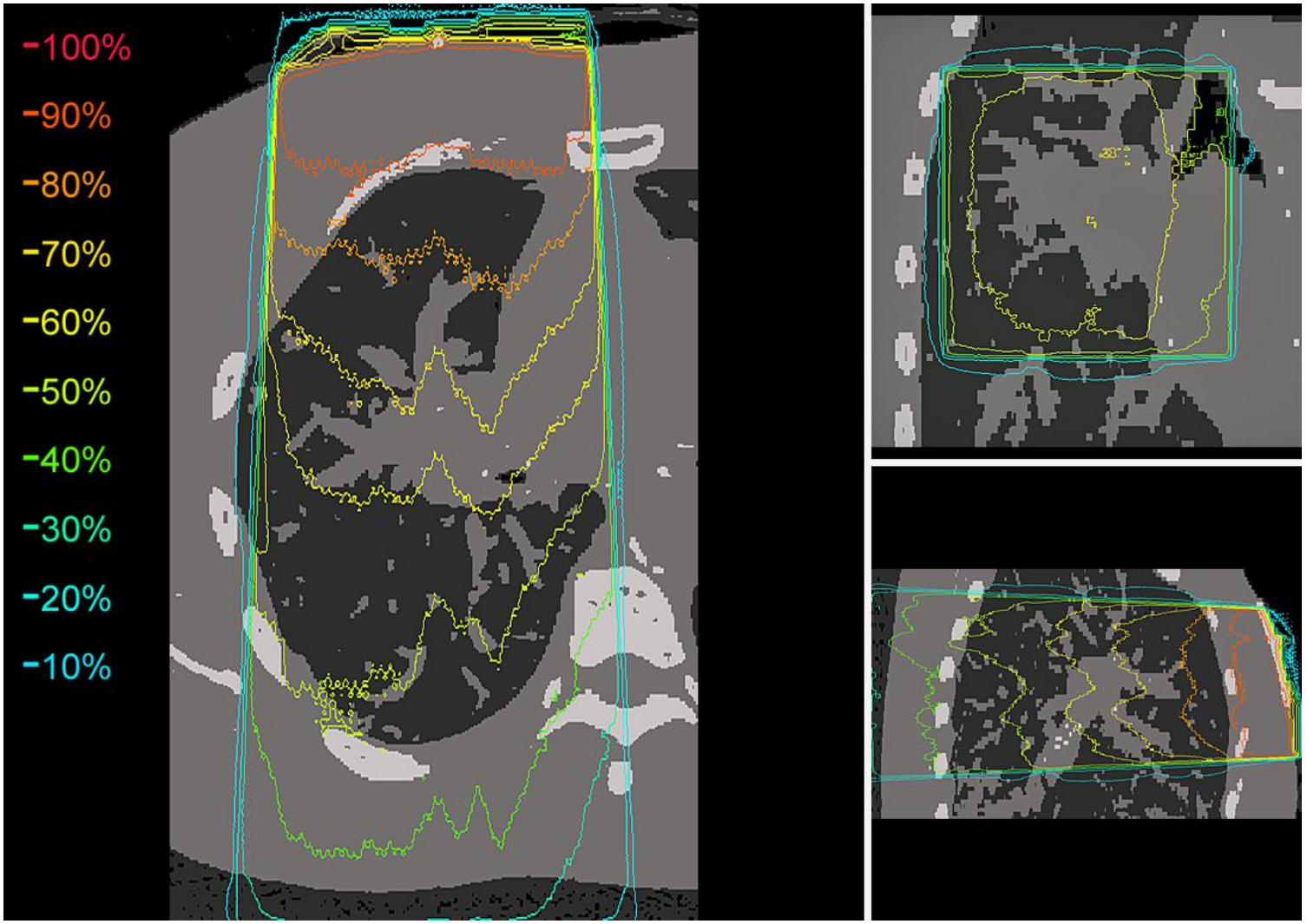

Figure 68: COMET isodose plots for a 10x10 cm^2 field

The gamma method was again used to compare the axial dose distributions when compared to a DOSXYZnrc reference calculation. The reference solution was calculated using $5x10^{11}$ histories and had an average percentage error of the 20 highest doses of 0.043%. The average percentage error of doses greater than half of the maximum dose was 0.061%.

For these tests a DTA criteria of 2%/2mm was chosen to better represent a gamma test that would be performed clinically. The region of interest used when calculating the percentage of pixels with a gamma score less than one was a rectangle set to extend 1 cm laterally beyond the field edge at the most posterior point in the patient and the anterior and posterior borders were set to the surface of the patient. This region of interest was chosen to exclude the regions of air outside the patient body contour because Eclipse excludes these regions from the final dose calculation. Figure 69 shows the results of the gamma analysis. AAA had the poorest performance with 56.3% of the pixels having a passing score of less than one. The AXB calculation resulted in 77.9% of the pixels passing and COMET produced 90.7%. The vertical line of failing pixels in the lung region of the AXB calculation is posterior to a rib along the anterior chest wall.

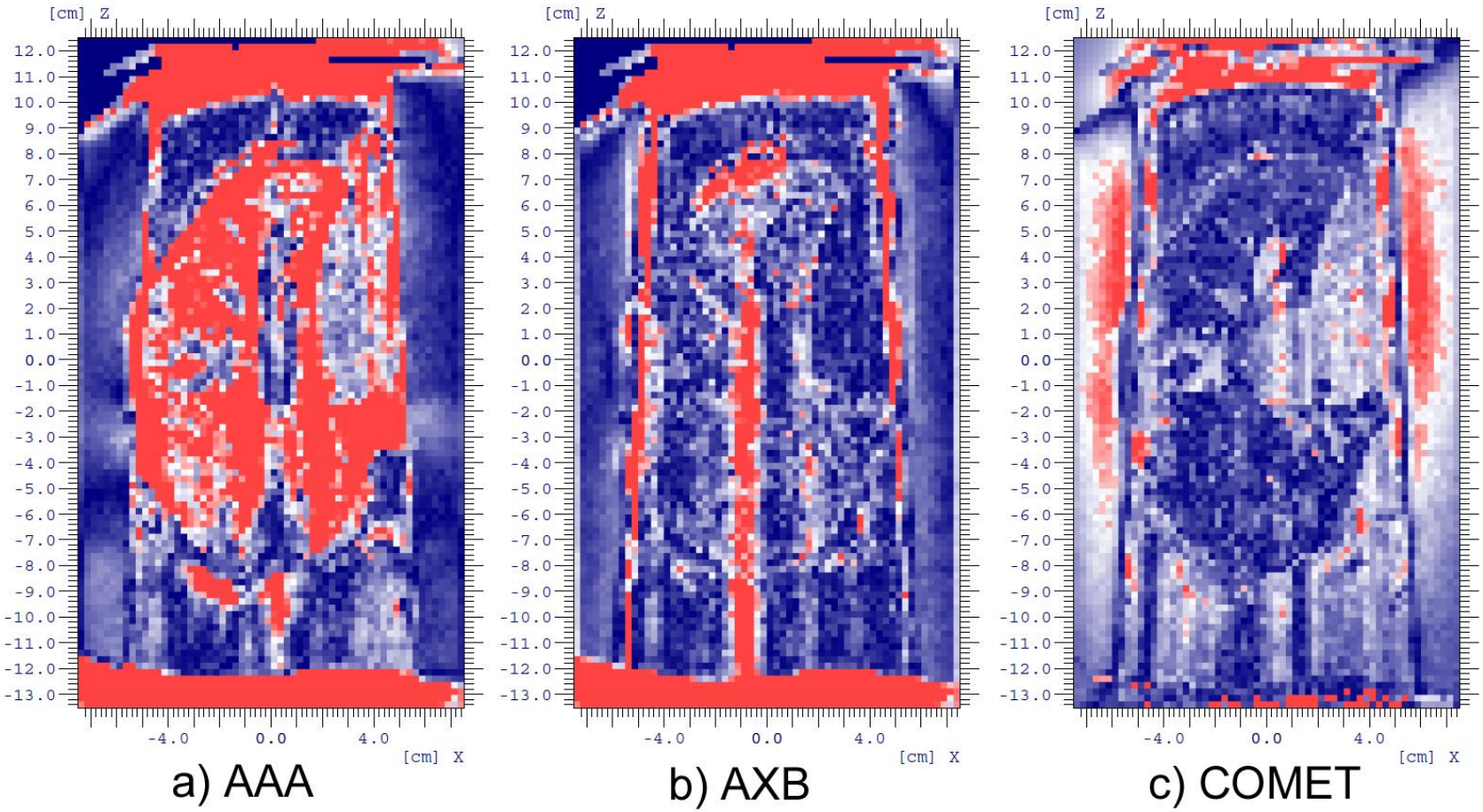

Figure 69: Gamma scores from lung phantom with 10x10 cm^2 field size and 2%/2mm DTA

CHAPTER 8

CONCLUSION

8.1 Discussion

8.1.1 Source Model

The source model developed in this work was formulated to represent the physical characteristics of the radiation emanating from the head of a linear particle accelerator used in the radiotherapeutic treatment of cancer patients. The model separated the source into primary photons, extra-focal photons, and electrons. Primary and extra-focal photon fluence was modeled using the functional expansion tally method and reference phase space data to produce functional approximations of the fluence at the energy levels determined by the energy spectrum discretization. The energy spectrum was taken from the BEAM user code for a 6 MV photon beam produced on a 2100C Varian clinac and discretized into 14 bins. Electron contamination was modeled using an exponential decay equation that was manually optimized to match Monte Carlo generated reference results.

The results of tests performed to evaluate the statistical and truncation error associate with the functional expansion tally method strongly suggested that an expansion used to model linac photon fluence should use a zonal harmonic hemispherical harmonic basis. This approach adopts the assumption of azimuthal symmetry in the clinical radiation beam. The azimuthal symmetry assumption is commonly used in beam modeling.

Plots of the functional approximations of the primary and extra-focal fluence were instructive in selecting a starting point for the expansion order. The influence of the flattening filter could clearly be seen using a zonal harmonic basis in expansion orders as low as $l = 15$. Tests were performed to evaluate the optimal expansion order necessary to produce a high level of agreement between COMET and DOSXYZnrc dose calculations. An optimal expansion order of $l = 25$ was ultimately selected.

While the proposed source model was implemented in COMET for this work, the method could easily be implemented in other treatment planning algorithms. The number of expansion coefficients using a zonal harmonic basis is low, which has allowed an expansion to be performed within each energy group. The source model for AAA and AXB for example apply the same intensity profile to all energies in the spectrum.

8.1.2 Phantom Tests

The performance of COMET with the developed source model was tested using a water phantom, a slab phantom, and a lung phantom generated from an actual patient computed tomography scan and compared to two commercially available treatment planning algorithms, namely Analytical Anisotropic Algorithm and AcurosXB. Central axis depth doses and profiles at depths of 1.5, 10, and 20 cm were compared for both the water phantom and the slab phantom. COMET had the lowest error when compared to Monte Carlo generated reference dose in 64 out of the 108 profile and percentage depth dose tests performed.

Comparisons were also made using the gamma method with the water phantom, slab phantom, and lung phantom. A tight distance-to-agreement of 1%/1mm for the water and slab phantom and 2%/2mm for the lung phantom was chosen to illuminate even the smallest errors in the various algorithms tested. COMET had the highest

percentage of passing pixels in all but one of the tests performed. These results demonstrate the viability of the proposed source model and the COMET method in dosimetric calculations.

The tradeoff in using the COMET method is increased calculation times. While the COMET code is faster than DOSXYZnrc by a factor of approximately 3-12, it was much slower than AAA or AXB. This is due in part to the manner in which the problem is decomposed by COMET. The dose outside the field is calculated using the same mathematical rigor as that inside the field. Also the dose is calculated outside the body contour when an actual patient scan is used. Now that the capabilities of COMET have been demonstrated it is recommended that future work focus on increasing the computational speed and user friendliness.

8.2 Future Work

There are many opportunities for extending the work done in this research project. The novel source treatment developed here can be applied to any treatment planning algorithm including AAA, CCC, and AXB.

The collimator jaws on the linear accelerator limit the maximum polar angle to less than 12 degrees. The functional expansions performed in this work covered the entire range of the hemisphere. A functional expansion that more densely samples the range of polar angles within the restrictions of the collimator jaws and excludes those outside regions under the collimator could improve the accuracy and speed of the source integration step of the calculation.

The same expansion order was used for both the primary and the extra-focal photon sources. The extra-focal photon source accounts for between 11% and 16% of the photon fluence at isocenter [46]. Because the extra-focal photon source contributes

significantly less dose, it may be possible to model it with a lower expansion order and still achieve a high degree of accuracy in the final results.

The electron source in this work was modeled using a very basic exponential equation. While this approach was logical for this work, there have been developed many more sophisticated electron contamination source models that could be included. One approach that could be considered is to apply an electron contamination source within each energy group. Some energy groups may not produce significant numbers of contaminant electrons and the electron treatment disregarded altogether.

The source model used by Eclipse includes a sophisticated optimization routine that varies the parameters of the source model to produce dosimetric calculations that closely match measurements made on a particular machine. Such an approach could be implemented with COMET, particularly in regards to the energy spectrum. The energy spectrum used in this work was taken from the BEAMnrc user code. It could be used as a starting point for an optimization routine that produces a spectrum that better matches measured or ideal results.

The energy spectrum was discretized into 14 bins for this project. The number of energy bins could be varied to investigate the optimal number. A lower number would be preferable to computational simplicity but may not produce the desired level of accuracy.

Response functions were generated for a 6 MV photon beam and five materials, namely water, air, lung, soft tissue, and bone. A possible step in further improving the results could be to generate response functions for more materials. AXB for example uses a material library of 5 biological materials and 16 non-biological materials. Also an adaptive algorithm could be developed that selects the response function expansion order that best applies depending on the source energy, area inside or outside the field,

or tissue inhomogeneity. Although it probably will lead to longer calculation times, it would be interesting to decompose the problem into a tetrahedral mesh rather than cuboidal. That would mean generating response functions for the new mesh shape.

Some additional functionality would make the COMET method more applicable to clinical environment. One addition that will be necessary is the modeling of the multileaf collimator. This will be crucial in calculating intensity modulated and volumetric modulated arc plans. Also it may not be necessary to calculate the dose outside the field with the same mathematical rigor as the dose inside the field because it is low and in many cases will have little or no impact on the patient's outcome. One method would be to implement a spatially varying Cartesian grid for dose calculation, where the local element size is a finer mesh inside the beam.

APPENDIX A

EGSNRC TRANSPORT PARAMETERS

Table 1. EGSnrc Transport Parameters

Parameter	Value
Photon Energy Cutoff	10 keV
Electron Energy Cutoff	700 keV
Photon Cross Sections	XCOM
Electron Step Algorithm	PRESTA-II
Boundary Crossing Algorithm	EXACT
Spin Effects	On
Bound Compton Scattering	norej
Photoelectron Angular Sampling	On
Rayleigh Scattering	On
Atomic Relaxations	On
Bremsstrahlung Cross Sections	NIST
Bremsstrahlung Angular Sampling	KM
Pair Production Angular Sampling	KM

REFERENCES

1. *World Health Organization Cancer Fact Sheet*. 2009 [cited 2010 January 26, 2010]; Available from: http://www.who.int/mediacentre/factsheets/fs297/en/index.html.
2. Ezzell, G.A., et al., *Guidance document on delivery, treatment planning, and clinical implementation of IMRT: report of the IMRT Subcommittee of the AAPM Radiation Therapy Committee.* Medical Physics, 2003. **30**(8): p. 2089-115.
3. Fenoglietto, P., et al., *Eight years of IMRT quality assurance with ionization chambers and film dosimetry: experience of the Montpellier Comprehensive Cancer Center.* Radiation Oncology, 2011. **6**: p. 85.
4. Xing, L., et al., *Overview of image-guided radiation therapy.* Medical Dosimetry, 2006. **31**(2): p. 91-112.
5. *Prevention of Accidents to Patients Undergoing Radiation Therapy.* ICRP Publication 86. Annals of the ICRP, 2000. **30**(3).
6. Holt, A., et al., *Volumetric-Modulated Arc Therapy for Stereotactic Body Radiotherapy of Lung Tumors: A Comparison With Intensity-Modulated Radiotherapy Techniques.* International Journal of Radiation Oncology*Biology*Physics, 2011. **81**(5): p. 1560-1567.
7. Papanikolaou, N. *Heterogeneity Corrections in the IMRT Era*. in *AAPM*. 2007. Minneapolis, MN.
8. Ronde, H.S. and L. Hoffmann, *Validation of Varian's AAA algorithm with focus on lung treatments.* Acta Oncologica, 2009. **48**(2): p. 209-15.
9. Satterfield, M., *Application of a Heterogeneous Coarse-Mesh Transport Method (Comet) to Radiation Therapy Problems*, in *Nuclear and Radiologic Engineering*2006, Georgia Institute of Technology: Atlanta. p. 66.
10. Hayward, R.M. and F. Rahnema, *COMET-PE: an incident fluence response expansion transport method for radiotherapy calculations.* Physics in Medicine and Biology, 2013. **58**(10): p. 3125-43.
11. Jabbari, K., *Review of fast monte carlo codes for dose calculation in radiation therapy treatment planning.* Journal of Medical Signals and Sensors, 2011. **1**(1): p. 73-86.
12. Meredith, W.J., *Atlas of Radiation Dose Distributions.* International Journal of Radiation Biology, 1969. **15**(2): p. 196-196.
13. Papanikolaou, N., et al., *Tissue Inhomogeneity Corrections for Megavoltage Photon Beams.* Report of the Task Group No. 65 of the Radiation Therapy Committee of the AAPM, 2004.
14. Bernhard Kroenig, W.F., *The Principles of Physics and Biology of Radiation Therapy*. 1922, New York: Rebman Company.
15. Quimby, E.H., M.M. Copeland, and R.C. Woods, *The Distribution of Roentgen Rays Withing the Human Body.* The American Journal of Roentgenology, Radium Therapy, and Nuclear Medicine, 1934. **32**: p. 534.

16. Khan, F.M., *The Physics of Radiation Therapy Third Edition*, ed. L.R.K. Michael Standen. 2003, New York: Lippincott Williams & Wilkins.
17. Batho, H.F., *LUNG CORRECTIONS IN COBALT 60 BEAM THERAPY.* Canadian Association of Radiologists Journal, 1964. **15**: p. 79-83.
18. Sontag, M.R. and J.R. Cunningham, *Corrections to absorbed dose calculations for tissue inhomogeneities.* Medical Physics, 1977. **4**(5): p. 431-436.
19. Engelsman, M., et al., *Impact of simple tissue inhomogeneity correction algorithms on conformal radiotherapy of lung tumours.* Radiotherapy and Oncology, 2001. **60**(3): p. 299-309.
20. Mackie, T.R., J.W. Scrimger, and J.J. Battista, *A convolution method of calculating dose for 15-MV x rays.* Medical Physics, 1985. **12**(2): p. 188-196.
21. Mackie, T.R., et al., *Generation of photon energy deposition kernels using the EGS Monte Carlo code.* Physics in Medicine and Biology, 1988. **33**(1): p. 1.
22. Storchi, P.R.M., L.J. van Battum, and E. Woudstra, *Calculation of a pencil beam kernel from measured photon beam data.* Physics in Medicine and Biology, 1999. **44**(12): p. 2917.
23. Ahnesjo, A., M. Saxner, and A. Trepp, *A pencil beam model for photon dose calculation.* Medical Physics, 1992. **19**(2): p. 263-273.
24. Rassiah-Szegedi, P., et al., *Monte Carlo characterization of target doses in stereotactic body radiation therapy (SBRT).* Acta Oncologica, 2006. **45**(7): p. 989-94.
25. Ulmer, W. and W. Kaissl, *A Triple Gaussian Pencil Beam Model for Photon Beam Treatment Planning.* Zeitschrift für Medizinische Physik, 1995. **5**: p. 25-30.
26. Ulmer, W., J. Pyyry, and W. Kaissl, *A 3D photon superposition/convolution algorithm and its foundation on results of Monte Carlo calculations.* Physics in Medicine and Biology, 2005(8): p. 1767.
27. Gagne, I.M. and S. Zavgorodni, *Evaluation of the analytical anisotropic algorithm (AAA) in an extreme water-lung interface phantom using Monte Carlo dose calculations.* Journal of Applied Clinical Medical Physics, 2007. **8**(1).
28. Ahnesjo, A., *Collapsed cone convolution of radiant energy for photon dose calculation in heterogeneous media.* Medical Physics, 1989. **16**(4): p. 577-592.
29. Ahnesjö, A. and M.M. Aspradakis, *Dose calculations for external photon beams in radiotherapy.* Physics in Medicine and Biology, 1999. **44**(11): p. R99.
30. Hasenbalg, F., et al., *Collapsed cone convolution and analytical anisotropic algorithm dose calculations compared to VMC plus plus Monte Carlo simulations in clinical cases.* Physics in Medicine and Biology, 2007. **52**(13): p. 3679-3691.

31. Vassiliev, O.N., et al., *Validation of a new grid-based Boltzmann equation solver for dose calculation in radiotherapy with photon beams.* Physics in Medicine and Biology, 2010. **55**(3): p. 581-98.
32. Lewis, E.E. and W.F. Miller, *Computational Methods of Neutron Transport*. 1993, La Grange Park, Illinois USA: American Nuclear Society, Inc.
33. Wareing, T.A., et al., *Discontinuous Finite Element S_N Methods on Three-Dimensional Unstructured Grids.* Nuclear Science and Engineering, 2001. **138**(3): p. 256-268.
34. Strang, G. and G.J. Fix, *An Analysis of the Finite Element Method*. 1973, Englewood Cliffs, NJ: Prentice-Hall.
35. Eckhardt, R., *Stan Ulam, John von Neumann, and the Monte Carlo method.* Lost Alamos Science, 1987. **15**: p. 131-143.
36. Kawrakow, I. and D.W.O. Rogers, *The EGSnrc Code System: Monte Carlo Simulation of Electron and Photon Transport*, in *Technical Report PIRS-701*2000, National Research Council of Canada: Ottaway, Canada.
37. Faddegon, B.A., et al., *Benchmarking of Monte Carlo simulation of bremsstrahlung from thick targets at radiotherapy energies.* Medical Physics, 2008. **35**(10): p. 4308-17.
38. Rogers, D.W.O., et al., *BEAM: A Monte Carlo code to simulate radiotherapy treatment units.* Medical Physics, 1995. **22**(5): p. 503-524.
39. Rogers, D.W.O., B. Walters, and I. Kawrakow, *BEAMnrc users manual.* NRC Report PIRS, 2001. **509**.
40. Walters, B., I. Kawrakow, and D.W.O. Rogers, *DOSXYZnrc Users Manual*, 2011, National Research Council of Canada Ottawa: Ottawa, CA.
41. Mosher, S.W. and F. Rahnema, *The Incident Flux Response Expansion Method for Heterogeneous Coarse Mesh Transport Problems.* Transport Theory and Statistical Physics, 2006. **35**(1): p. 55 - 86.
42. Zhang, D. and F. Rahnema, *A Heterogeneous Coarse Mesh Method for Coupled Photon Electron Transport Problems.* Transport Theory and Statistical Physics, 2011. **40**(3): p. 127-152.
43. Hayward, R.M., *A Coarse Mesh Transport Method with General Source Treatment for Medical Physics*, in *Department of Nuclear and Rdaiological Engineering and Medical Physics*2009, Georgia Institute of Technology: Atlanta, GA. p. 32.
44. Hayward, R.M. and F. Rahnema, *A Coarse Mesh Transport Method for Radiotherapy Calculations*, 2013, Georgia Insitute of Technology.
45. Hayward, R., *A Coarse Mesh Transport Method for Photons and Electrons in 3-D*, in *Nuclear and Radiological Engineering and Medical Physics*2013, Georgia Institute of Technology: Atlanta, GA.
46. Liu, H.H., T.R. Mackie, and E.C. McCullough, *A dual source photon beam model used in convolution/superposition dose calculations for clinical megavoltage x-ray beams.* Medical Physics, 1997. **24**(12): p. 1960-74.
47. Systems, V.M., *Eclipse Algorithms Reference Guide*, 2010, Varian Medical Systems: Palo Alto, CA. p. 25-98.

48. Isabelle Marie Gagne, S.Z., *Evaluation of the analytical anisotropic algorithm in an extreme water-lung interface phantom using Monte Carlo dose calculations.* Journal of Applied Clinical Medical Physics, 2007. **8**(1): p. 33-46.
49. Han, T., et al., *Dosimetric comparison of Acuros XB deterministic radiation transport method with Monte Carlo and model-based convolution methods in heterogeneous media.* Medical Physics, 2011. **38**(5): p. 2651-64.
50. Sheikh-Bagheri, D. and D.W. Rogers, *Monte Carlo calculation of nine megavoltage photon beam spectra using the BEAM code.* Medical Physics, 2002. **29**(3): p. 391-402.
51. Axler, S., P. Bourdon, and W. Ramey, *Harmonic Function Theory*. 2000, New York: Springer-Verlag.
52. Byerly, W.E., *An Elementary Treatise on Fourier's Series and Spherical, Cylindrical, and Ellipsoidal Harmonics with Applications to Problems in Mathematical Physics*. 1893, Boston: Ginn & Company.
53. MacRobert, T., *Spherical Harmonics. An Elementary Treatise on Harmonic Functions with Applications*. 1927, London: E P Dutton.
54. Wigner, E.P., *Group Theory and its Application to the Quantum Mechanics of Atomic Spectra*. 1959, New York: Academic Press, Inc.
55. D. A. Varshalovich, A.N.M., V. K. Khersonskii, *Quantum Theory of Angular Momentum*. 1988, Singapore: World Scientific Publishing Co. Pte. Ltd.
56. Ramamoorthi, R. and P. Hanrahan, *On the relationship between radiance and irradiance: determining the illumination from images of a convex Lambertian object.* Journal of the Optical Society of America A, 2001. **18**(10): p. 2448-2459.
57. Cabral, B., N. Max, and R. Springmeyer, *Bidirectional reflection functions from surface bump maps*, in *Proceedings of the 14th annual conference on Computer graphics and interactive techniques*1987, ACM. p. 273-281.
58. Sillion, F.X., et al., *A global illumination solution for general reflectance distributions.* SIGGRAPH Computer Graphics, 1991. **25**(4): p. 187-196.
59. Green, R., *Spherical Harmonic Lighting: The Gritty Details.* Archives of the Game Developers Conference, 2003.
60. Gautron, P., et al., *A novel hemispherical basis for accurate and efficient rendering*, in *Proceedings of the Fifteenth Eurographics conference on Rendering Techniques*2004, Eurographics Association: Norrkoping, Sweden. p. 321-330.
61. Griesheimer, D.P., W.R. Martin, and J.P. Holloway, *Convergence properties of Monte Carlo functional expansion tallies.* Journal of Computational Physics, 2006. **211**(1): p. 129-153.
62. Chadsey, W.L., C.W. Wilson, and V.W. Pine, *X-Ray Photoemission Calculations.* Nuclear Science, IEEE Transactions on, 1975. **22**(6): p. 2345-2350.
63. Beers, B.L. and V.W. Pine, *Functional Expansion Technique for Monte Carlo Electron Transport Calculations.* Nuclear Science, IEEE Transactions on, 1976. **23**(6): p. 1850-1856.

64. Noel, A. and H.S. Wio, *A new series-expansion approach in Monte Carlo: Application to neutron shielding.* Annals of Nuclear Energy, 1984. **11**(5): p. 225-227.
65. Cho, S.H., et al., *Reference photon dosimetry data and reference phase space data for the 6MV photon beam from Varian Clinac 2100 series linear accelerators.* Medical Physics, 2005. **32**(1): p. 137-148.
66. *Monte Carlo Data Package High Energy Accelerator Rev 2*, Varian Medical Systems.
67. Griesheimer, D.P., W.R. Martin, and J.P. Holloway, *Estimation of flux distributions with Monte Carlo functional expansion tallies.* Radiat Protection Dosimetry, 2005. **115**(1-4): p. 428-32.
68. Griesheimer, D.P. and W.R. Martin, *Two dimensional functional expansion tallies for Monte Carlo simulations*, in *PHYSOR 2004: The Physics of Fuel Cycles and Advanced Nuclear Systems - Global Developments*2004: Chicago, IL United States.
69. Sawtelle, W.J., *Measurement of the Bremsstrahlung Spectrum of the Linear Accelerator*, in *Physics*1955, Massachusetts Institute of Technology: Cambridge MA.
70. Ali, E.S.M. and D.W.O. Rogers, *Functional forms for photon spectra of clinical linacs.* Physics in Medicine and Biology, 2012. **57**(1): p. 31.
71. Ali, E.S., M.R. McEwen, and D.W. Rogers, *Unfolding linac photon spectra and incident electron energies from experimental transmission data, with direct independent validation.* Medical Physics, 2012. **39**(11): p. 6585-96.
72. Landry, D.J. and D.W. Anderson, *Measurement of accelerator bremsstrahlung spectra with a high-efficiency Ge detector.* Medical Physics, 1991. **18**(3): p. 527-32.
73. Fippel, M., et al., *A virtual photon energy fluence model for Monte Carlo dose calculation.* Medical Physics, 2003. **30**(3): p. 301-311.
74. Sikora, M. and M. Alber, *A virtual source model of electron contamination of a therapeutic photon beam.* Physics in Medicine Biology, 2009. **54**(24): p. 7329-44.
75. Yang, J., et al., *Modelling of electron contamination in clinical photon beams for Monte Carlo dose calculation.* Physics in Medicine and Biology, 2004. **49**(12): p. 2657.
76. Mackie, T.R. and J.W. Scrimger, *Contamination of a 15-MV photon beam by electrons and scattered photons.* Radiology, 1982. **144**(2): p. 403-9.
77. Ahnesjö, A., M. Saxner, and A. Trepp, *A pencil beam model for photon dose calculation.* Medical Physics, 1992. **19**(2): p. 263-273.
78. Tillikainen, L., et al., *Determination of parameters for a multiple-source model of megavoltage photon beams using optimization methods.* Physics in Medicine and Biology, 2007. **52**(5): p. 1441-67.
79. Rogers, D.W.O. and R. Mohan, *Questions for comparison of clinical monte carlo codes*. The Use of Computers in Radiation Therapy: XIIIth Interantional Conference. 2000, Heidelberg, Germany: Springer.

80. Kawrakow, I., M. Fippel, and K. Friedrich, *3D electron dose calculation using a Voxel based Monte Carlo algorithm (VMC).* Medical Physics, 1996. **23**(4): p. 445-457.
81. Low, D.A., et al., *A technique for the quantitative evaluation of dose distributions.* Medical Physics, 1998. **25**(5): p. 656-661.
82. *OmniPro I'mRT System Version 1.7b User's Guide*, 2010, IBA Dosimetry: Schwarzenbruck, Germany.

VITA

CALEB I. PRICE

Caleb Price grew up in Valdosta, GA. He received a BS degree in Physics in 2001 from Valdosta State University and a MSMP in 2005 from the Georgia Institute of Technology. Mr. Price has worked in several radiation oncology departments and currently serves as the Chief of Medical Physics at Memorial University Medical Center. His research has resulted in two publications in major scientific journals with a third under review. When not researching, Mr. Price enjoys brewing beer, playing classical guitar, and riding vintage motorcycles.